Kazan Federal University
Zavoisky Physical-Technical Institute
Institute of Perspective Research
Tatarstan Academy of Sciences
Russian Foundation for Basic Research
Russian Science Foundation
Bruker Ltd (Moscow)

ACTUAL PROBLEMS OF MAGNETIC RESONANCE AND ITS APPLICATION

XIX International Youth Scientific School

ACTUAL PROBLEMS OF MAGNETIC RESONANCE AND ITS APPLICATION
KAZAN

Program
Lecture Notes
Proceedings

Kazan
24 - 28 October 2016

Kazan Federal University
Zavoisky Physical-Technical Institute
Institute of Perspective Research
Tatarstan Academy of Sciences
Russian Foundation for Basic Research
Russian Science Foundation
Bruker Ltd (Moscow)

ACTUAL PROBLEMS OF MAGNETIC RESONANCE AND ITS APPLICATION

XIX International Youth Scientific School

Program
Lecture Notes
Proceedings

Kazan
24 – 28 October 2016

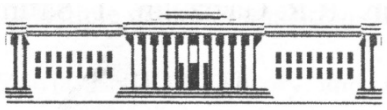

KAZAN
2016

UDC 537
LBC 22.334
A19

Administration of the School

Professor M.S. Tagirov (KFU, Kazan) — rector
Professor V.A. Zhikharev (KSTU, Kazan) — vice-rector
V.K. Voronkova (KFTI RAS, Kazan) — scientific secretary
I.P. Volodina (KFU, Kazan) — secretary

Program committee

Chairman
Professor V.A. Atsarkin (IREE, Moscow)

Committee members

Professor A.V. Aganov (KFU, Kazan)
Professor I.A. Garifullin (KFTI RAS, Kazan)
Academician of RAS K.M. Salikhov (KFTI RAS, Kazan)
Professor V.D. Skirda (KFU, Kazan)
Professor L.R. Tagirov (KFU, Kazan)

Organizing committee

M.S. Tagirov, V.A. Zhikharev, I.P. Volodina, I.G. Motygullin, A.V. Klochkov, E.M. Alakshin, I.V. Romanova, M.P. Rodionova, E.I. Kondratyeva, T.R. Safin, V.V. Kuzmin, S.A. Volodin, Yu. Kochneva

A19 **Actual problems of magnetic resonance and its application:** program, lecture notes, proceedings of the XIX International Youth Scientific School (Kazan, 24 – 28 October 2016) / edited by M.S. Tagirov, V.A. Zhikharev. – Kazan: Kazan University Press, 2016. – 124 p.

ISBN 978-5-00019-709-7

This collection contains the reports of young scientists submitted to the XIX International Youth Scientific School “Actual problems of magnetic resonance and its application”, organized by the Kazan Federal University and the Zavoisky Physical-Technical Institute.

UDC 537
LBC 22.334

ISBN 978-5-00019-709-7

Program

Monday, October 24

Conference Hall of Lobachevsky Scientific Library

8:30 **Registration**
10:00 – 10:30 **Opening Ceremony of School-2016**

Lectures Conference Hall of Lobachevsky Scientific Library

10:30 – 11:30 **Yu.M. Bunkov** (Grenoble, France), "Supermagnonics"

11:30 – 12:30 **I.R. Mukhamedshin** (Kazan, Russia), "The digital domain of NMR spectrometer"

Oral Session Conference Hall of Lobachevsky Scientific Library

14:00 – 14:20 **G.S. Musabirova,** "Study of the spatial structure of fluvastatin and its complex with dodecylphosphocholine micelles by NMR spectroscopy"

14:20 – 14:40 **T.M. Salikhov,** "Influence of the non-stoichiometry on the frustrated honeycomb layered lithium nickeloantimonate"

14:40 – 15:00 **O.G. Miheeva,** "Two dimensional nuclear magnetic resonance spectroscopy in research of structure and dynamics of human insulin"

15:00 – 15:20 **M.M. Bakirov,** "Analysis of manifestations of spin exchange and dipole-dipole interactions in EPR spectra of nitroxyl radical solutions"

15:20 – 15:40 **R. Likerov,** "Investigations of $Y_2SiO_5:Nd^{143}$ by ESR method"

15:40 – 16:00 **A.E. Bardasova,** "EPR investigation of the aggregation of copper porphyrin"

16:00 – 16:20 **D.V. Shurtakova,** "EPR and spin-lattice relaxation in nanoscale hydroxyapatite powder"

16:20 – 16:40 **A.V. Vovk,** "Dysfunction of mitochondria and adipose tissue inflammation in patients with rectal cancer"

18:00 **Welcome Party**

Tuesday, October 25

Lectures Conference Hall of Lobachevsky Scientific Library

9:00 – 10:00 **M.Yu. Presnyakov,** (Moscow, Russia), "Resource Center of Probe and Electron Microscopy as an instrumental component of the NRC Kurchatov Institute research infrastructure"

10:00 – 11:00 **E.B. Fel'dman (**Chernogolovka, Russia), "Magnus expansion paradoxes in spin dynamics and quantum informatics"

11:00 – 11:30 **Coffee break**

11:30 – 12:30 **F.S. Dzheparov (**Moscow, Russia), "Impurity spin in normal stochastic field: basic model of magnetic resonance"

Oral Session Conference Hall of Lobachevsky Scientific Library

14:00 – 14:20 **I.A. Khodov,** "Conformational NMR analysis of small flexible molecules by 2D NOESY"

14:20 – 14:40 **E.A. Kovalenko,** "Supramolecular systems of peptides and cucurbit[7]uril"

14:40 – 15:00 **A.Yu. Germov,** "^{87}Sr NMR study of inhomogeneous state in $Sr_{1-x}La_xMnO_3$ (x = 0; 0.02; 0.04)"

15:00 – 15:20 **G.A. Bochkin,** "Dipolar relaxation of multiple-quantum MNR coherences in a linear homogeneous chain of ^{19}F nuclei in calcium fluoroapatite"

15:20 – 15:40 **S.I. Serobaba,** "Experimental vs GIAO calculated NMR spectra for 5,8-dihydro-4*H*-pyrazolo[5,1-*d*][1,2,5]triazepin-4-ones"

15:40 – 16:00 **D.V. Nazipov,** "Ab initio study of single-crystalline $BiMnO_3$"

16:00 – 16:20 **A.V. Koshelev,** "The long-range magnetic order in shattuckite $Cu_5(OH)_2(SiO_3)_4$"

16:20 – 16:40 **Coffee break**

16:40 – 17:00 **Yu.V. Krasnikova,** "Antiferromagnetic resonance in noncollinear antiferromagnet $Mn_3Al_2Ge_3O_{12}$"

17:00 – 17:20 **A.V. Sergeev,** "Application of Overhauser DNP and K optics INTERMAGNET quantum magnetometers to fundamental physics and cosmology"

17:20 – 17:40 **S.G. Vasil'ev,** "Multiple-quantum NMR in hybrid organic-inorganic silica gels and aerogels"

17:40 – 18:00 **R.S. Denisov,** "ESR study of new low-dimensional magnet $Co(NO_3)_2$"

18:00 – 18:20 **A.V. Fedorov,** "Perspective applications of NMR relaxometery to blood thromboelastography"

18:20 – 18:40 **E.D. Narkhov,** "New vector/scalar Overhauser DNP magnetometers POS-4 for magnetic observatories and directional oil drilling support"

18:40 – 19:00 **T.R. Safin,** "Pulse NMR investigations of $MnCO_3$"

Wednesday, October 26

Museum of Kazan University. Main building.

10:00 **Awarding Ceremony of Zavoisky Youth Scientific Prize Winners**

Lectures Conference Hall of Lobachevsky Scientific Library

14:00 – 15:00 **M.R. Gafurov** (Kazan, Russia), "Combination and recombination of free radical paramagnetic centers in heavy petroleum fractions"

15:00 – 16:00 **I.A. Larionov** (Kazan, Russia), "Theory of magnetic resonance response in HTSC cuprates"

16:00 – 16:30 **Coffee break**

16:30 – 17:30 **E. Goovaerts** (Antwerp, Belgium), "The fate of charge excitations in organic photovoltaic devices studied by electrically detected magnetic resonance"

Thursday, October 27

Lectures Conference Hall of Lobachevsky Scientific Library

9:00 – 10:00 **R.M. Eremina** (Kazan, Russia), "Anisotropic exchange interaction in low dimensional systems"

10:00 – 11:00 **S.B. Orlinskii** (Kazan, Russia), "Macro-, micro- and nanodiamonds by HF EPR/ENDOR"

11:00 – 11:30 **Coffee break**

11:30 – 12:30 **V. Kataev** (Dresden, Germany), "Sub-THz EPR spectroscopy of correlated spin systems in high magnetic fields"

Oral Session Conference Hall of Lobachevsky Scientific Library

14:00 – 14:20 **I.I. Gimazov,** "Superconducting fluctuations above critical temperature in the $Bi_2Sr_2Ca_{1-x}Y_xCu_2O_8$ single crystals"

14:20 – 14:40 **A.A. Stanislavovas,** "Spin kinetics research of ^3He in contact with Al_2O_3 ordered aerogel"

14:40 – 15:00 **D.S. Nuzhina,** "Synthesis and study of the magnetic properties of micro- and nanosize powders $LiTbF_4$ and TbF_3"

15:00 – 15:20 **A.V. Shestakov,** "Investigation magnetic properties HgCdTe:Ag and HgSe:Cr"

15:20 – 15:40 **A.V. Petrova,** "Ab initio investigations of double rare earth fluorides under pressure"

15:40 – 16:00 **G.A. Dolgorukov,** "Spin kinetics of ^3He in contact with detonation nanodiamonds"

16:00 – 18:00 **Master-classes**
Formation of groups for masters-classes will be made at registration.

Friday, October 28

Lectures Conference Hall of Lobachevsky Scientific Library

9:00 – 10:00 **U. Eichhoff** (Ettlingen, Germany), "Preclinical magnetic resonance imaging"

10:00 – 11:00 **V.A. Zhikharev** (Kazan, Russia), "20 years of Youth scientific school "Actual problems of magnetic resonance and its application""

11:00 **Closing Ceremony of School-2016**

Supermagnonics

Yu.M. Bunkov

Institut Neel, Grenoble, France
Kazan Federal University, Kazan, Russia

e-mail: Yury.bunkov@neel.cnrs.fr

The Electronics is the field of science which describes the non-linear behavior of electric current. It was developed for a century. Later there was observed the phenomenon of supercurrent – the coherent transport of electrons without friction. This effect forms the basis of new types of electronics — Superelectronics. The main element of Superelectronics is the Josephson connection – the interference between the coherent wave function of electrons on a two sides of week connection. This effect leads to a construction of SQUID, the supersensitive devise which can measure of a quant of magnetic field. The circuits with SQUID may be used as an element of quantum memory.

Later the new types of non-linear phenomena were developed — Spintronics and Magnonics. In the first case the magnetic moment of electrons takes in to account. Indeed, the Superpintronics does not exist because the electron Cooper pairs has a zero magnetic moment.

The Magnonics case refers to information transport and processing by spin waves. A magnon current has advantages as compared to a conventional spin-polarized electron current. It does not involve the motion of electrons and, thus, it is free of Joule heat dissipation. In low-damping magnetic dielectrics (for example, yttrium-iron-garnet, YIG) magnons can propagate over millimeters distances whereas an electron-carried spin current is limited by the spin diffusing length, which does not exceed one micrometre.

Indeed the coherent magnon transport was observed about 30 years ago in Kapitza Institut. In different with a simple magnonics, the magnetization transport by Supermagnonics described by a coherent state of magnons – the magnons Bose Condensate. Its gradient leads to a Spin Supercurrent. There was observed the Josephson Effect, the main nonlinear effect of Supermagnonics. The Supermagnonics was observed in superfluid 3He-B. Indeed, the magnetic properties of superfluid ^{3}He-B are described as a 3 sublattice antiferromagnetic. The other examples, where the magnons BEC was observed are superfluid ^{3}He-A, Nuclear-electron precession in antiferromagnets ($MnCO_3$, $CsMnF_3$) and yttrium-iron-garnet, YIG. In the last case the Supermagnonics and Josephson Effect may be observed at room temperature. This phenomena are under investigations.

The digital domain of NMR spectrometer

I.R. Mukhamedshin

Institute of Physics, Kazan Federal University, 420008 Kazan, Russia

e-mail: Irek.Mukhamedshin@kpfu.ru

Nuclear Magnetic Resonance (NMR) spectrometers have now become very complicated instruments capable of performing sophisticated experiments. The transition of NMR spectrometers to digital electronics domain which happened in a last decade has drastically reduced the size and price of NMR spectrometers. This extends the possible fields of application for NMR and promotes novel NMR experiments.

In this lecture I'll make a review of the classical "analog" NMR spectrometer and the main shortcomings of it. After the short introduction to digital electronics the modern way of digital circuit implementation using special semiconductor chips — Field-Programmable Gate Array (FPGA) — will be represented. With FPGA the digital devices can be built by writing codes in a hardware description language, like software development. The possible realization of the main modules of digital NMR spectrometer using FPGA will be demonstrated.

At the end the home-built digital NMR spectrometer "Kazan-Nova II" will be introduced. It is a highly integrated FPGA-based nuclear magnetic resonance spectrometer which works in the frequency range up to 160 MHz. Inside the FPGA chip a number of digital modules have been implemented including the digital part of frequency synthesizers, pulse sequencer, a digital quadrature receiver and a computer interface. The system is composed of the single printed-circuit 110×180 mm board on which all associated analogue circuits are implemented — direct-digital synthesis circuits, RF transmission, signal amplification and acquisition, as well as a FPGA board connectors. The only two external devices necessary to complete NMR spectrometer are low noise pre-amplifier and RF pulse power amplifier.

This work was partially supported by the RFBR under project 14-02-01213a.

Macro-, micro- and nanodiamonds by HF EPR/ENDOR

A.A. Soltamova[2], P.G. Baranov[2], O. Shenderova[3], G.V. Mamin[1], B.V. Yavkin[1], S.B. Orlinskii[1]

[1]Kazan (Volga region) Federal University, EPR division of the Centre of the Shared Facilities, Kazan, Russia

[2]Ioffe Physicotechnical Institute, Russia

[3]International Technology Centre, USA

e-mail: orlinskii@list.ru

Magnetic resonance methods are the basic techniques for studying spin phenomena in condensed matter and biological systems. Spin phenomena are playing a crucial role in the development of devices based on nanostructures. Nanoparticles are also widely used in tehnologies and medicine, for transfection, gene silencing, photodynamic therapy, drug delivery, etc.

Since 2007 in the EPR division of the Centre of the Shared Facilities of Kazan Federal University we investigate special nanostructures.

Paramagnetic centers of substitutional nitrogen in micro- and nanocrystalline diamond particles have been identified in pulsed EPR spectra at room temperature

At temperature 200 K in spite of the presence of 10^4 of interfering spins from the surface defects per one spin from nitrogen

A novel approach based on EPR analysis of nanodiamond hydrosols was suggested for efficient separation of EPR signals of paramagnetic centers localized within nanocrystals from those present on the nanoparticle surface.

References

[1] Soltamova, A.A., et al (2009) Physica B. 404 (23-24) 4518.

[2] Baranov, P. G., et al (2009) JETP Letters. 89(8), 409.

[3] Baranov, P.G., et al (2010) Applied Magnetic Resonance, 39 (1), 151.

[4] Soltamova, A.A., et al (2010) JETP Letters, 92(2), 102.

[5] Ilyin I.V., et al (2011) Fullerenes Nanotubes and Carbon Nanostructures, 19(1-2), 44.

[6] Orlinskii, S.B. et al (2011) Nanoscience and Nanotechnology Letters, 3(1), 63.

[7] Shenderova, O.A., et al (2011*)* J. Phys. Chem. C. 115 (29), 14014.

[8] Baranov, P.G.et al (2011) Small 7(11), 1533.

[9] Yavkin B.V., et al (2013) Applied Magnetic Resonance. 44(10), 1235.

[10] Yavkin B.V., et al (2014) Applied Magnetic Resonance. 45(10), 1035.

[11] Kratochvilova, Irena; et.al (2014) *)* J. Phys. Chem. C. 118(43), 25245.

[12] Yavkin, B. V.; et al., Magnetic Resonance in Solids. (2015), 17(1), 15101.

[13] Yavkin, B. V.; et al., (2016) J.Magnetic Resonance. 262, 15.

Magnus expansion paradoxes in spin dynamics and quantum informatics

E.B. Fel'dman[1], D.E. Feldman[2], E.I. Kuznetsova[1]

[1]Institute of Problems of Chemical Physics of Russian Academy of Sciences, Chernogolovka, 142432, Moscow Region, Russia;

[2]Department of Physics, Brown University, Providence, Rhode Island 02912, USA

e-mail: efeldman@icp.ac.ru

The divergence of the Magnus expansion leads to paradoxes in spin dynamics of solid-state NMR and in quantum informatics. This lecture presents results on quasi-equilibrium magnetization in a system of dipole-dipole (DD) coupled spins at times $T_2 << t << T_1\rho$ in multiple-pulse spin locking (T_2 is the transverse spin relaxation time and $T_1\rho$ is the rotating-frame spin-lattice relaxation time). It is shown how contradictions between results, obtained with the Magnus expansion, and experimental data can be resolved. Entanglement is investigated in a two-spin system with DD interactions in a multi-pulse spin locking experiment. We discover a conflict between an exact solution and the standard approximation employing a time-independent Floquet Hamiltonian. It is shown that while the exact solution yields non-zero entanglement in the system the Floquet approach predicts that entanglement is absent. The failure of the Floquet method is explained by the multivaluedness of the Floquet Hamiltonian. Correct results can only be obtained with a proper choice of the branch of the Hamiltonian. The developed methods can be useful in different branches of physics.

This study was supported in part by the Russian Foundation for Basic Research (project no. 16-03-00056) and by Program 1.26 of the Presidium of the Russian Academy of Sciences "Electron spin resonance, spin-dependent electron effects, and spin technologies" (grant 0089-2015- 0191).

Impurity spin in normal stochastic field: basic model of magnetic resonance

F.S. Dzheparov, D.V. Lvov

Institute for Theoretical and Experimental Physics, Moscow 117258, Russia

e-mail: dzheparov@itep.ru, lvov@itep.ru

Famous Anderson-Weiss-Kubo model of magnetic resonance is reconsidered in order to bridge existing gaps in its applications for solutions of fundamental problems of spin dynamics and theory of master equations. The model considers the local field fluctuations as one-dimensional normal random process. We refined the conditions of applicability of perturbation theory to calculate the spin depolarization. A counterexample is considered to show that in the absence of temporal fluctuations of local fields, perturbation theory is not applicable even qualitatively. It is shown that for slow fluctuations the behavior of the longitudinal magnetization is simply related to the correlation function of the local field. The effect could be checked by the experimental studies of magnetic resonance in quasi-Ising paramagnets.

Spin system with the Hamiltonian (written in rotating frame)

$$H = H_0(t) + H_1, \quad H_1 = \omega_1 I_x, \quad H_0(t) = \left(\Delta + \omega_l(t)\right) I_z = H_I + H_l(t) \tag{1}$$

is one of most important basic models for studies in spin dynamics. Here I_α is spin operator, Δ is the detuning from the resonance, ω_1 represents magnitude of the rotating field, and $\omega_l(t)$ corresponds to time dependent local field, produced by surrounding substance. Famous Anderson-Weiss-Kubo (AWK) model [1] considers $\omega_l(t)$ as a normal stationary stochastic process with the correlation function $\langle \omega_l(t)\omega_l(t_1)\rangle_n = M_2\kappa\left(|t-t_1|\right)$, $M_2 = \langle \omega_l^2 \rangle_n$, it means, that for any reasonable function $\alpha(t)$ the moment-generating functional is of the form

$$\Phi(t,0,[\alpha]) = \left\langle \exp\left(i\int_0^t d\tau \alpha(\tau)\omega_l(\tau)\right)\right\rangle_n = \exp\left(-\frac{M_2}{2}\int_0^t d\tau_1 d\tau_2 \alpha(\tau_1)\alpha(\tau_2)\kappa(\tau_1-\tau_2)\right). \tag{2}$$

Here averaging is fulfilled on distribution of random trajectories $\omega_l(t)$ (noise).

The model was created to explain the "narrowing of the resonance line by motion" using Gaussian or simple exponential $\kappa\left(|t|\right)$, but it was successful for explaining of the line shape for impurity beta-active nuclei [2,3] without measured differences between experimental data and theoretical predictions for more realistic $\kappa\left(|t|\right)$. It was adopted to describe two- and multi-spin transitions [3-5] with successful incorporation both static and dynamic correlations of local fields on impurity spins [6]. The model found important application in description of the electron spin echo [7] and it produces a kernel for modern theory of spin dynamics in magnetically diluted systems [8,9].

An important application of the model consists in derivation of the applicability conditions for perturbation theory for small ω_1 in calculation of longitudinal correlation function

$$F(t) = \langle I_z I_z(t)\rangle / \langle I_z^2\rangle = \langle \langle I_z I_z(t)\rangle_0 \rangle_n / \langle I_z^2\rangle_0 . \tag{3}$$

Here $\langle A\rangle_0 = Tr(A)/Tr(1)$ for any relevant operator A, that corresponds to averaging with infinite spin temperature. The function $F(t)$ is proportional to observable value of the operator $I_z(t)$, if the initial state of the density matrix $\rho(t)$ is of standard form

$$\rho_0 = \rho(t=0) = \frac{1}{Tr(1)}\left(1+\frac{3p_0}{I(I+1)}I_z\right), \qquad p_0 = \langle I_z(t=0)\rangle = Tr\left(I_z\rho(t=0)\right). \tag{4}$$

Indeed, p_0 doesn't depend on ω_l, therefore

$$J_z(t) = \left\langle Tr\left(I_z\rho(t)\right)\right\rangle_n = \left\langle Tr\left(I_z(t)\rho(t=0)\right)\right\rangle_n = F(t)p_0 \tag{5}$$

The advantage of the model is the realistic smooth time dependence of local field contrary to known exactly solvable models with hopping evolution of $\omega_l(t)$. As usual it is expected [1,10,11], that if Δ=0, then the simplest conditions $\varepsilon_1 = R_0T_2 \ll 1$, and $\varepsilon_2 = R_0\tau_c \ll 1$, where

$$R_0 = \omega_1^2 T_2, \qquad T_2 = \int_0^\infty dt \exp\left(-M_2\int_0^t d\tau(t-\tau)\kappa(\tau)\right), \qquad \tau_c = \int_0^\infty dt\kappa(t), \tag{6}$$

produce $F(t) = \exp(-R_0t)$, but nothing is known for slow smooth motion, when $R_0\tau_c \gg 1$.

We will indicate below, that for smooth $\omega_l(t)$ there exist logarithmical correction to the ε_2, similar to the correction, indicated early for two-spin flip-flop transitions [5], and we will construct the solution for very slow smooth motions, which is valid in the main order in $\varepsilon_1 = \omega_1^2T_2^2 \ll 1$. It has the form

$$F(t) = \frac{2}{\pi}\arcsin\kappa(t). \tag{7}$$

1. Very fast fluctuations — δ-correlated local fields

If $\tau_c = 0$ then correlation of local field can be written as

$$\langle\omega_l(t)\omega_l(t_1)\rangle_n = \frac{2}{T_2}\delta(t-t_1), \tag{8}$$

and the phase evolutions at different times are independent. Indeed, if $t \le t' \le t_1$, then, according to relation (2), we have

$$\begin{aligned}\Phi(t,t',[\alpha]) &= \left\langle \exp\left(i\int_{t'}^t d\tau\alpha(\tau)\omega_l(\tau)\right)\right\rangle_n = \exp\left(-\frac{1}{T_2}\int_{t'}^t d\tau\alpha^2(\tau)\right) = \\ &= \exp\left(-\frac{1}{T_2}\int_{t_1}^t d\tau\alpha^2(\tau) - \frac{1}{T_2}\int_{t'}^{t_1} d\tau'\alpha^2(\tau')\right) = \Phi(t,t_1,[\alpha])\Phi(t_1,t',[\alpha]).\end{aligned} \tag{9}$$

Basing on this relation the quantum Liouville equation for density matrix $\rho(t)$

$$\frac{\partial}{\partial t}\rho = -i[H,\rho] = -iL\rho = -i(L_0+L_1)\rho, \quad L_0\rho = [H_0,\rho], \quad L_1\rho = [H_1,\rho], \tag{10}$$

can be rewritten in the integral form

$$\rho(t) = e^{-i\int_0^t d\tau L_0(\tau)}\rho_0 - i\int_0^t d\tau e^{-i\int_\tau^t d\tau_1 L_0(\tau_1)} L_1\rho(\tau). \tag{11}$$

Here and below we will use superoperator formalism, basic information about which can be found, for example, in the textbook [12]. The superoperator $L_0(t)$ commutes with itself for different times $L_0(t_1)L_0(t_2) = L_0(t_2)L_0(t_1)$, that admits to use simple exponential in (11) instead of chronological ordering, required in absence of the commutativity.

For the sake of brevity below $t > 0$. The Eq.(11) is exact as well as (10), but for δ-correlated local field it admits exact averaging on local field fluctuations:

$$\begin{aligned}\langle\rho(t)\rangle_n &= \left\langle \exp\left(-i\int_0^t d\tau L_0(\tau)\right)\right\rangle_n \rho_0 - i\int_0^t dt_1 \left\langle \exp\left(-i\int_{t_1}^t d\tau L_0(\tau)\right) L_1\rho(t_1)\right\rangle_n = \\ &= \left\langle \exp\left(-i\int_0^t d\tau L_0(\tau)\right)\right\rangle_n \rho_0 - i\int_0^t dt_1 \left\langle \exp\left(-i\int_{t_1}^t d\tau L_0(\tau)\right)\right\rangle_n L_1\langle\rho(t_1)\rangle.\end{aligned} \tag{12}$$

It was used in (11) and (12), following to Ref. [13], that effectively, as in (9), we have $\tau > t_1$. The properties of the superoperator $L_0(\tau)$ relative to the averaging on local field fluctuations are the same as for simple function $\alpha(\tau)\omega_l(\tau)$. Therefore, particularly, as a consequence of (9), we have

$$U(t-t_1) = \left\langle \exp\left(-i\int_{t_1}^t d\tau L_0(\tau)\right)\right\rangle_n = \exp\left(-\left(i\Delta I_z^{\times} + \frac{1}{T_2}\left(I_z^{\times}\right)^2\right)|t-t_1|\right) = U(t-t')U(t'-t_1). \tag{13}$$

Here $t \geq t' \geq t_1$ or $t \leq t' \leq t_1$ and new superoperator $I_z^{\times}$ is produced from usual spin operator I_z according to the standard rule $I_z^{\times} f = [I_z, f]$, where f is arbitrary operator. More rigorous mathematical treatment can start from iterative solution of the Eq. (11) with consequent averaging on local field fluctuations using the relation (9) and checking, that obtained solution obey the Eq. (12).

As a result of Eqs. (12) and (13) we have for $t > 0$

$$\frac{\partial}{\partial t}\langle\rho(t)\rangle_n = -\left(i\Delta I_z^{\times} + R\left(I_z^{\times}\right)^2 + iL_1\right)\langle\rho(t)\rangle_n. \tag{14}$$

Last equation is equivalent to Bloch's equations for average values of spin operators

$$J_\alpha(t) = Tr\left(I_\alpha\langle\rho(t)\rangle_n\right). \tag{15}$$

Indeed, multiplying the Eq. (14) on I_α, and calculating the trace with taking into account the relations

$$Tr\left(A[B,C]\right) = Tr\left([A,B]C\right), \quad I_z^{\times 2} I_{x,y} = \left[I_z\left[I_z, I_{x,y}\right]\right] = I_{x,y}, \quad I_z^{\times 2} I_z = 0, \tag{16}$$

we immediately obtain the Bloch's equations in absence of longitudinal spin-lattice relaxation:

$$\frac{\partial}{\partial t}J_z = [\boldsymbol{\Omega}\times\mathbf{J}]_z, \quad \frac{\partial}{\partial t}J_{x,y} = [\boldsymbol{\Omega}\times\mathbf{J}]_{x,y} - \frac{1}{T_2}J_{x,y}, \quad \boldsymbol{\Omega} = (\omega_1, 0, \Delta). \tag{17}$$

To solve the Eqs. (17) conventional variables $J_\pm = J_x \pm iJ_y$ are useful. For them

$$\frac{\partial}{\partial t}J_+ = i\Delta J_+ - i\omega_1 J_z - \frac{1}{T_2}J_+, \quad \frac{\partial}{\partial t}J_- = -i\Delta J_- + i\omega_1 J_z - \frac{1}{T_2}J_-, \quad \frac{\partial}{\partial t}J_z = -\frac{i\omega_1}{2}\left(J_+ - J_-\right). \quad (18)$$

Excluding $J_\pm(t)$ with initial condition $J_\pm(t=0)=0$ (according to (4)) we receive the equation

$$\frac{\partial}{\partial t}J_z = -\omega_1^2 \,\mathrm{Re}\int_0^t d\tau e^{\left(i\Delta-\frac{1}{T_2}\right)\tau} J_z(t-\tau), \quad (19)$$

which is exact for δ-correlated process (8). We see that for small ω_1 the derivative $\partial J_z/\partial t \sim \omega_1^2$ is small. Therefore the variation of $J_z(t-\tau)$ during the times τ, important for the multiplayer $\exp\left(\left(i\Delta - 1/T_2\right)\tau\right)$ in the integrand of Eq. (19), is negligible, and for $t > T_2$ we can replace the Eq.(19) by

$$\begin{aligned} &\frac{\partial}{\partial t}J_z = -\omega_1^2 \,\mathrm{Re}\int_0^\infty d\tau e^{\left(i\Delta-\frac{1}{T_2}\right)\tau} J_z(t) = -R(\Delta)J_z(t), \qquad R(\Delta) = \pi\omega_1^2 g(\Delta), \\ &g(\Delta) = \mathrm{Re}\int_{-\infty}^{\infty}\frac{dt}{2\pi}e^{i\Delta t - |t|/T_2} = \frac{T_2}{\pi\left(1+\Delta^2 T_2^2\right)}. \end{aligned} \quad (20)$$

Here normalized resonance line shape $g(\Delta)$ is introduced; it is a Fourier transform of free induction decay $F_0(t) = \left\langle I_+(t,\Omega=0)\mathrm{I}_-\right\rangle / \left\langle I_+\mathrm{I}_-\right\rangle$, which has simple exponential form $F_0(t) = \exp\left(-|t|/T\right)$ for δ-correlated local field. It is evident from Eqs. (12), (13), (16) with $L_1 = 0$ and $\Delta = 0$.

Comparing Eqs. (19) and (20) we see, that ω_1 is small, if, at least, $R \ll 1/T_2$. To refine the condition we can retain in (20) next, linear in τ term of $J_z(t-\tau)$, that produce

$$\begin{aligned} &\frac{\partial}{\partial t}J_z = -\omega_1^2 \,\mathrm{Re}\int_0^\infty d\tau e^{\left(i\Delta-\frac{1}{T_2}\right)\tau}\left(J_z(t) - \tau\frac{\partial}{\partial t}J_z(t)\right) = -Rt + \vartheta\frac{\partial}{\partial t}J_z, \\ &\vartheta = \mathrm{Re}\,\omega_1^2\int_0^\infty d\tau e^{\left(i\Delta-\frac{1}{T_2}\right)\tau}\tau = \omega_1^2\frac{T_2^2\left(1-\left(\Delta T_2\right)^2\right)}{\left(1+\left(\Delta T_2\right)^2\right)^2}, \quad |\vartheta| \le R(\Delta)T_2 \le R_0 T_2 = \varepsilon_1, \quad R_0 = R\left(\Delta=0\right). \end{aligned} \quad (21)$$

It is evident, that condition of smallness of ω_1 received the form $|\theta| \ll 1$. For $\Delta = 0$ new condition coincides with previous $\varepsilon_1 = R_0 T_2 = \omega_1^2 T_2^2 \ll 1$, but with increasing of Δ it can be less restrictive.

2. Fast fluctuation of local fields and the perturbation theory

Modern perturbation theory consists of two different, but connected parts: obtaining the effective Hamiltonian and derivation of master equation, see [14] for example. Master equation is an equation for important part of the density matrix $\rho(t)$, which is sufficient for calculation of necessary observables. To derive it according to projection technique of Nakajima-Zwanzig we can introduce the projection superoperators P, which separates the important part:

$$P\rho = \langle \rho_D \rangle_n = \big(\langle \rho \rangle_n \big)_D . \tag{22}$$

Here index D separates the part, diagonal in representation of eigenstates of I_z, i.e., if $I_z|m\rangle = m|m\rangle$, then $\langle n|\rho_D|m\rangle = \delta_{mn}\langle m|\rho|m\rangle$.

Multiplication of Liouville Eq.(10) on P and $\overline{P} = 1 - P$ produces

$$\frac{\partial}{\partial t} P\rho = -iPL\left(P + \overline{P}\right)\rho, \quad \frac{\partial}{\partial t}\overline{P}\rho = -i\overline{P}L\left(P + \overline{P}\right)\rho.$$

Both P and $\overline{P}$ are projectors, because $P^2 = P$ and $\overline{P}^2 = \overline{P}$. Solving second equation with initial condition $\overline{P}\rho_0 = 0$ and substituting the solution into the first equation we receive a master equation

$$\frac{\partial}{\partial t} P\rho = -iPLP\rho - \int_0^t d\tau PL(t)\overline{P}T\exp\left(-i\int_\tau^t ds\overline{P}L(s)\overline{P}\right)\overline{P}L(\tau)P\rho(\tau).$$

Here $T\exp(\cdots)$ is the standard chronological exponential. Our projectors obey the relations $PLP = 0$, $PL\overline{P} = PL_1\overline{P} = PL_1$, $\overline{P}LP = \overline{P}L_1P = L_1P$, therefore more simple exact equation is valid:

$$\begin{aligned} &\frac{\partial}{\partial t} P\rho = -\int_0^t d\tau PL_1 T\exp\left(-i\int_\tau^t ds\overline{P}L(s)\overline{P}\right)L_1 P\rho(\tau) = \\ &= \int_0^t d\tau M(t-\tau)P\rho(\tau) = \int_0^t d\tau M(\tau)P\rho(t-\tau), \\ &M(\tau) = PL_1 T\exp\left(-i\int_0^\tau ds\overline{P}L(s)\overline{P}\right)L_1 P. \end{aligned} \tag{23}$$

The memory kernel $M(t)$ has second order in $L_1 \sim \omega_1$. As a consequence the main order master equation is of the form

$$\frac{\partial}{\partial t} P\rho = -\int_0^t d\tau \left(\left\langle L_1 \exp\left(-i\int_\tau^t ds L_0(s)\right)L_1 \right\rangle_n P\rho(\tau) \right)_D = -\int_0^t d\tau M_0(t-\tau)P\rho(\tau). \tag{24}$$

It is taken into account here, that $L_0(t_1)L_0(t_2) = L_0(t_2)L_0(t_1)$ (therefore Texp is not necessary), and action of L_0 on nondiagonal operators produce nondiagonal operator as well (therefore $\overline{P}$ is not necessary).

Substituting here $L_0(t) = \omega_l(t)I_z^\times$ and $L_1 = \omega_1 I_x^\times$, using basic commutators $[I_z, I_\pm] = \pm I_\pm$, $[I_+, I_-] = 2I_z$, and taking into account that

$$\exp\left(-i\int_\tau^t ds L_0(s)\right)L_1 P\rho(\tau) = \left[\exp\left(-i\int_\tau^t ds H_0(s)\right)H_1 \exp\left(i\int_\tau^t ds H_0(s)\right), P\rho(\tau)\right]$$

we receive

$$\begin{aligned} &\frac{\partial}{\partial t} P\rho = -\frac{\omega_1^2}{4}\int_0^t d\tau \left[I_+ + I_-, \left[I_+ \left\langle e^{-i\Delta(t-\tau)-i\varphi(t,\tau)} \right\rangle_n + I_- \left\langle e^{i\Delta(t-\tau)+i\varphi(t,\tau)} \right\rangle_n, P\rho(\tau) \right] \right]_D = \\ &= -\frac{\omega_1^2}{4}\int_0^t d\tau \left\{ \left[I_+, \left[I_- \left\langle e^{i\Delta(t-\tau)+i\varphi(t,\tau)} \right\rangle_n, P\rho(\tau) \right] \right] + \left[I_-, \left[I_+ \left\langle e^{-i\Delta(t-\tau)-i\varphi(t,\tau)} \right\rangle_n, P\rho(\tau) \right] \right] \right\}, \end{aligned} \tag{25}$$

where $\varphi(t,\tau)=\int_\tau^t ds\omega_l(s)$. Therefore

$$\frac{\partial J_z(t)}{\partial t}=-\frac{\omega_1^2}{4}\int_0^t d\tau Tr\left\{\left(\left[\left[I_z,I_+\right],I_-\right]\left\langle e^{i\Delta(t-\tau)+i\varphi(t,\tau)}\right\rangle_n+\left[\left[I_z,I_-\right],I_+\right]\left\langle e^{-i\Delta(t-\tau)-i\varphi(t,\tau)}\right\rangle_n\right)P\rho(\tau)\right\}.$$

The function $F_0(t-\tau)=\left\langle\exp\left(i\varphi(t,\tau)\right)\right\rangle_n=\left\langle\exp\left(-i\varphi(t,\tau)\right)\right\rangle_n$ represents free induction decay, because

$$\begin{aligned}F_0(t)&=\left\langle I_+(t,\Omega=0)\mathrm{I}_-\right\rangle/\left\langle I_+\mathrm{I}_-\right\rangle=\left\langle I_+\exp\left(-i\int_0^t dsL_0(s)\right)I_-\right\rangle/\left\langle I_+I_-\right\rangle=\\&=\left\langle\exp\left(i\int_0^t dsH_0(s)\right)I_+\exp\left(-i\int_0^t dsH_0(s)\right)I_-\right\rangle/\left\langle I_+I_-\right\rangle,\end{aligned}\tag{26}$$

that corresponds to evolution under influence of local field only.

Now, after calculation of the commutators,

$$\begin{aligned}&\frac{\partial J_z(t)}{\partial t}=-\omega_1^2\int_0^t d\tau\cos\left(\Delta\left(t-\tau\right)\right)F_0(t-\tau)J_z(\tau)=\\&=-\omega_1^2\int_0^t d\tau\cos\left(\Delta\tau\right)F_0(\tau)J_z(t-\tau)=-\int_0^t d\tau\,W_0(\tau)J_z(t-\tau),\\&W_0(\tau)=\omega_1^2\cos\left(\Delta\tau\right)F_0(\tau)=Tr\left(I_zM_0(\tau)I_z\right)/Tr\left(I_z^2\right).\end{aligned}\tag{27}$$

Last relation here is evident from the preceding calculations. The Eq. (27) is similar to Eq.(19), it can be transformed to local in time (Markov) form for small ω_1 by the same way, expanding upper limit of the integral to infinity and replacing $J_z(t-\tau)$ by $J_z(t)$. As a result for $t>T_2$ we obtain

$$\frac{\partial J_z(t)}{\partial t}=-R(\Delta)J_z(t),\quad R(\Delta)=\int_0^\infty dt\,W_0(t)=\pi\omega_1^2g(\Delta),\quad g(\Delta)=\frac{1}{2\pi}\int_{-\infty}^{\infty}dte^{i\Delta t}F_0(t).\tag{28}$$

Direct application of the definition (2) produces famous relation for the free induction decay within the AWK theory:

$$F_0(t)=\left\langle e^{i\varphi(t,0)}\right\rangle_n=\exp\left(-\frac{1}{2}\int_0^t d\tau_1d\tau_2\left\langle\omega_l\left(\tau_1\right)\omega_l\left(\tau_2\right)\right\rangle_n\right)=\exp\left(-M_2\int_0^t d\tau\left(t-\tau\right)\kappa\left(\tau\right)\right).\tag{29}$$

First condition of applicability of the Eq. (28) can be received again by retaining in (27) the term, linear in τ, that produce refined equation

$$\frac{\partial}{\partial t}J_z=-\omega_1^2\int_0^\infty d\tau\cos\left(\Delta\tau\right)F_0(\tau)\left(J_z(t)-\tau\frac{\partial}{\partial t}J_z(t)\right)=-R\left(\Delta\right)J_z+\vartheta\frac{\partial}{\partial t}J_z,\tag{30}$$

$$\vartheta=\omega_1^2\int_0^\infty dt\cdot t\cos\left(\Delta t\right)F_0(t)\le\omega_1^2\int_0^\infty dt\cdot tF_0(t)\sim\omega_1^2T_2^2=R_0T_2.\tag{31}$$

Therefore new term is negligible if $\vartheta\ll1$, and condition $\varepsilon_1\ll1$ is sufficient, but the condition $\vartheta\le R(\Delta)T_2$ is not fulfilled here, contrary to Eqs. (21), because $R(\Delta\tau_c\to\infty)$ decays exponentially (as a Fourier transform of a smooth function), while $\vartheta\left(\Delta\to\infty\right)\sim\Delta^{-2}$. Second and main condition of the applicability of perturbation theory must be connected with the correlation time τ_c, because for $\tau_c=\infty$ kinetic equation produces absolutely wrong result.

Indeed, if local field is static and $\Delta = 0$, then every spin of the ensemble evolves by rotation with the frequency Ω around the effective field $\mathbf{\Omega} = (\omega_1, 0, \omega_l)$, which forms the angle $\chi = \arccos\left(\omega_l / \left(\omega_l^2 + \omega_1^2\right)^{1/2}\right)$ with initial direction of the spin $\mathbf{J}(t=0) = (0,0,p_0)$. Average in time value of $\mathbf{J}(t)$ is $\overline{\mathbf{J}} = (\mathbf{\Omega}/\Omega)\mathrm{p}_0\cos\chi$, while its z-component is $\overline{J_z}(\mathbf{\Omega}) = p_0\cos^2\chi = p_0\dfrac{\omega_l^2}{\omega_l^2+\omega_1^2}$. Therefore relative deviation of $\overline{J_z}(\mathbf{\Omega})$ from its initial value is $\delta\overline{F(\omega_l)} = \left(p_0 - \overline{J_z}(\Omega)\right)/p_0 = \omega_1^2/\left(\omega_l^2+\omega_1^2\right)$, that after averaging on normal distribution of local fields produces

$$\delta\overline{F} = \int_{-\infty}^{\infty} d\omega_l \frac{\omega_1^2}{\omega_l^2+\omega_1^2}\cdot\frac{\exp\left(-\omega_l^2/(2M_2)\right)}{(2\pi M_2)^{1/2}}. \tag{32a}$$

If $\varepsilon_1 = \omega_1^2 T_2^2 \sim \omega_1^2/M_2 \ll 1$, then the integral can be calculated by the substitution $\exp \to 1$ with the result

$$\delta\overline{F} = \left(\frac{\pi}{2}\right)^{1/2}\frac{\omega_1}{M_2^{1/2}} \sim \varepsilon_1^{1/2} \ll 1 \tag{32b}$$

that contradicts to solution of kinetic equation (28) $F_{kin}(t) = J_z(t)/p_0 = \exp(-Rt)$, which evidently produces $F_{kin}(t\to\infty) = 0$, $\overline{F}_{kin} = 0$, and $\delta\overline{F}_{kin} = 1$. This result indicates that main order master equation (28) is inapplicable, if local field fluctuations are not fast enough.

For more quantitative analysis we should calculate next term $M_1(t)$ of the expansion of the memory kernel (23) in powers of ω_1. It is of the form

$$M_1(t) = -\int_0^t dsdu P L_1 U_0(t,s)\overline{P}L_1 U_0(s,u)\overline{P}L_1 U_0(u,0)\overline{P}L_1 P, \quad U_0(t,s) = \exp\left(-i\int_s^t d\tau L_0(\tau)\right), \tag{33}$$

that produces corresponding correction $W_1(t)$ to the memory function $W_0(t)$ in the Eq. (27)

$$\begin{aligned} &W_1(t) = \mathrm{Tr}\left(I_z M_1(t) I_z\right)/Tr\left(I_z^2\right) = \\ &= -\omega_1^4\int_0^t ds\int_0^s du\left(\left\langle \mathrm{Re}\, e^{i\varphi(t,s)}\,\mathrm{Re}\, e^{i\varphi(u,0)}\right\rangle - \left\langle \mathrm{Re}\, e^{i\varphi(t,s)}\right\rangle\left\langle \mathrm{Re}\, e^{i\varphi(u,0)}\right\rangle\right) \end{aligned} \tag{34}$$

together with correction of the saturation rate R in the Eq. (28):

$$R \to R + R_1, \quad R_1 = \int_0^\infty dt\; W_1(t) = -\omega_1^4\int_0^\infty dt\int_0^t ds\int_0^s du\left(S_1(t-s, s-u, u) - S_0(t-s)S_0(u)\right). \tag{35}$$

Here and below the case $\Delta = 0$ is discussed only. The functions $S_0(t-s) = \left\langle \mathrm{Re}\, e^{i\varphi(t,s)}\right\rangle$ and $S_1(t-s, s-u, u) = \left\langle \mathrm{Re}\, e^{i\varphi(t,s)}\,\mathrm{Re}\, e^{i\varphi(u,0)}\right\rangle$ are introduced in (35). Integrals in (35) are similar to Laplace-convolutions, therefore we will use next variant of well known theorem about Laplace-transformation of the convolution

$$\int_0^\infty dt e^{-\lambda t}\int_0^t ds f(t-s, s) = \int_0^\infty dtds e^{-\lambda(t+s)} f(t,s) \tag{36}$$

together with its evident generalization for multiple convolutions. As a result

$$R_1 = -\omega_1^4 \int_0^\infty dtdsdu \left(S_1(t,s,u) - S_0(t)S_0(u) \right). \tag{37}$$

Direct calculation produces

$$R_1 = R_1^{(+)} + R_1^{(-)}, \qquad R_1^{(\pm)} = -\frac{\omega_1^4}{4} \int_0^\infty dtdsdu e^{-Q(t)-Q(u)} \left(e^{\pm\Psi(t,s,u)} - 1 \right), \tag{38}$$

$$Q(t) = \frac{1}{2} M_2 \int_0^t dudv\ \kappa(u-v) = M_2 \int_0^t du(t-u)\kappa(u), \tag{39}$$

$$\Psi(t,s,u) = M_2 \int_0^t dt' \int_0^u du' \kappa(t'+s+u'). \tag{40}$$

For preliminary qualitative understanding we should recognize, that essential range on t and u of the integrand is of order T_2, while its duration on s has the order τ_c, because with increasing of s we have $S_1(t, s\to\infty, u) \to S_0(t)S_0(u)$ (or $\Psi(t, s\to\infty, u) \to 0$) that produces a rough estimation $R_1 \sim \omega_1^4 T_2^2 \tau_c$.

If $\tau_c \ll T_2$, then this estimation is sufficient, but opposite relation $\tau_c \gg T_2 \sim M_2^{-1/2}$ requires more refined analysis. Below, following to Refs. [5] and [3], we apply rather general form of the local field correlation function

$$\kappa(t) = \left(\frac{T_{2T} + \tau_0}{\sqrt{t^2 + T_{2T}^2} + \tau_0} \right)^{3/2}. \tag{41}$$

This relation incorporates all existing qualitative information about correlations of dipole local fields on impurity nuclei taking into account existence of smooth quadratic in time evolution at $t < T_{2T}$, its transformation into linear in time dependence at $T_{2T} < t < \tau_0$ with consequent transformation to 3d-diffusional asymptotics $\kappa(t) \sim t^{-3/2}$ at $t \gg \tau_0$. It is evident, that $\tau_c \sim T_{2T} + \tau_0$ here.

It will be evident from the calculations that largest value has the term $R_1^{(+)}$ from (38). It can be rewritten as

$$R_1^{(+)} = -\frac{\omega_1^4}{4} \left(\int_0^{T_{2T}} ds + \int_{T_{2T}}^\infty ds \right) \int_0^\infty dtdu\ e^{-Q(t)-Q(u)} \left(e^{\Psi(t,s,u)} - 1 \right) = R_{1<}^{(+)} + R_{1>}^{(+)}. \tag{42}$$

Looking for orders of values we can approximate $R_{1<}^{(+)}$ and $R_{1>}^{(+)}$ as

$$R_{1<}^{(+)} = -\frac{\omega_1^4}{4} \int_0^{T_{2T}} ds \int_0^\infty dtdu\ e^{-Q_<(t)-Q_<(u)} \left(e^{\Psi_<(t,s,u)} - 1 \right), \tag{43a}$$

$$R_{1>}^{(+)} = -\frac{\omega_1^4}{4} \int_{T_{2T}}^\infty ds \int_0^\infty dtdu\ e^{-Q_>(t)-Q_>(u)} \left(e^{\Psi_>(t,s,u)} - 1 \right), \tag{43b}$$

where the indexes ">" and "<" indicate that the functions Q and Ψ are calculated according to definitions (39) and (40) with substitution of $\kappa(\tau)$ by $\kappa_<(\tau) = 1 - (\tau/\tau_1)^2$ and $\kappa_>(t) = \left(\tau_0 / \left(|t| + \tau_0 \right) \right)^{3/2}$ respectively. Here $\tau_1^2 = 4T_{2T} \cdot (T_{2T} + \tau_0)/3$.

Largest value has the term $R_{1<}^{(+)}$. Substitutions $s \to s\tau_1$, $t \to t\tau_1$, $u \to u\tau_1$ give

$$R_{1<}^{(+)} = -\frac{\omega_1^4 \tau_1^3}{4} \int_0^{T_{2T}/\tau_1} ds \int_0^{\infty} dt du \; e^{-M_2 \tau_1^2 (Q_{0<}(t)+Q_{0<}(u))} \left(e^{M_2 \tau_1^2 \Psi_{0<}(t,s,u)} - 1 \right), \tag{44}$$

where new index "0" indicates that inside $Q_{0<}(t)$ and $\Psi_{0<}(t,s,u)$ we have M_2 =1 and τ_1=1. Large parameter $M_2\tau_1^2 \gg 1$ arises in (44), therefore the integrations on variables t and u can be carried out by the Laplace method, but the first term in the bracket produces degenerated quadratic form proportional to $t^2+u^2-2tu(1-s^2)$. As a result the integral on s has logarithmical divergence at s=0. Therefore we should retain in the exponent the cubic term as well. It removes the divergence because $\kappa(\tau)$ decays monotonically. Analysis of $R_{1>}^{(+)}$ is similar, but here we can substitute $T_{2T} \to 0$ without creating nonintegrable divergence at $s=0$, and the divergence is absent at all in $R_1^{(-)}$.

As a result we obtain second condition of applicability of the Eq. (28)

$$\varepsilon_{2s} = R_1 / R_0 \sim R_0 \tau_c \left(1 + \left(T_{2T} \tau_0 \right) / \tau_c^2 \ln^2 \left(T_{2T}^3 / \left(T_2^2 \tau_0 \right) \right) \right)^{1/2} \ll 1 \tag{45}$$

that for $T_{2T} \sim \tau_0 \sim \tau_c$ is equivalent to

$$\varepsilon_{2s} = R_1 / R_0 \sim R_0 \tau_c \left(1 + \ln^2 \left(\tau_c / T_2 \right) \right)^{1/2} \ll 1. \tag{46}$$

The index s in ε_{2s} recalls about smooth behavior of $\kappa(t)$ near $t=0$. Singular behavior like $\kappa(t) = e^{-|t|/\tau_0}$ or $\kappa_>(t) = \left(\tau_0 / \left(|t| + \tau_0 \right) \right)^{3/2}$ produce no nonintegrable divergence at $s=0$ and simple condition $\varepsilon_2 \ll 1$ is sufficient. It follows from (45) at $T_{2T} \to 0$.

3. Very slow evolution of local fields

If the local field evolves very slowly, then according to the adiabatic theorem of Landau-Majorana-Stückelberg-Zener [15] the projection $\mathbf{J}(t)\mathbf{\Omega}(t)/\Omega(t)$ of the spin $\mathbf{J}(t)$ on the effective field $\mathbf{\Omega}(t) = \left(\omega_1, 0, \omega_l(t) \right)$ is adiabatic invariant. We can suppose that $\tau_c \gg T_2$ and introduce the time of averaging T_{av} for which $\tau_c \gg T_{av} \gg T_2$. The evolution starts from initial state ρ_0 (4) and after the short time T_{av}, as well as in the Eq. (32), $\overline{J_z}(t) = p_0 \left(1 - \delta \overline{F} \right)$. Here and below upper bar indicates averaging during the time T_{av}. This kind of averaging is sufficient to derive the Eq. (32) in difference of averaging on the time scale $\sim R^{-1}$, which was necessary to obtain $\overline{F}_{kin} = 0$ in preceding section. According to (32) $\delta \overline{F} \sim \varepsilon_1^{1/2} \ll 1$, that will be considered as negligible below. With this accuracy later evolution starts from $\overline{J_z}(t = T_{av}) = p_0$. Absolute majority of the time $|\omega_l(t)| \gg \omega_1$, and, as a result of the adiabatic theorem, at this time $\overline{J_z}(t) = \pm p_0$ corresponding to the sign of $\omega_l(t)$. Therefore in this conditions

$$F(t) = \frac{\langle I_z(t) I_z \rangle}{\langle I_z^2 \rangle} = \langle sign(\omega_l(t)) \cdot sign(\omega_l(0)) \rangle_n. \tag{47}$$

Further calculation should be based on main definition (2). Using the Fourier-transformation we have

$$sign(x)=\int_{-\infty}^{\infty}\frac{dq}{2\pi}\cdot e^{iqx}s(q),\qquad s(q)=\int_{-\infty}^{\infty}dxe^{-iqx-\eta|x|}sign(x)=-\frac{2iq}{\eta^2+q^2},\qquad \eta\to+0\,. \quad (48)$$

Later

$$\begin{aligned}F(t)&=\int_{-\infty}^{\infty}\frac{dq_1dq_2}{(2\pi)^2}s^*(q_1)s(q_2)\left\langle e^{-iq_1\omega_l(t)+iq_2\omega_l(0)}\right\rangle_n=\\&=\int_{-\infty}^{\infty}\frac{dq_1dq_2}{(2\pi)^2}s^*(q_1)s(q_2)\exp\left[-\frac{M_2}{2}\left(q_1^2+q_2^2-2q_1q_2\kappa(t)\right)\right].\end{aligned} \quad (49)$$

It is evident from (48) and (49) that

$$\frac{d}{d\kappa(t)}F(t)=4M_2\int_{-\infty}^{\infty}\frac{dq_1dq_2}{(2\pi)^2}\exp\left[-\frac{M_2}{2}\left(q_1^2+q_2^2-2q_1q_2\kappa(t)\right)\right]=\frac{2}{\pi\left(1-\kappa^2(t)\right)}. \quad (50)$$

Integration of the last equation produces final result

$$F(t)=1+\frac{2}{\pi}\int_1^{\kappa(t)}\frac{dy}{\left(1-y^2\right)^{1/2}}=\frac{2}{\pi}\arcsin\kappa(t)\,. \quad (51)$$

Estimation of corrections to the relation (51) and elucidation of its range of applicability requires much more complex calculations, than the transformation from (47) to (51). It is natural as well as receiving of main order master equation (28) was much simpler, then derivation of the conditions of its applicability (45) and (46).

Standard condition of applicability of the adiabatic theorem on one trajectory requires

$$\varepsilon_{ad1}=\max\left|\frac{d}{dt}\mathbf{n}(t)\right|/\omega_1\ll 1,\quad \mathbf{n}(t)=\frac{\mathbf{\Omega}(t)}{\Omega(t)}. \quad (52)$$

Direct calculation produces

$$\left|\frac{d}{dt}\mathbf{n}(t)\right|/\omega_1=\frac{1}{\omega_1^2+\omega_l^2}\left|\frac{d\omega_l}{dt}\right|. \quad (53)$$

For very rough estimation simplest calculation gives

$$\varepsilon_{ad}^{(0)}=\left\langle\left(\frac{1}{\omega_1^2}\frac{d}{dt}\omega_l\right)^2\right\rangle_n^{1/2}=\frac{M_2^{1/2}}{\omega_1^2\tau'}\sim\frac{1}{\omega_1^2\tau' T_2},\qquad \tau'=\left|\frac{\partial^2\kappa(t=0)}{\partial t^2}\right|^{-1/2}\sim\tau_c\,. \quad (54)$$

More refined calculations (similar to derivation of (51)) produce less restrictive value

$$\varepsilon_{ad}^{(1)}=\left\langle\left(\frac{1}{\omega_1^2+\omega_l^2}\cdot\frac{d\omega_l}{dt}\right)^2\right\rangle_v^{1/2}\sim\left(\frac{1}{\omega_1^3\tau'^2T_2}\right)^{1/2}\sim\left(\omega_1T_2\right)^{1/2}\varepsilon_{ad}^{(0)}\ll\varepsilon_{ad}^{(0)}, \quad (55)$$

which should be more reliable, because main nonadiabatic decrease of the spin polarization take place near $\omega_l(t)\sim\omega_1$. Relation (55) contains suppression of contribution of $\omega_l(t)\gg\omega_1$, while in (54) the suppression is absent.

According to the adiabatic theorem [15] decrease of the polarization during one passage of the range $\omega_l\sim\omega_1$ is $\delta_{nad}=\exp\left(-\pi/\varepsilon_{ad}\right)\ll 1$, frequency of such passages $W_{nad}\sim 1/\tau_c$, therefore nonadiabatic losses of polarization should follow the law $\exp\left(-\delta_{nad}W_{nad}t\right)$. Accounting it we get

$$F(t) = \frac{2}{\pi}\arcsin\kappa(t)\cdot\exp\left(-\delta_{nad}W_{nad}t\right). \quad (56)$$

The spin-lattice relaxation should be considered separately of course.

We expect, that the relation (56) can be useful in studies of quasi-Ising spin systems by the magnetic resonance of impurity spins and in quantum information processing, therefore additional theoretical and experimental studies are necessary.

4. Conclusions

The model (1) is very important in spin dynamics and physical kinetics. Content of the lecture bridges existing gaps in known textbooks and, we hope, will give new possibility for applications of the magnetic resonance.

References

[1] Abragam A. Principles of Nuclear Magnetism. Oxford University Press, Oxford (1961).

[2] Bulgakov M.I., Gul'ko A.D., DzheparovF.S., Stepanov S.V., Trostin S.S. Spin-fluctuation spectrum and NMR of beta-active 8Li nuclei in LiF crystals: from the method of memory functions to cumulant expantions. JETP Lett. **58**, 592, 1993.

[3] Abov Y.G., Gulko A.D., Dzheparov F.S., Stepanov S.V., Trostin S.S. Statistical dynamics of spin systems and beta-NMR spectroscopy. Phys. Part. Nucl. **26**, 692, 1995.

[4] Abov Y.G., Bulgakov M.I., Borovlev S.P., Gul'ko A.D., Garochkin V.M., Dzheparov F.S., Stepanov S.V., Trostin S.S., Shestopal V.E. Investigation of a disordered spin system of the ^{8}Li-^{6}Li nuclei in LiF crystals by the method of beta-NMR spectroscopy. Sov. Phys. JETP **72**, 534, 1991.

[5] Dzheparov F.S. Transport of spin polarization in a system of disperse and random walks in disordered media. Sov Phys JETP **72**, 546, 1991.

[6] Abov Y.G., Gulko A.D., Dzheparov F.S., Ermakov O.N., Lvov D.V., Lyubarev A.A. Investigation of the External-Magnetic-Field Dependence of Polarization Transfer in a ^{8}Li–^{6}Li Disordered Nuclear System. Physics of Atomic Nuclei **77**, 682, 2014.

[7] Salikhov K.M., Semenov A.G., Tsvetkov Yu.D. Electron Spin Echo. Nauka, Novosibirsk 1976.

[8] Dzheparov F.S., Lvov D.V., Veretennikov M.A. Phase Relaxation in Disordered Nuclear Paramagnets. JETP Lett. **98**, 484, 2013.

[9] Dzheparov F.S., Lvov D.V., Veretennikov M.A. Spin-spin relaxation in magnetically dilute crystals. Low Themp. Phys. **41**, 9, 2015.

[10] Alexandrov I.V. Theory of Marnetic Relaxation. Nauka, Moscow, 1975.

[11] Burshtein A.I. Lectures on Quantum Kinetics. Novosibirsk State University, Novosibirsk, 1968.

[12] Abragam A., Goldman M. Nuclear magnetism: order and disorder. Clarendon, Oxford 1982.

[13] Dzheparov F.S. Ergodic theorem for an impurity spin subsystem in a paramagnet. JETP **89**, 753, 1999.

[14] Dzheparov F.S. Interplay of clssical and quantum spin dynamics. Magnetic Resonance in Solids. Electronic Journal **14**, 12201, 2012.

[15] Di Giacomo F., Nikitin E.E. The Majorana formula and the Landau-Zener-Stückelberg treatment of the avoided crossing problem. Physics-Uspekhi **48**, 515, 2005.

Combination and recombination of free radical paramagnetic centers in heavy petroleum fractions

M. Dolomatov[1,2], A. Rodionov[3], M. Gafurov[3], A. Petrov[4], V. Izotov[3], S. Makarchikov[3], R. Bakhtizin[1], I. Khairutdinov[4], S. Orlinskii[3]

[1]Bashkir State University, Ufa, Russia

[2]Ufa State Petroleum Technical University,Ufa, Russia

[3]Kazan Federal University, 420008 Kazan, Russia

[4]Institute of Petroleum Refining and Petrochemistry, Ufa, Russia

e-mail: Marat.Gafurov@kpfu.ru

A typical petroleum fluid can be considered as a petroleum disperse system (PDS) — a hybrid of a solution and a colloidal dispersion (of crystallizing waxes, self-associating asphaltenes, etc.) [[1]]. The understanding of complex behavior of PDS under the thermal treatment is expected to be a challenge. Nevertheless, as it was stressed by Evdokimov et al., relatively simple experiments on only one of the PDS components can shed light on details of phase transformations in such systems [2,3].

As one of the constituents of PDS, a paramagnetic phase can be the subject of interest: one gram of PDS contains 10^{16} – 10^{21} paramagnetic centers (PC, [4-6]). The majority of PC is concentrated in the high-molecular PDS components such as asphaltenes, resins and polycyclic aromatic hydrocarbons (PAH). The content of the high-molecular PDS components could reach the values of 45 wt% in native oils and up to 73 wt% in natural asphalts and bitumen [4]. Assuming that asphaltenes and resins have molecular weight of about 1000 amu [4], they could contain up to one unpaired electron per molecule. Obviously, such high concentration of PC should (or could) affect not only the paramagnetic properties of substance but (at least partially) also the electrical qualities of PDS.

Electrical properties of asphaltenes and bitumen are the matter of intensive research for decades and briefly reviewed in [7,8]. It was shown that the temperature dependence of the electrical conductivity in some PDS resembles those for the organic broadband semiconductors [7,9-11]. But there is no detailed description of the process(es) that would adequately describe the thermal generation-recombination of PC in PDS [12]. Among numerous additional motivations to investigate the processes of generation-recombination of PC in PDS, the most significant are related to understanding the mechanisms of photodegradation – the PC linewidth and radicals number decreases with sunlight irradiation time of some tenth of hours [13], as well as by the discrepancies in the PC concentrations derived from the conventional and pulsed EPR measurements [14]. An attempt to present a corresponding

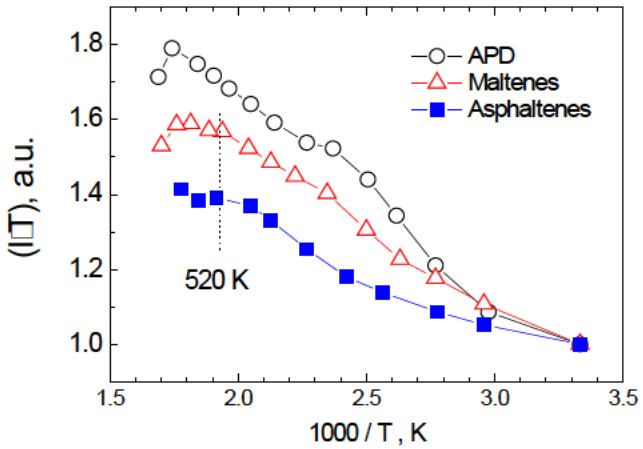

Fig.1. Dependencies of relative EPR intensities of free radicals multiplied by the absolute temperature on the reverse absolute temperature for asphalt (APD) and its fractions

kinetic model using asphalt (APD) and its fractions (asphaltenes and maltenes) with the parameters derived experimentally is given in this work.

Reference

[1] Z.I. Syunyaev Concentration of complex structural units in disperse petroleum systems, and methods for regulation of this concentration Chemistry and Technology of Fuels and Oils July 1980, Volume 16, Issue 7, pp 484-489

[2] Evdokimov I.N., Eliseev N.Yu., and Eliseev D.Yu. 2001. Rheological evidence of structural phase transitions in asphaltene-containing petroleum fluids. J. Petrol. Sci. Eng. 30(3-4): 199-211.

[3] Evdokimov I.N., Eliseev N.Yu., and Eliseev D.Yu. 2004. Effect of asphaltenes on the thermal properties of emulsions encountered in oil recovery operations. Fuel. 83(7-8): 897-903.

[4] Yen T.F., Chilingarian G.V. (Editors), Asphaltenes and asphalts, 2. Developments in petroleum science. 40 B. USA: Elsiever, 2000. 622 p.

[5] Yen, T.; Chilingarian, G.V. Asphaltenes and Asphalts. 1. Developments in Petroleum Science, 40A; Elsevier: New York, 1994; 459 p.

[6] Volodin M.A., Mamin G.V., Izotov V.V., Orlinskii S.B. // Journ. of Physics: Conference Series. 2013. V.478. №1. 012002.

[7] I.N. Evdokimov, A.P. Losev. Electrical Conductivity and Dielectric Properties of Solid Asphaltenes. Energy Fuels 2010, 24, 3959-3969

[8] A. Hosseini, E. Zare, S. Ayatollahi, F.M. Vargas, W. G. Chapman, K. Kostarelos, V. Taghikhani. Electrokinetic behavior of asphaltene particles Fuel 178 (2016) 234–242

[9] M. Dolomatov, S. Dezortzev, S. Shutkova. Asphaltenes of Oil and Hydrocarbon Distillates as Nanoscale Semiconductors. Journal of Materials Science and Engineering B 2 (2) (2012) 151-157

[10] Grechishkin V S, Ainbinder N E "Radiospectroscopy of organic semiconductors" Sov. Phys. Usp. 10 237–255 (1967);

[11] V.E. Zhivulin, L.A. Pesin, D.V. Ivanov. Special aspects of the temperature dependence of EPR absorption of chemically carbonized polyvinylidene fluoride derivatives Physics of the Solid State January 2016, Volume 58, Issue 1, pp 86-90

[12] Wang W., Ma Y., Li S., Shi J., Teng J. // Energy & Fuels. 2016. V.30. №2. p.830

[13] Carmen L. B. Guedes, Eduardo Di Mauro, Ariana De Campos, Leandro F. Mazzochin, Gislaine M. Bragagnolo, Fernando A. De Melo, and Marilene T. Piccinato EPR and Fluorescence Spectroscopy in the Photodegradation Study of Arabian and Colombian Crude Oils Hindawi Publishing Corporation International Journal of Photoenergy Volume 2006, Article ID 48462, Pages 1 – 6 DOI 10.1155/IJP/2006/48462

[14] Mamin GV, Gafurov MR, Yusupov RV, Gracheva IN, Ganeeva YM, Yusupova TN, Orlinskii SB. Toward the Asphaltene Structure by Electron Paramagnetic Resonance Relaxation Studies at High Fields (3.4 T) Energy Fuels 2016, Vol. 30 (9) 6942-6946

Anisotropic exchange interaction in low dimensional systems

Z. Seidov[1,2], T.P. Gavrilova[3,4], R.M. Eremina[3,4], L.E. Svistov,[5] A.A. Bush,[6] A. Loidl[1], H.-A. Krug von Nidda[1]

[1] Experimental Physics V, Center for Electronic Correlations and Magnetism, University of Augsburg, D-86135 Augsburg, Germany

[2] Institute of Physics, Azerbaijan National Academy of Sciences, H. Cavid pr. 33, AZ-1143 Baku, Azerbaijan

[3] E. K. Zavoisky Physical-Technical Institute RAS, 420029 Kazan, Russia

[4] Kazan (Volga region) Federal University, 420008 Kazan, Russia

[5] P.L. Kapitza Institute for Physical Problems RAS, 119334 Moscow, Russia

[6] Moscow Institute of Radiotechnics, Electronics, and Automation, RU-117464 Moscow, Russia

e-mail: REremina@yandex.ru

Frustration in quasi-one-dimensional (1D) chain magnets is provided by competing interactions, f the nearest neighbor (NN) exchange is ferromagnetic and the next-nearest neighbor (NNN) exchange is antiferromagnetic. Numerical investigations of frustrated chain magnets within different models have predicted a number of exotic magnetic phases, such as planar, spiral, and different multipolar phases. Moreover, theoretical studies show that the magnetic phases are very sensitive to inter-chain interactions and anisotropic interactions in the system. Here we concentrate on $LiCu_2O_2$ with its fascinating interplay of competing exchange interactions both within the Cu^{2+} chains and the zigzag-ladders formed by neighboring two chains. Detailed investigations to resolve the phase diagram of $LiCu_2O_2$ have been performed by means of magnetization and dielectric measurements as well as neutron scattering, electron spin resonance (ESR), and nuclear magnetic resonance (NMR) studies. Basically, a susceptibility maximum at a temperature T_{max} = 38 K typical for a low-dimensional antiferromagnet and two subsequent phase transitions at T_{N1} =24.5 K and T_{N2} = 23 K [1] into the spin-spiral structure, where the latter is accompanied by the occurrence of ferroelectricity, characterize the magnetic and electric properties of $LiCu_2O_2$ at low magnetic fields. We present a quantitative analysis of the angular dependence of the paramagnetic resonance linewidth in $LiCu_2O_2$ to determine the anisotropic exchange parameters. For this purpose ESR is the method of choice, because the anisotropy of the line broadening is extremely sensitive to anisotropic interactions, while the isotropic exchange contributions only result in a general isotropic narrowing of the ESR signal.

The ESR measurements were performed in a Bruker ELEXSYS E500-CW spectrometer equipped with continuous flow He cryostats (Oxford Instruments) at *X*- (9.4 GHz) frequency in the temperature range 4.2 < T< 300 K. A single exchange-narrowed Lorentz-shaped absorption line with g values g_c =2.22 and g_a=g_b= 2.05 at a microwave frequency of 9 GHz was observed. In the case of sufficiently strong exchange interaction the ESR linewidth can be analyzed in terms of the high-temperature approach ($k_BT >> J$).

$$\Delta H = \frac{\hbar M_2}{g\mu_B\omega_{ex}}, \quad (1)$$

where M_2 is the second moment of line. Second moment can be expressed in terms of the microscopic parameters of the Hamiltonian of the spin system as:

$$M_2 = \frac{\left\langle \left[H_{an}, S^+ \right] \left[S^-, H_{an} \right] \right\rangle}{\hbar^2 \left\langle S^+ S^- \right\rangle}. \qquad (2)$$

Here g — denotes the g value, $\hbar$ — the Planck constant, and μ_B — the Bohr magneton. The second moment M_2 and the exchange frequency ω_{ex} can be expressed via microscopic Hamiltonian parameters H_{int}. The second moment shows orientation dependence with respect to the external magnetic field, which is characteristic for the anisotropic interaction responsible for the line broadening.

The consideration of the exchange-paths symmetry shows that any antisymmetric anisotropic- exchange contributions are forbidden. Therefore, below we will speak about symmetric anisotropic-exchange interactions, only. To evaluate the two anisotropic exchange contributions in H_{int}, one has to consider the respective bond geometries. For each anisotropic exchange contribution a local coordinate system has to be defined such that the corresponding tensor of anisotropic interaction is diagonal and the sum of diagonal elements equals zero. One of the local axes is directed along the exchange bond. The directions of the two other axes are defined by the symmetry of the local environment. As indicated in fig.1 for the intra-chain anisotropic exchange interaction $\mathbf{J_2}$ the local axes are defined as: x' - along the O-O direction within the chain, y' - along the Cu-Cu direction within the chain, and z' - perpendicular to the plane spanned by the Cu-O2 ribbons within the chain. The local axes of the intra-ladder anisotropic exchange between neighboring chains $\mathbf{J_1}$ are chosen as: x'' - along the Cu-Cu direction between neighboring chains, y'' - perpendicular to the plane spanned by the Cu-O-Cu bridge between neighboring chains, and z'' - perpendicular to x'' and y'' axes.

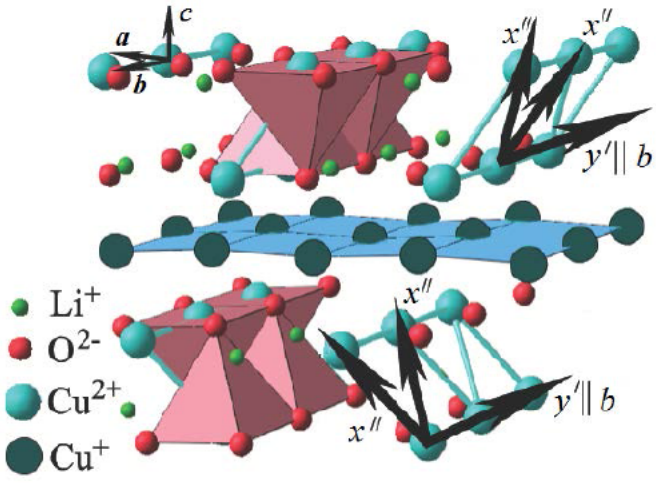

Fig.1. Orthorhombic crystal structure of $LiCu_2O_2$. The spin ladders along the b axis are formed by edge-sharing pink $Cu^{2+}O_5$ pyramids. The light blue Cu^+ planes separate the structure into layers perpendicular to the c axis. Black arrows indicate the crystallographic coordinates a; b; c, the inter-chain local coordinate y', as well as the inter-ladder coordinate x'' to describe the local anisotropic exchange tensors.

In the unit cell there are two different ladders which both consist of two chains. In the following expressions the upper and lower signs correspond to the directions of the individual vectors for different ladders. In the crystallographic coordinate system (a; b; c) the unit vectors of the local coordinate systems of the intra-chain anisotropic exchange $\mathbf{J_2}$ read (x' 0.982, 0, ∓0187; y' 0, 1, 0; z' ±0.187, 0, 0.982) for first and second ladder, respectively. This means that only local y' axis coincides with the crystallographic b axis parallel to the

Cu^{2+} chains where as x' and z' axes are slightly rotated from a and c axes, respectively. In the first ladder the unit vectors of the local coordinate system of the intra-ladder anisotropic exchange $\mathbf{J_1}$ are given by (x'' 0.460, ±0.463, 0.758; y'' ∓0.725, 0.689, ±0.018; z'' ∓0.513, ∓0.557, 0.653) for first and second super-exchange bond, respectively. Analogously, for the second ladder the unit vectors of the local coordinate systems of $\mathbf{J_1}$ are given by (x'' –0.460, ±0.463, 0.758; y'' ∓0.725, –0.689, ∓0.018; z'' –0.513, ±0.557, –0.653). The details of second-moment calculations for anisotropic-exchange interactions are presented in [2]. The intra-chain anisotropic contribution $\mathbf{J_2}$ can be adopted from the identical ionic configuration in the related compound LiCuVO4, where we considered the same so called ring-exchange geometry of the Cu-O2 ribbons yielding $Jcc^2 = 2$ K [2]. The remaining intra-ladder anisotropic contribution $\mathbf{J_1}$ needs a deeper analysis which will be discussed in the following.

The schematic pathway of the relevant anisotropic spin-spin coupling $\mathbf{J_1}$ between two neighboring chains within the same ladder is illustrated in fig.2. Here we use local coordinates *x; y; z* adapted to the conventional rotation of the unperturbed *d*- orbitals neglecting distortion of lattice and any mixing of the wave functions. We consider the case where the hole ground state dx^2-y^2 is coupled with the excited *dxz* state by spin-orbit interaction (fig.2). Following this scheme, we estimate the intra-ladder anisotropic exchange parameter *Ayy* according to [3]:

$$A_{yy} = \frac{1}{2}\frac{\lambda^2}{\Delta^2_{x^2-y^2,xz}}\left(\left\langle x^2-y^2\left|l_y\right|xz\right\rangle\right)^2 J_{x^2-y^2,xz}. \qquad (3)$$

$J_{x^2-y^2,xz}$ denotes the corresponding isotropic exchange integral, which is significantly larger than J_1. Our estimation of the isotropic exchange interaction parameter between the ground and excited states is quite rough and probably strongly overestimated because of the idealized geometry. Therefore, to calculate the anisotropic exchange interaction we used a ratio $J_{xz;x^2-y^2} = 5J_1$ which most closely coincides with experimental values. Using (3) and all data derived microscopic parameters, we get A_{yy} = 3,5 K that cannot be neglected compared to the isotropic exchange. As indicated in fig.1 for the two different Cu^{2+} ladders, the rotation of the theoretically predicted main values of the tensors of the symmetric anisotropic exchange interaction from the local coordinate system to the crystallographic coordinate system leads to two symmetric tensors (in K):

$$J_1 = \begin{vmatrix} 0.52 & \pm 1.72 & -0.32 \\ \pm 1.72 & 0.58 & \mp 0.33 \\ -0.32 & \mp 0.33 & -1.1 \end{vmatrix}, \quad J_1 = \begin{vmatrix} 0.52 & \pm 1.72 & 0.32 \\ \pm 1.72 & 0.58 & \pm 0.33 \\ 0.32 & \pm 0.33 & -1.1 \end{vmatrix}.$$

These tensors have to be compared to the experimental results below.

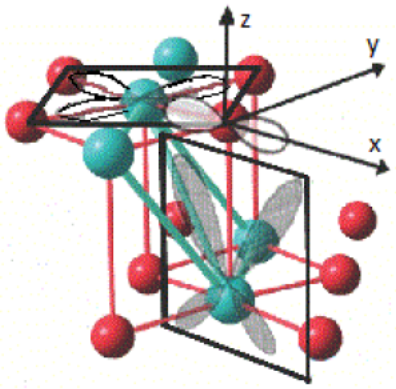

Fig.2. Schematic pathway of the origin of the anisotropic spin-spin coupling *Ayy* between copper *dx*2-*y*2 states with an copper *dx*2-*y*2 states with an excited copper *dxz* state via oxygen p_c^x states.

Now we focus on the angular dependence of the linewidth depicted in fig.3 for $T = 300$ K. The maximum of the linewidth is found for $H||a$, the minimum for $H||b$ and an intermediate value for $H||c$ indicating the leading anisotropic exchange contribution to be connected to the *a* direction. To fit the angular dependencies of the ESR linewidth in $LiCu_2O_2$ we used method in [2]. The isotropic exchange parameters were taken from [1].

Hence, as fitting parameters we used the components of symmetric anisotropic exchange interactions $\mathbf{J}_{1,2}$. As one can see, the model provides a good agreement between experimental and theoretical data. From the analysis of the angular dependence of the linewidth one obtains the magnitude of the anisotropic exchange interactions. The sign of the anisotropic exchange interaction was derived from the theoretical analysis of exchange bonds.

$$J_2 = \begin{vmatrix} 1.63 & 0 & \mp 0.64 \\ 0 & -0.04 & 0 \\ \mp 0.64 & 0 & -1.6 \end{vmatrix}.$$

For the first and second ladders the inter ladder anisotropic exchange tensor reads:

$$J_1 = \begin{vmatrix} 0.64 & \pm 1.5 & -0.55 \\ \pm 1.5 & 0.51 & \pm 0.49 \\ -0.55 & \pm 0.49 & -1.15 \end{vmatrix}, \quad J_1 = \begin{vmatrix} 0.64 & \mp 1.5 & 0.55 \\ \mp 1.5 & 0.51 & \pm 0.49 \\ 0.55 & \pm 0.49 & -1.15 \end{vmatrix}.$$

The fitting parameters of anisotropic exchange interaction between spins from neighboring chains are close to the theoretical estimations. Note that absolute value is only results for the high-temperature limit $T \approx J/k_B$.

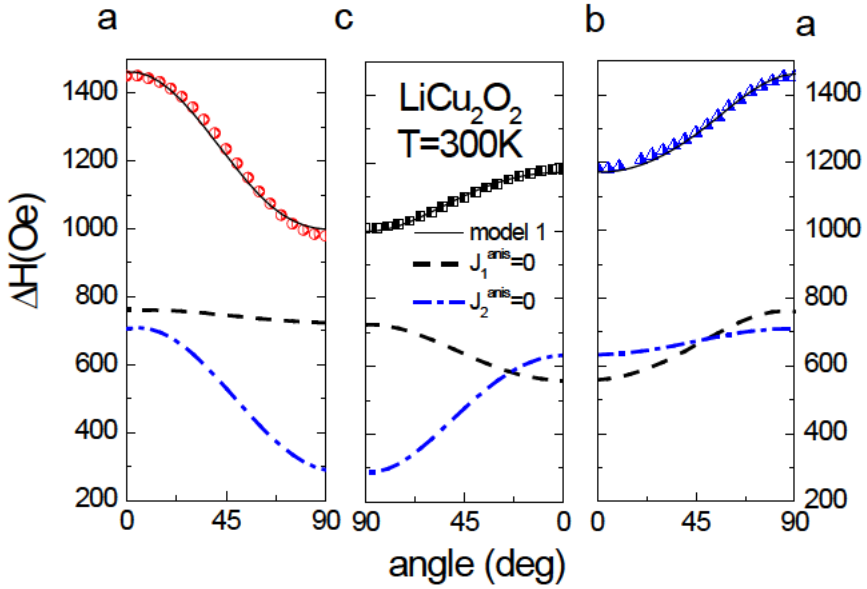

Fig.3. Angular dependence of the linewidth in LiCu2O2 for three perpendicular crystallographic planes at selected temperatures at X-band frequency (solid symbols) and for the ab plane at $T = 300$ K. The dotted solid lines indicate theoretical linewidth when $J_1(\text{anis}) = 0$; the dotted-point lines indicate theoretical linewidth when $J_2(\text{anis}) = 0$.

References

[1] A. A. Bush, N. Buttgen, A. A. Gippius, V. N. Glazkov, W. Kraetschmer, L. A. Prozorova, L. E. Svistov, A. M. Vasiliev, and A. Zheludev, Phys. Rev B **88**, 104411 (2013).

[2] R. M. Eremina, Magnetic Resonance in Solids. Electronic Journal **16**, 14102 (2014).

[3] B. Bleaney and K. D. Bowers, Proc. R. Soc. A 214, 451 (1952).

Resource Center of Probe and Electron Microscopy as an instrumental component of the NRC Kurchatov Institute research infrastructure

M.Yu. Presnyakov

[1]NRC Kurchatov Institute, 123 182, Akademika Kurchatova pl., Moscow, Russia.

e-mail: Presnyakov_MY@nrcki.ru

Resource Center — is an instrumental component of the research infrastructure of NRC “Kurchatov Institute” that includes facilities for a wide variety of measurements, investigations, technological processes and called for the implementation of interdisciplinary research in various areas of convergent science and technology.

Resource Center main goals and objectives:

- Providing prompt and qualitative measurements and investigations using RC facilities;
- Organization of effective and uninterrupted operation of RC in shared mode;
- Development of new measurement techniques in order to expand opportunities and create a new directions in research activities;
- Teaching and training the personnel on the RC facilities;
- Expanding the user community of the RC infrastructure

The resource center of the probe and electron microscopy "NANOPROBE" represented a unique combination of optical, scanning, probe and transmission electron microscopy. A variety of instrument base, as well as opportunities of analytical equipment have allowed reaching a new level of materials research. Results, which were obtain on a hardware basis of RC, allow technologists to regulate the initial stage of the synthesis process of promising materials in the field of semiconductor electronics, superconducting, polymer and bio-organic materials and to achieve the global level results in these areas, in turn, to make the discoveries of a fundamental nature in these areas by the researchers from NRC Kurchatov Institute.

The high level of skills of staff and wide range of equipment corresponding to the best international standards, makes resource center "NANOPROBE" the one of the most advanced in the country.

Unique the Titan transmission electron microscope, equipped with a spherical aberrations corrector, allows you to explore the structure of inorganic nano-materials on a sub angstrem level. With the help of electron-ion scanning microscope Helios held not only the study of the surface morphology of objects with nanometer resolution, in turn, the nanostructuring held by using of the method of the focused ion beam in conjunction with the micromanipulator, and gas injection system. Russia's only cryo-transmission electron microscope Titan Krios, equipped with an image corrector, allows to study of bioorganic objects frozen in a native environment. Probe microscopes allow visualizing the surface of the nano-sized objects under different environmental conditions.

Resource Center of probe and electron microscopy "NANOPROBE" is a research complex of full cycle: from sample preparation until research and analysis of the results at the highest level. Some words about our main directions in science.

Objectives of the RC “NANOPROBE”

- Characterization of the structure, surface and morphology of materials, segmentation and statistical data processing;
- Nanoscale microanalysis and mapping of elementary sample composition;
- 3D structure reconstruction of volume and surface of micro- and nanometer- scale objects;
- Developing modern methods to imagine atomic structure;
- Improving of existing and development of new methods of research and nano-characterization for different materials;
- Sample preparation for electron microscopy studies.

Main objects of investigation

- Semiconductor structures;
- Polymer nanocomposites;
- Superconductors;
- Bioorganic materials;
- Metals;
- Magnetic materials and structures.

Researching methods

- Transmission electron (cryo)microscopy;
- Scanning electron microscopy and FIB technique;
- Scanning probe microscopy;
- Highly precision mechanical and ion polishing facilities for EM- studies.

Some results of our investigations below.

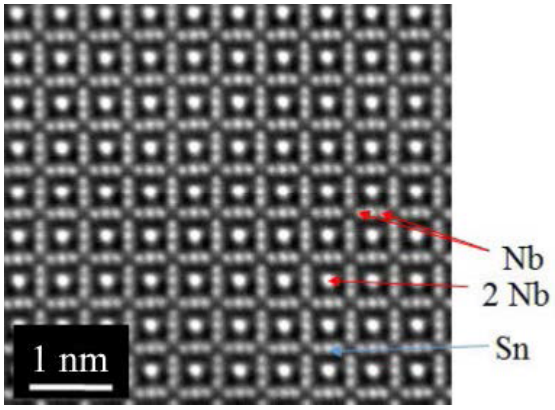

Fig.1. STEM- image of Nb_3Sn superconducting grain

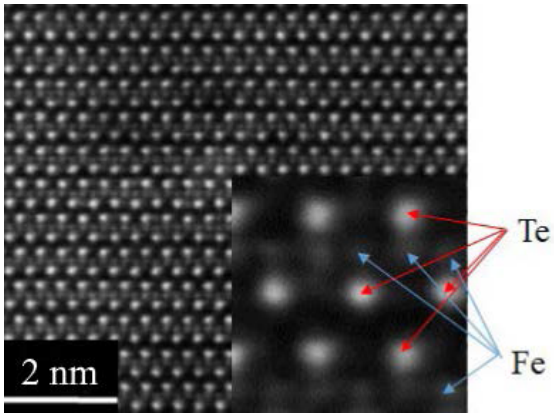

Fig.2. STEM- imge of monocrystalline FeTe structure [1]

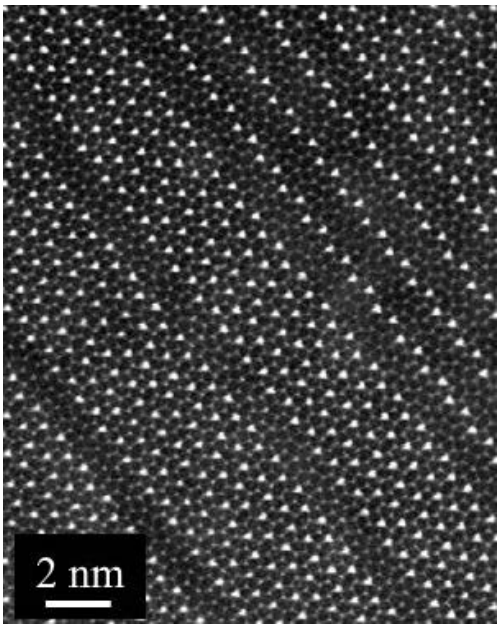

Fig.3. STEM- image of linear defects in AlLaNiFe structure [2]

References

[1] I.O. Shchichko, I.P. Makarova, M.Yu. Presnyakov, S.M. Kazakov, E.V. Antipov, D.A. Chareev, E.S. Mitrofanova, A.A. Mikhutkin, and A.L. Vasil'ev. Single-Crystal Structure Study of Iron Chalcogenides Fe1 + δTe1 – xSx. Crystallography Reports, 2015, Vol. 60, No. 2, pp. 227–235. © Pleiades Publishing, Inc., 2015. DOI: 10.1134/S1063774515020248

[2] A.L. Vasiliev, A.G. Ivanova, N.D. Bakhteeva, N.N. Kolobylina, A.S. Orekhov, M.Y. Presnyakov and E.V. Todorova. Microstructure of the Al-La-Ni-Fe. Crystallography Reports, 2015, Vol. 60, No. 1, pp. 23–29. © Pleiades Publishing, Inc., 2015. DOI: 10.1134/S1063774514060297

Preclinical magnetic resonance imaging

U. Eichhoff

Bruker Biospin GmbH (retired), D76275 Ettlingen, Germany

e-mail: barbara.uwe@t-online.de

Introduction

Magnetic Resonance since more than 60 years is the most powerful method for structural investigation physics, chemistry, biology and has been extended to medical applications. Four Nobel prices have been awarded directly for NMR [1-4]. Today NMR together with X-ray-diffraction is the most powerful method for structure determination of proteins.

Magnetic Resonance Imaging (MRI) [4] added another dimension to NMR and is now well established as the most informative medical imaging method.

MRI is *the* ideal method for preclinical imaging, the non-invasive biomedical and pharmaceutical research on animals [5]. Pathological processes can be followed over a long time period on one single animal. This gives much more reliable results and saves laboratory animals and costs.

Instrumentation

Many universities and research institutions already use analytical NMR spectrometers for biochemical and biomedical investigations on bodyfluids, cell suspensions and tissues. Adding an imaging accessory (gradient unit and probehead) they can extend their research to investigations in living animals. Today special instruments with horizontal magnet bores offer excellent capabilities for developing new imaging methods and strategies. The adaption to (much more expensive) whole body medical imagers is straightforward. In fact most of the current imaging methods have been developed on such small bore systems. Mice can be investigated in a normal wide bore magnet (89 mm) and rats in superwide bore magnets (150 mm). For larger animals systems with horizontal magnets like the permanent magnet system ICON 1T and the superconducting BioSpec and Pharmascan must be used, covering a field range from 1.0 to 17.6 Tesla (fig.1). The horizontal magnets are much more convenient

Fig.1. MRI sytems for preclinical imaging: ICON(1T), BioSpec (4.7, 7.0, 9.4, 11.7, 14.0, 15.2, 17.6 T)

for anesthesia and handling of the animals. They have been carefully designed for maximal field homogeneity and stability and excellent cryogenic performance. Active shielding reduces the strayfield to a minimum and makes siting easier. Cold transportation results in short installation times.

In vivo MRI and MRS

MRI allows to obtain detailed morphological information even in small animals due to its high spatial resolution (<100 μm) almost comparable to optical microscopy (fig.2).

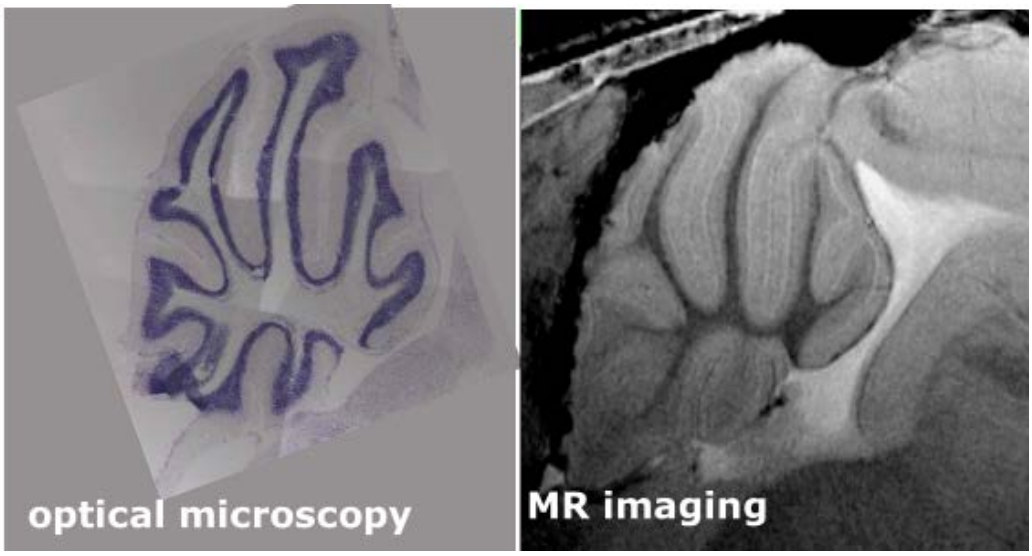

Fig.2. Cerebellum of a mouse left: optical microscopy right: MRI with spatial resolution 30 μm × 30 μm (courtesy of B.Baltes, M.Rudin ETH Zürich)

MR images of the living animal are three-dimensional and any cross section under any angle can be reconstructed. For optical microscopy the animal must be sacrificed to obtain a microtome preparation for each single section.

Fast imaging methods [6-9] extended the temporal resolution into the msec-range allow to follow heart motion in real time and to perform functional imaging in the brain using the fastest available imaging sequences. Blood vessels can be imaged selectively without and with contrast agents and the blood flow parameters can be studied. Additionally chemical information can be obtained with localized spectroscopy and spectroscopic imaging. Endogenous tissue metabolites can be identified at millimolar concentrations and metabolic processes can be monitored.

Applications in pharmaceutical industry

For evaluation of the effectivity of cerebroprotective drugs a cerebral infaction in a rat brain has been initiated by occlusion of the middle cerebral artery. (MCA-O model) [10,11]. The development of ischemia can be followed by various imaging methods. Diffusion-weighted pulse-sequences deliver the best contrast between infarcted and healthy tissue [12]. The combination of diffusion and perfusing weighting allows to determine tissue at risk, which can be recovered [13,14]. Application of a cerebroprotective drug leads to a decrease of the infarcted area. The time window for successful intervention in the rat MCA-O model turned out to be quite narrow, about 2h. This is very close to observation in humans and proves, that the MCA-O in rat is a suitable model for ischemia and infarction in the human brain.

Organ Function

The excellent time resolution of MRI in the millisecond range allows real time cardiac imaging in animals like mice and rats with an almost 10 times higher heartbeat rate than in humans. Cardiac wall motion can be displayed in real time and infarcted regions can be recognized. The regeneration of partially resected organs by can be followed their volume increase and the function of transplanted kidneys can be evaluated from the transition time of a contrast agent.

Oncology

Already the first publications on MRI concentrated on the ability to distinguish various types of neoplastic tissue [15]. Human tumors can be injected into laboratory animals and the tumor growth can be followed. Preclinical applications of MRI in oncology focus on the assessment of tumor volume , perfusion, neovascularization, metabolism and the influence of antitumor drugs on all these parameters.

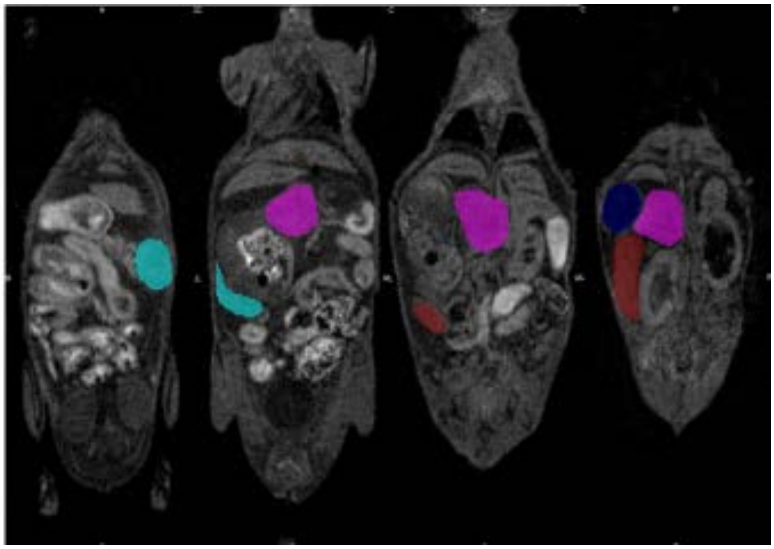

Fig.3. Quantification of a pancreatic tumor in rat from a 3D-iamge obtained at 1.0 Tesla. The pink tumor is the main pancreatic tumor, the turquoise tumor is located next to the stomach and is thought to be a gastric papilloma or a squamous cellcarcinoma. The tumors were found to have the following volumes: Turquoise = 200 mm^3, Pink = 570 mm^3

Transgenic animals and disease models

The latest developments in molecular biology and genome research allow to exclude (knockout) or to modify the genome of animals and to create transgenic animals, which can serve as excellent models for various human diseases. Molecular imaging and rapid phenotyping of transgenic animals have significantly extended the role of MRI/MRS in pharmacology. For instance mice can be genetically modified to overexpress the corticotropin-releasing factor (CRF). CRF is a neurotransmitter and core mediator of endocrine behavioural responses to stress. The mouse model is allocated to psychiatric disorders in humans. When compared to the wild type the adrenals were significantly enlarged and the thymus volume reduced at the same time. This is also true for humans. These in vivo data of the adrenals correlated perfectly with the post mortem weight of the organs.

Diffusion Tensor Imaging (DTI) and Structural Connectivity

If in diffusion weighted imaging direct the diffusion gradient is directed in three perpendicular directions, slightly different images are obtained, because diffusion is observed

along the gradient direction [16]. Mathematically the diffusion must be described as a tensor with three main axes with the main axis $\lambda_1, \lambda_2, \lambda_3$. The diffusion information can be displayed in different ways. In brain the white matter shows a high anisotropy, because diffusion is almost free along the fiber direction and limited perpendicular to it. The vector map in the center shows the local diffusion in the different voxel, the arrows symbolize the signal strength the direction of diffusion. The color coded map on the right shows the main direction of diffusion along the three main coordinates (fig.4).

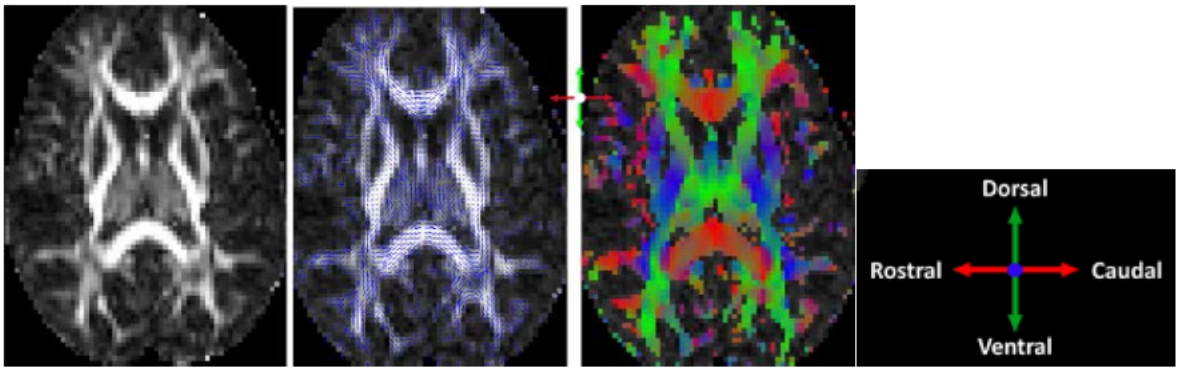

Fig.4. DTI of human brain
left: fractional anisotroy $\sqrt{(\lambda_1-\lambda_2)^2+(\lambda_2-\lambda_3)^2+(\lambda_3-\lambda_1)^2 / (\lambda_1^2+\lambda_2^2+\lambda_3^2)}$;
center: vector map; right: main diffusion direction.

In a very simplified view we can follow the arrows of the diffusion direction and obtain a selective image of the neuronal fibers connecting various brain areas (MR tractography) [17]. Since fibers may be kissing and crossing, this is a very complicated mathematical procedure. The resolution may be well in the submillimeter range. The three examples show the fiber structure of a human brain, the connection between its language centers, the Broca- and Wernicke-areas and the fiber structure in a mouse brain (fig.5).

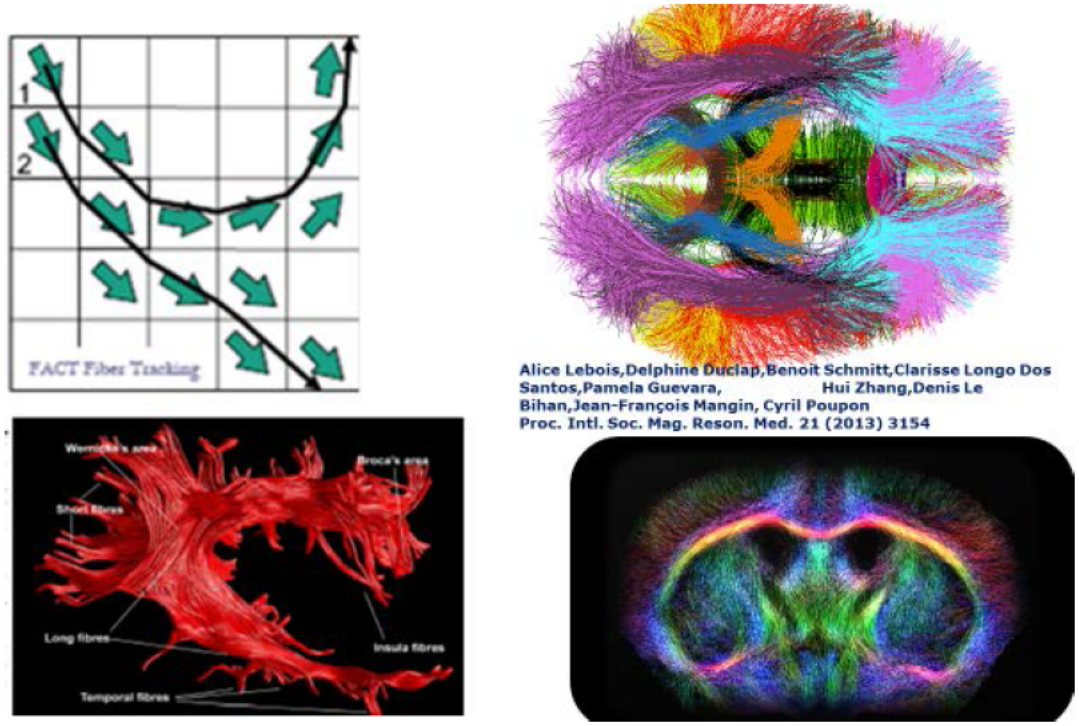

Fig.5. MR tractography clockwise: principle, fiber structure of human and mouse brain, fiber connections between language areas in human brain (Broca and Wernicke areas)

Functional MRI

MRI offers the unique possibility to map brain function without injecting a contrast agent. In activated brain areas ogygen is consumed and therefore blood diamagnetic oxyhemoglobin is converted into paramagnetic deoxyhemoglobin leading to a signal decrease. This effect is immediately overcompensated by supply of oxygenated blood leading to a final increase in oxyhemoglobin resulting in an increase of signal intensity [18,19]. In rats electric stimulation of the forepaw shows the activated areas in the motor cortex, photic stimulation allows investigation of the visual cortex. Epilepsy has been studied in a rat model by injecting pentylenetrazol (PTZ) and observing brain activation changes between the normal state, pre-seizure putative kindling and fully blown seizure (fig.6) and the effect of treatment (fig.7)

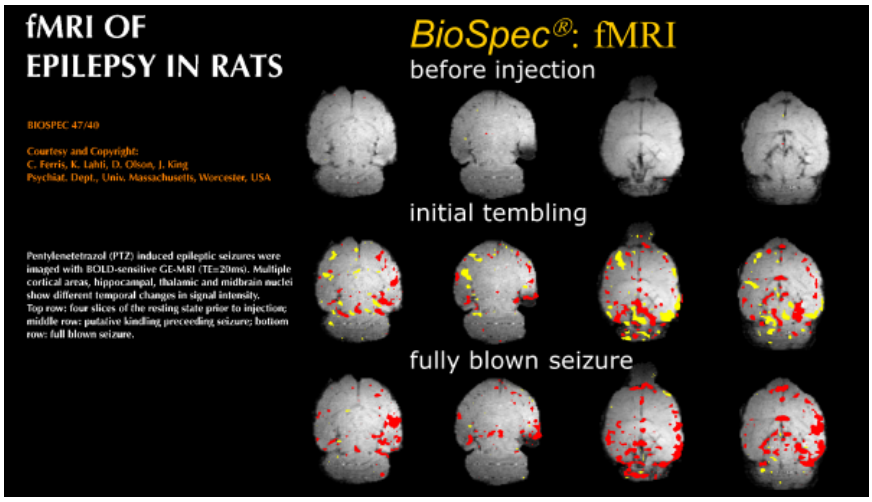

Fig.6. Steps of epileptic seizure in a rat brain initiated by injection of pentratetrazol (PTZ)

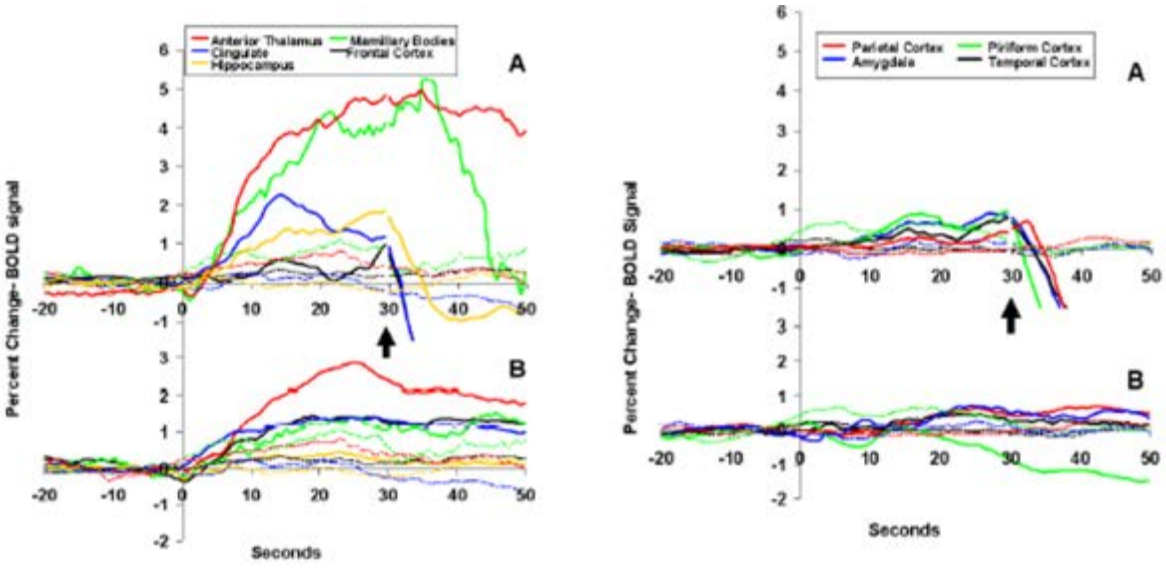

Fig.7. Epileptic seizure after injection of PTZ. Time course of activation in the affected brain areas before and after treatment with relaxing agent Ethoximid.
A: befor; B: after treatment

Resting state fMRI (rs-fMRI)

Functional MRI does not need necessarily a stimulus. If MR images are recorded extremely fast (>500 msec) time-dependent fluctuations of the signal intensity can be

observed. If these fluctuations are analyzed for frequency, phase and amplitude in all voxels, a synchrony of these variations can be observed in certain brain areas, even if these areas far apart from each other. In contrary to the *structural connectivity revealed by DTI* this connectivity is called *functional connectivity* [20-22]. There are two ways of statistical analysis. Independent Component Analysis **ICA** without any assumptions correlates the signal time course in all voxels and finds areas with high synchronity [23]. **Seed based analysis** selects one area and compares its signal time course with all other to find selectively the connectivity to the selected area [24]. Since the evaluation of the very small fluctuations of the signals needs extreme speed and sensitivity, high field MRI systems with extremely strong and fast gradients are a prerequisite. Fig.8 shows an animal experiment with a cryocoil at 9.4 Tesla. This allowed to identify many brain regions by Independent Component Analysis. The reliability and reproducibility of this method has been established by many experiments, in animal and human studies.

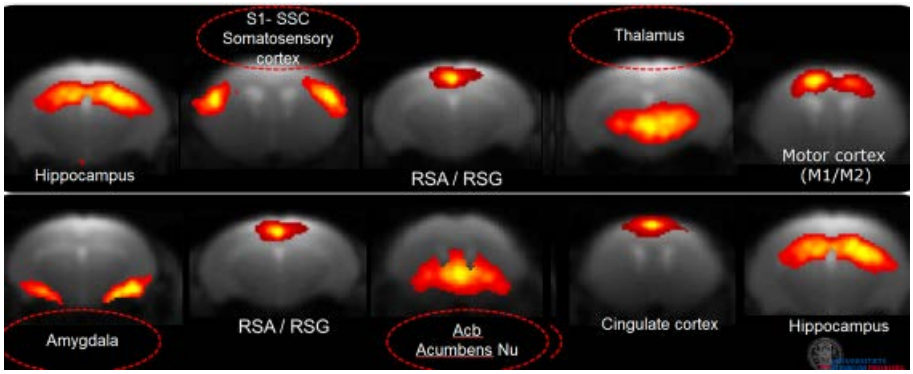

Fig.8. rs-fMRI of mouse brain. By ICA the somatosensory cortex, thalamus, motor cortex, amygdala, cingulate cortex and hippocampus are clearly identified

We can now go further and select a seed points and look for the correlation of the seed point area to other brain areas. This is here shown for the somatosensory cortex. The connectivities to many brain areas could be established.

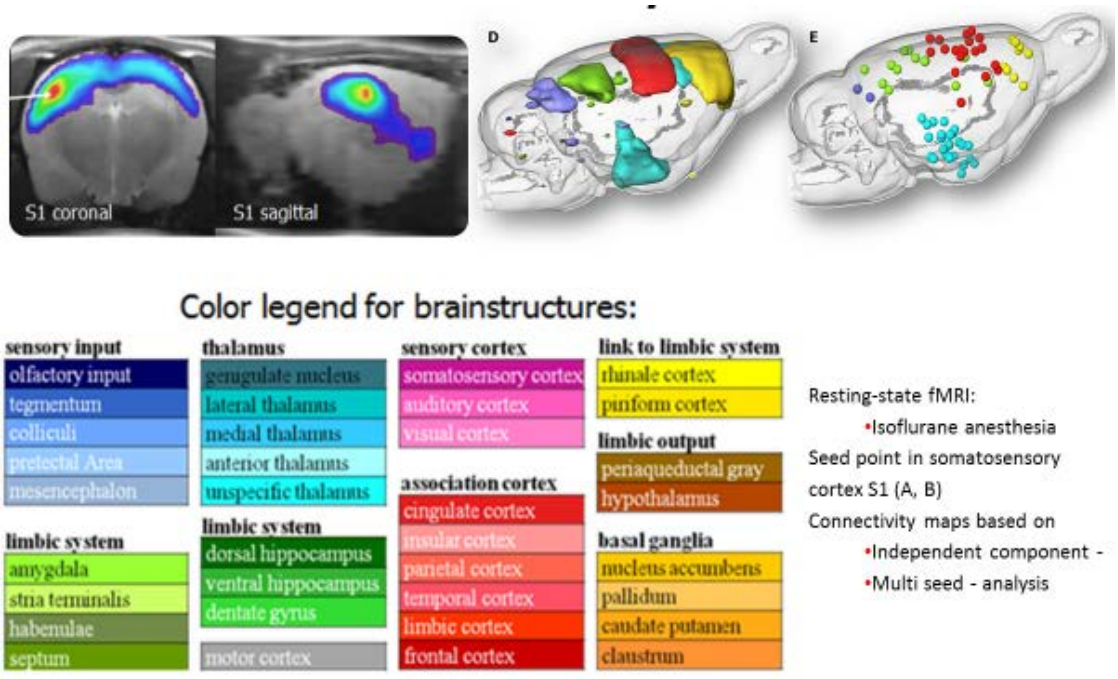

Fig.9. rs-fMRI of mouse brain. The somatosensory cortex has been chosen as seed point and its connectivities to other brain areas have been established.

Rs-fMRI in humans has established three most important brain networks (fig.10). *Central Executive Network (CEN)* is active during task performance. *Salience Network (SN)* plays a crucial role in identifying the most biologically and cognitively relevant events for adaptively guiding attention and behavior. *Default Mode Network (DMN)* is active during rest than during task-performance. It is typically deactivated during stimulus-driven cognitive processing [25,26].

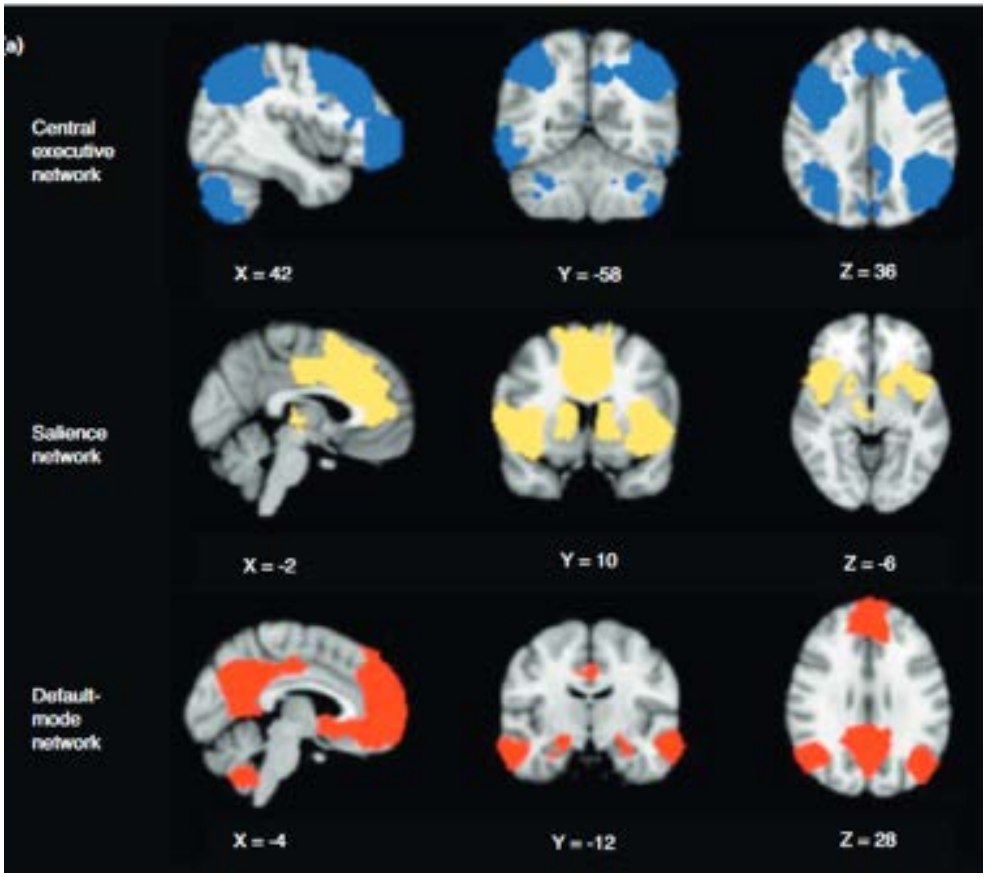

Fig.10. The three most important networks in human brain, established by ICA from rs-fMRI central executive (blue), salience (yellow) and default mode (red)

The interplay of these three networks guide reaction to external stimuli, creation of emotions and activity based on both and are therefore most important for understanding of mental diseases [27-29].

References

[1] Nobel Price Physics 1952. F. Bloch,W.W. Hansen, M. Packard, Phys.Rev. 69 (1946) 127; E.M. Purcell, H.C. Torrey, R.V. Pound, Phys.Rev. 69(1946)37

[2] Nobel Price Chemistry 1991. R.R. Ernst, Angew. Chemie Int. Engl. Ed. 31/7 (1992) 805

[3] Nobel Price Chemistry 2002. K. Wüthrich, Journal of Biomolecular NMR. **27** (1): 1–12.

[4] Nobel Price Medicine 2003. P.C. Lauterbur, Nature 242 (1973) 190; P. Mansfield, P.K. Granell J.Phys. C6 (1973) L422

[5] M. Rudin, N. Beckmann, R. Porszasz, T. Reese, D. Bochelen, A. Sauter, NMR Biomed. 12 (1999) 69;

[6] J. Hennig, A. Nauerth, H. Friedburg, Magn. Reson. Med. 3 (1986) 823

[7] A. Haase, J. Frahm, D. Matthaei, J. Magn. Reson. 67 (1986) 258

[8] A. Haase, Magn. Reson. Med. 13 (1990) 77

[9] P. Mansfield, J.Phys. C Solid State Phys. 10 (1977) 155

[10] A. Tamura, D.I. Grahem, J.Mc. Gulloch, G.M. Teasdale, J. Cer. blood flow metab. (1981) 53

[11] A. Sauter, M. Rudin, Stroke 17 (1986) 1228

[12] M.E. Moseley, M.F. Wendland, M.F. Kucharzyk, Top.Mag.Res.Imag. 3(1991)50

[13] M. Rudin, A. Sauter, Mag.Reson.Med. 23(1991)32

[14] S.A. Roussel, N. van Bruggen, M.D. King, D.G. Gadian, J.Cer.blood flow metab. 15 (1995) 578

[15] R. Damadian Science 171 (1971) 1151

[16] E.A.H. von dem Hagen, R.M. Henkelman, Mag.Reson.Med. 48 (2002) 454

[17] S. Mori, W.E. Kaufmann, C. Davatzikos, B. Stieltjes, L. Amodei, K. Frederikson, G.D. Pearlson, E.R. Melhem, M. Solaiyappan, G.V. Raymond, H.W. Moser, P.C.M. van Zijl, Mag.Reson.Med 47 (2002) 215

[18] S. Ogawa, T.M. Lee, A.S. Nayak, P. Glynn, Magn. Reson. Med. 14 (1990) 68

[19] Ch. Preibisch, A. Haase J. Mag. Reson. 140 (1999) 162

[20] B.B. Biswal, [Review]. Neuroimage, 62(2), p.938 (2012)

[21] B.B. Biswal, Biological Psychiatry, 69(9), 200 (2011)

[22] M.I. Posner, M.E. Raichle, Images of Mind (1994), Scientific American Library, New York

[23] C.F. Beckmann, M. de Luca, J.T. Devlin, S.M. Smith, Philosophical Transactions of the Royal Society, B-Biological Sciences, 360 (1457), (2005)

[24] D.S. Margulis, A.M.C. Kelly, L.Q. Uddin, B.B. Biswal, F.X. Castellanos, M.P. Milham, Neuroimage, 37(2), 579-588 (2007)

[25] M.D. Fox, A.Z. Snyder, J.L. Vincent, M. Corbetta, D.C. Van Essen, M.E. Raichle, Proceeding of National Academy of Sciences of the United States of America, 102(27), 9673 (2005)

[26] R.L. Buckner, Neuroimage, 62(2), 1137-1145 (2012)

[27] V. Mennon, L.Q. Uddin, Brain Struct.Function DOI 10.1007/s00429-010-0262-0 (2010)

[28] Lena Palanipyappan, P.F. Little, J. Psychiatry Neurosci.1: 17-27 (2012)

[29] V. Mennon, Trends in cognitive Sciences (2011) 1-14

Study of the spatial structure of fluvastatin and its complex with dodecylphosphocholine micelles by NMR spectroscopy

G.S. Musabirova, L.F. Galiullina, A.V. Aganov, V.V. Klochkov

Kazan (Volga region) Federal University, 420008, 18 Kremlevskaya st., Kazan, RF

e-mail: musabirova.guzel@bk.ru

Introduction

Hydroxy-methyl-glutaryl-coenzyme A (HMG-CoA) reductase inhibitors or statins, including fluvastatin, reduce the amount of low-density lipoprotein (LDL) cholesterol, which is known as a well-established risk factor for atherosclerosis [1,2]. The structure of fluvastatin is presented in the fig.1. There is a hypothesis that pharmacological features of statins depend on their location in cell membrane [3]. NMR NOESY spectroscopy is a powerful tool for studying conformational structure of molecules and intermolecular complexes, but its application to investigation of interactions of compounds with cell membranes is complicated because relaxation times for phospholipid aggregates are too large relative to the NMR time-scale [4-5]. For these reasons, in this study, we examined statin interaction with model membranes – dodecylphosphocholine micelles.[6] The aim of this work was to study the interaction between fluvastatin and dodecylphosphocholine (DPC) micelles, which were used as model of biological membranes.

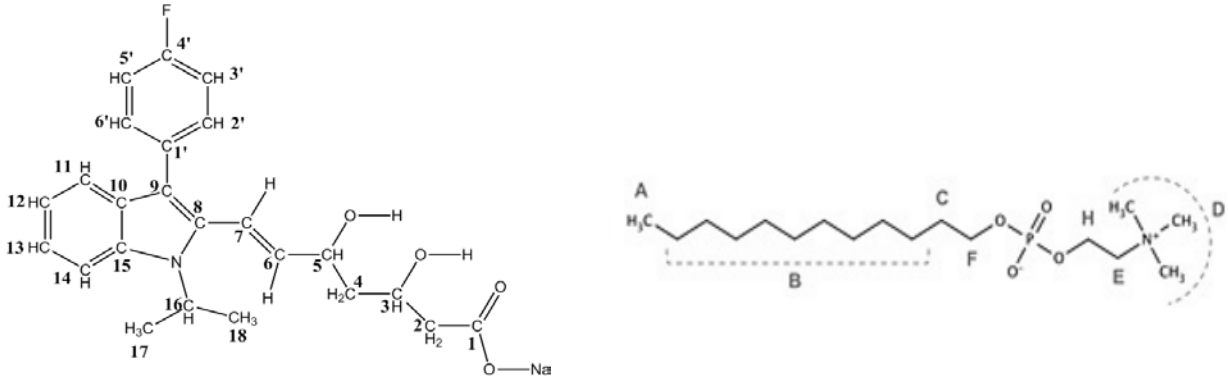

Fig.1. Chemical structures of fluvastatin (left) and dodecylphosphocholine (right).

Material and Methods

Fluvastatin was dissolved in D_2O and D_2O+DPC with concentration of 3 g/l. Solution containing micelles was prepared using combination of deuterated (>98%) and undeuterated DPC. The concentration of DPC in D_2O solution was greater than the critical micelle concentration and was equal to 3 g/l for non-deuterated DPC and 7.5 g/l for deuterated DPC.

All NMR experiments were performed on a Bruker Avance II 500 NMR spectrometer equipped by a 5 mm probe using standard Bruker TOPSPIN software. Temperature control was performed using a Bruker variable temperature unit (BVT-3000) in combination with a Bruker cooling unit (BCU-05). Experiments were performed at 303 K without sample spinning. Chemical shifts are given in values of ppm, referenced to residual solvent signals (4.72 ppm for ^{1}H in D_2O). ^{1}H NMR data were collected with 32k complex data points. All two-dimensional experiments were performed with 2k × 512 data points; the number of transients (96 scans) and the sweep widths were optimized individually. 2D ge-NOESY experiments were performed with the pulsed filtered gradient technique, the relaxation delay

was set to 2 s, and the 90° pulse length was 7.5 μs. Mixing time values were 0.5, 0.4, 0.3, 0.2, and 0.1 s.

Results and Discussion

^{1}H NMR spectrum of fluvastatin is shown in the fig.2. Signals in the spectra were assigned according to the ^{1}H spectrum and the results of 2D ^{1}H-^{1}H COSY, ^{1}H-^{13}C HSQC and ^{1}H-^{13}C HMBC NMR experiments. It was found thatNMR signals of fluvastatin are different in pure D_2O solution and in D_2O + DPC micelles solution. All proton signals of aromatic region (CH-11,12,13,14; CH-2',3',5',6') and CH-7 signal in the ^{1}H NMR spectrum of fluvastatin+DPC micelles exhibit strong high-field shifts as compared to the spectrum in pure D_2O. Observed differences in the spectra indicate that probably fluvastatin forms molecular complex with DPC micelle and mostly its cyclic parts are involved in the interaction.

In order to define conformational structure of fluvastatin 2D NOESY experiment was carried out. There are no non-trivial cross peaks were observed in the spectrum. Thus, it can be concluded that fluvastatin has "linear" form in solution without special «folded» structure.

To investigate how fluvastatin interacts with model membranes additional 2D NOESY spectra with different mixing times of fluvastatin+DPC micelles water solution were obtained. There are set of intermolecular cross peaks observed in the spectrum: between **B** signal of the micelle (fig.1) and 14, 11, 6'(2'), 16, 5'(3'), 12 protons of fluvastatin; C signal of the micelle and 14, 11, 6'(2'), 13 protons of fluvastatin; **D** signal of the micelle and 6'(2'), 5'(3'), 17, 18; groups **E**, **F**, **H** of DPC and 6'(2'), 5'(3'). Observed intermolecular NOEs indicate that fluvastatin penetrates into the surface of model membrane by its aromatic part. In conclusion based on the obtained 2D NOESY spectra average distances between DPC micelles and fluvastatin nuclei were calculated. Schematic presentation of observed intermolecular NOEs and distances are presented in the fig.3.

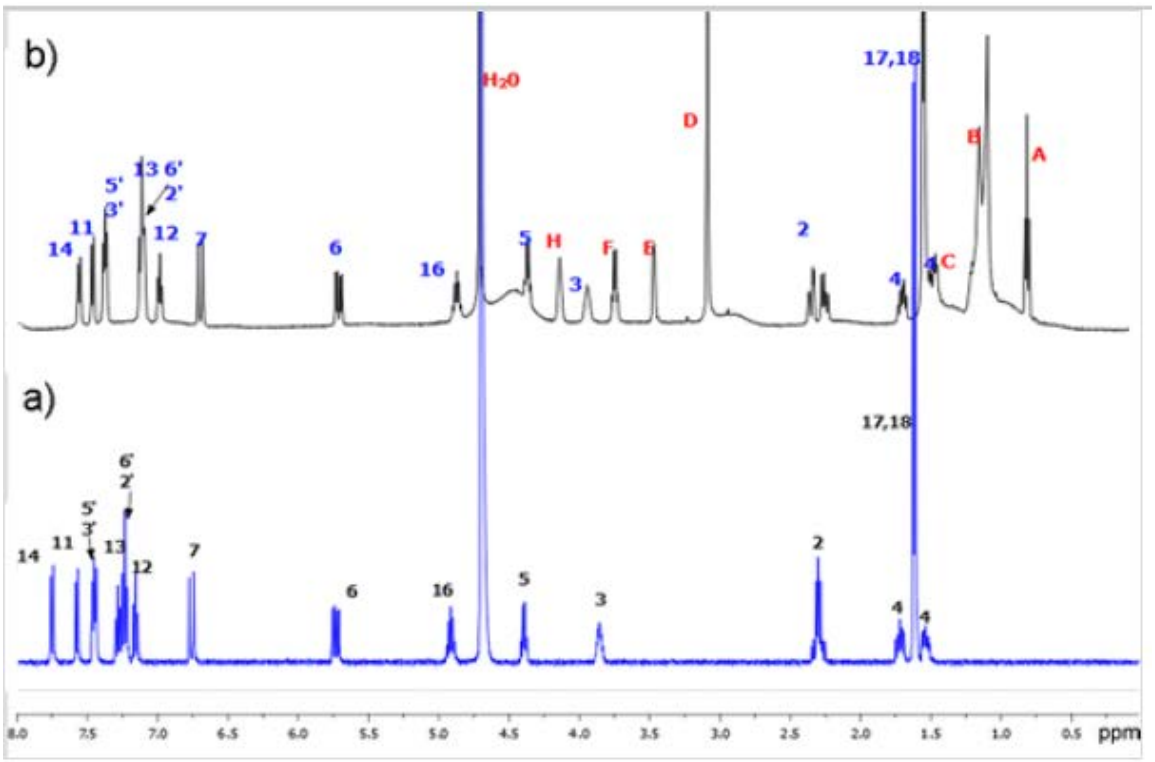

Fig.2. ^{1}H NMR spectra of (a) fluvastatin and (b) fluvastatin+DPC micelles in D_2O solution, T=303K. Figures correspond to the numeration of statin atoms. Latin letters correspond to DPC atoms (see fig.1).

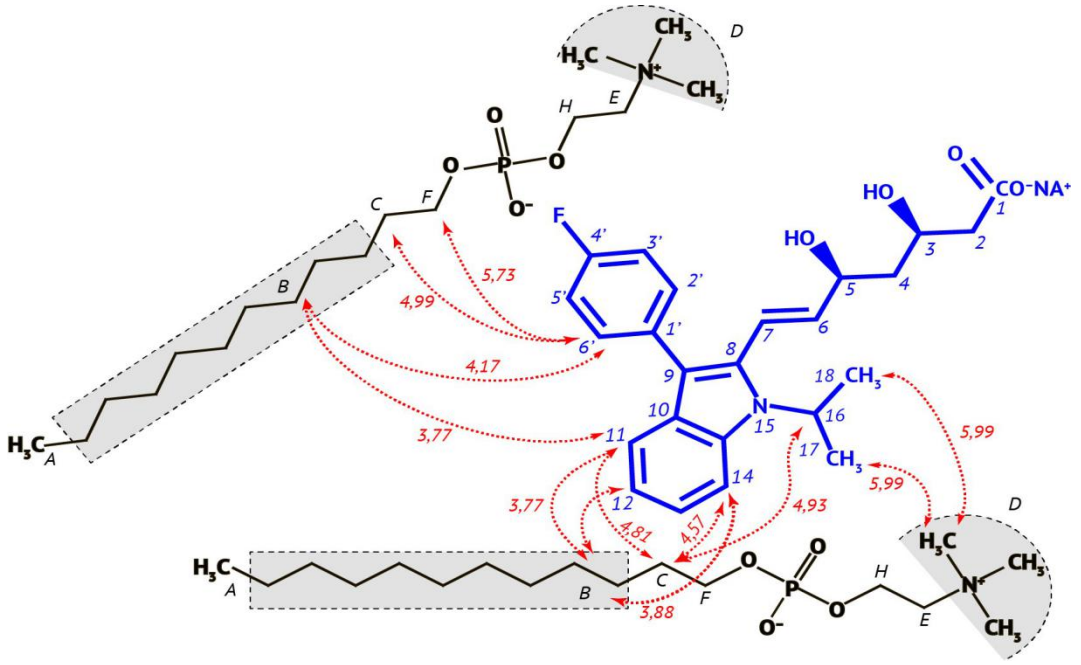

Fig.3. Schematic presentation of observed intermolecular NOEs and calculated average distances between DPC micelles and fluvastatin nuclei. Distances are given in Å.

Conclusion

Conformational features of fluvastatin in water solution were determined. 2D NOESY NMR spectra of fluvastatin+DPC micelles in D_2O solution showed that fluvastatin form molecular complex with model membrane. It intercalates into model membrane surface by its aromatic part. Intermolecular distances between DPC micelles and fluvastatin nuclei were calculated.

References

[1] Davidson H. (1994) Fluvastatin long term extension trial (FLUENT): Summary of efficacy and safety. Am J Med. 96(6): S41-4

[2] Peters TK, Jewitt-Harris J, Mehra M, Muratti EN. (1993) Safety and tolerability of fluvastatin with concomitant use of antihypertensive agents: An analysis of a clinical trial database. Am J Hypertens 6: S346-52

[3] Mason, R.P. Intermolecular differences of 3-hydroxy-3-methylglutaryl coenzyme a reductase inhibitors contribute to distinct pharmacologic and pleiotropic actions [Text] / R.P. Mason, M.F. Walter, Ch.A. Day, R.F. Jacob // the American journal of cardiology – 2005. – V. 96. – P. 11-23.

[4] Rakhmatullin IZ, Galiullina LF, Klochkova EA, Latfullin IA, Aganov AV, Klochkov VV. (2016) Structural studies of pravastatin and simvastatin and their complexes with SDS micelles by NMR spectroscopy. J Mol Struc 1105: 25-9

[5] Galiullina LF, Rakhmatullin IZ, Klochkova EA, Aganov AV, Klochkov VV. (2015) Structure of pravastatin and its complex with sodium dodecyl sulfate micelles studied by NMR spectroscopy. Magn Reson Chem 53(2): 110-4

[6] Kallik DA, Tessmer MR, Watts ChR, Li Ch-Y. (1995) The use of dodecylphosphocholine micelles in solution NMR. J Magn Reson B

Influence of the non-stoichiometry on the frustrated honeycomb layered lithium nickeloantimonate

T. Salikhov[1], E. Klysheva[1], M. Iakovleva[1], E. Zvereva[2], I. Shukaev[3], V. Nalbandyan[3], B. Medvedev[3], E. Vavilova[1]

[1]Zavoisky Physical-Technical Institute, 420029, Kazan, Russia

[2]Faculty of Physics, Moscow State University, 119991, Moscow, Russia

[3]Chemistry Faculty, Southern Federal University, 344090, Rostov-on-Don, Russia

e-mail: tmsalikhov@gmail.com

In recent decades the layered oxides of alkali and transition metals are intensively investigated due to their potential applications as solid electrolytes and electrode materials in modern ionics. Recently, a new generation of layered complex metal oxides with honeycomb-based crystal structure where ordered mixed-layers of magnetic cations alternate with non-magnetic alkali metal layers has been a subject of intense research worldwide. In this work we present the results of the investigation of new quasi two-dimensional (2D) honeycomb-lattice compound $Li_3Ni_2SbO_6$ and non-stoichiometric $Li_{0,8}Ni_{0,6}Sb_{0,4}O_2$.

The magnetization data reveal the change of the sign of magnetic interactions and suppressing of the magnetic correlations at low temperatures with doping. We assume the crossover to the cluster spin glass state in $Li_{0,8}Ni_{0,6}Sb_{0,4}O_2$ instead of the antiferromagnetic transition in $Li_3Ni_2SbO_6$. Basic magnetic properties of $Li_3Ni_2SbO_6$ have been reported recently [1,2].

^{7}Li (I = 3/2) NMR experiments were performed and we found that the behavior of the NMR spectrum and relaxation at low temperature is caused by the interaction with the magnetic Ni^{2+} ions and reflects the dynamics of magnetic subsystem. Also from NMR data we conclude that the vacancies in the lithium subsystem rise the lithium mobility at high temperatures.

The work was supported by Foundation for Basic Research (grant 14-02-01194 and 14-02-00245)

References

[1] E.A. Zvereva, *et al*., *Dalton Trans.* **41**, 572 (2012).

[2] V.V. Politaev, *et al*., *J. Solid State Chem.* **183**, 684 (2010).

Two dimensional nuclear magnetic resonance spectroscopy in research of structure and dynamics of human insulin

O.G. Miheeva, S.V. Efimov, V.V. Klochkov

Kazan Federal University, 420008, Kremlevskaya str. 18, Kazan, Russia

e-mail: oksanalina693@mail.ru

Introduction

Today there is a growing interest in the problem of structural and dynamical properties of insulin. Peptide hormone insulin is produced in the pancreatic β-cells. It has a huge impact on the metabolism in almost all tissues. The main effect is to reduce the glucose concentration in blood. Insulin increases the permeability of the plasma membrane for glucose by interacting with insulin receptors, stimulates the production glycogen from glucose in liver and muscles, and enhances the synthesis of fats and proteins. Insulin molecule is composed of two polypeptide chains containing 51 amino acid residues: A-chain consists of 21 residues, and B-chain contains 30 amino acid residues. The polypeptide chains are joined by two disulphide bonds through cysteine residues, the third disulphide bond is located in the A-chain [1].

The aim is to study the structure and dynamics of the chain of human insulin using NMR spectroscopy. The insulin molecule in solution has a sufficiently flexible structure that is prone to aggregation, which makes it difficult to study in some cases. The behaviour of the molecule depends on the medium pH, temperature, presence of ions in the solution, and other factors. Study of the structure and dynamics of molecules in solution or in the form of various complexes is valuable for practical aspects in pharmaceutics and for understanding the fundamental laws of structure–function correlations in bioactive molecules.

Experimental

^{15}N-labeled Insulin (85% purity) was purchased from FarmKholding (St. Petersburg). MilliQ class water was used to prepare the solution, 2.9 mg insulin was taken. 10% D_2O was added, total volume of the sample was 600 μL; 0.02 wt % of NaN_3 was added as a preservative. HCl was used to lower the pH and facilitate insulin solubility. To prevent aggregation, the solution was continuously stirred. Bruker Avance III HD spectrometer was used for recording HSQC, TOCSY, NOESY spectra and for measuring T_1 and T_2 relaxation times; operating frequency is 70 MHz in the proton channel. Spectra were obtained at 293 K, pH level was 2.59.

Results and Discussion

To measure the cross-relaxation rate and calculate the interatomic distances 2D NOESY spectra with different mixing times (τ_m = 70 and 100 ms) were recorded.

A part of the NOESY NMR spectrum of insulin is shown in fig.1. Relative intensities of the cross-peaks were defined as $I = \frac{1}{2}\left(I_{ab}/I_{bb} + I_{ba}/I_{aa}\right)$. Integration was performed in Sparky programme by fitting the peaks by the Gaussian shape; this allowed distinguishing partially overlapping signals.

Consider the data obtained NMR spectrum in more detail. The experiment with the mixing time of 100 ms was taken to analysis, the cross-relaxation rate can be estimated as

$\delta = I/\tau_m \equiv 0.6\ \mathrm{s}^{-1}$. Next, we calculate the correlation time as [2]

$$\tau_c = \frac{10\delta r_{AX}^6}{\gamma^4\hbar^2(\mu_0/4\pi)^2} \approx 2.11\cdot10^{-9}\,(\mathrm{s}) \qquad (1)$$

Thus, we can estimate the effective volume of the molecules $V = \tau_c k_b T/\eta \approx 8.5\cdot10^{-27}\,\mathrm{m}^3$ (assumed that the molecule has a spherical shape) and to determine the hydrodynamic radius of the molecule as [7]

$$R = \sqrt[3]{\frac{3V}{4\pi}} \approx 1.3\cdot10^{-9}\,(\mathrm{m}) \qquad (2)$$

This value agrees with known models of insulin and gives an evidence that human insulin exists in the acidic solution at pH = 2.6 presumably as monomers.

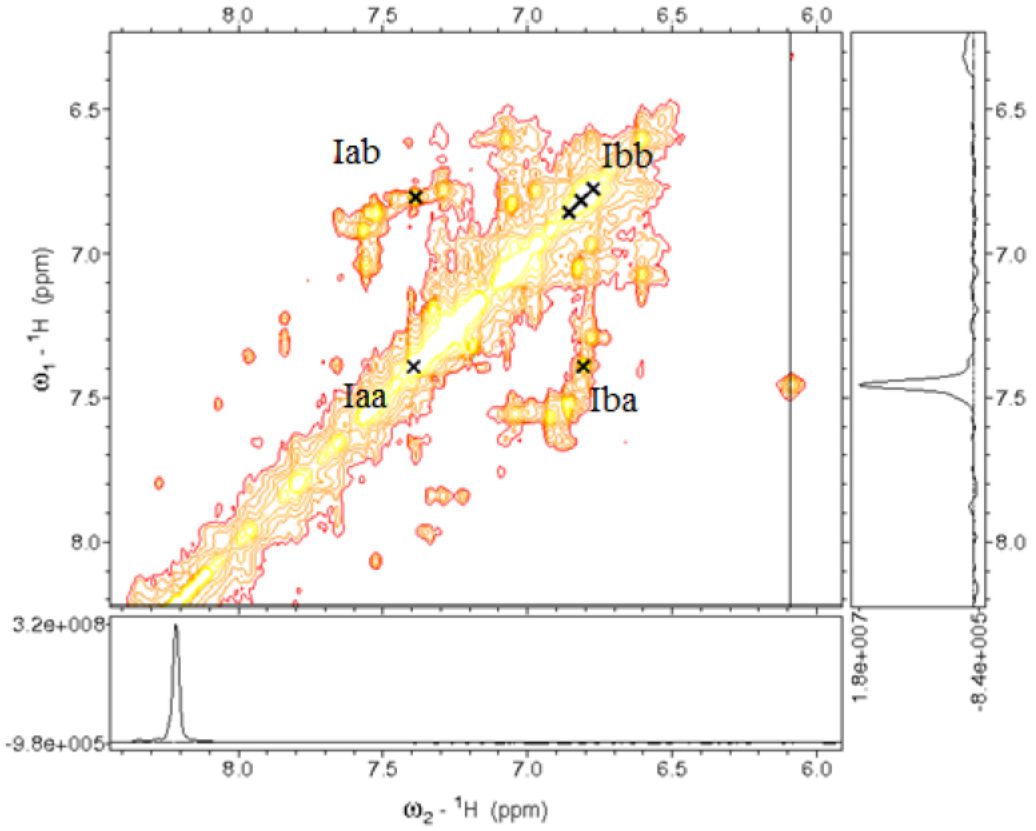

Fig.1. NOESY NMR spectra of insulin recorded at 20°C (aromatic signals)

Fig.2 shows the distribution diagram of the ^{15}N relaxation times. Obtained values fall within the range $0.368 \le T_1 \le 1.398$ s. The relaxation times for 22% of all observed signals are longer that most of the others (>0.8 s), which indicates that these residues form the most rigid elements of protein structure. In further investigation we will compare the T_1 and T_2 values and determine the assignment of the signals to their amino acid residues, which will give us more detailed information on the rigidity of different segments of the protein.

Thus, it possible to obtain unique information on the structure of molecules in solution through nuclear Overhauser effect spectroscopy. This is very important since information of this kind is difficult to obtain in other ways. Knowledge of the aggregation state of a protein in solution (whether it forms oligomers or not) is of interest to pharmaceutical applications.

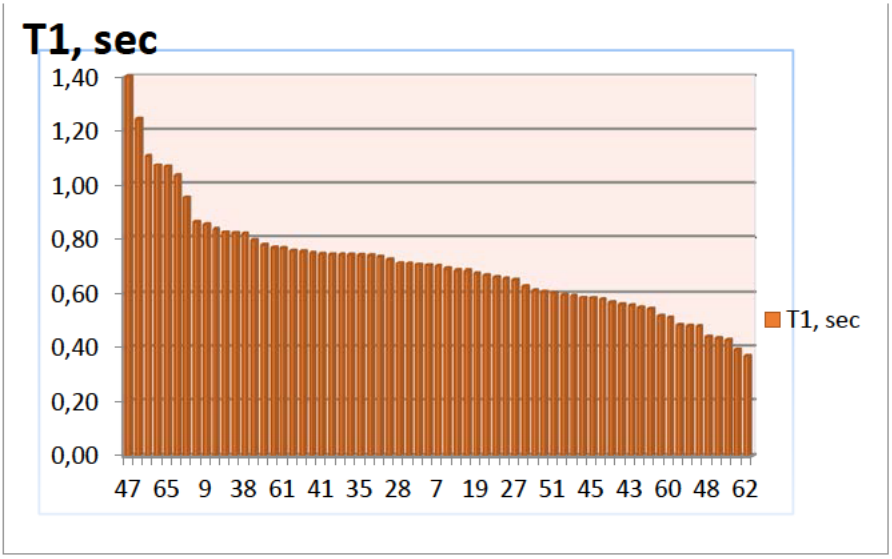

Fig.2. Distriburion ^{15}N relaxation times T_1 (in descending order). Horizontal axis shows arbitrary numbers of the signals

References

[1] Olsen, H.B. Investigations of structure and dynamics of insulin mutants using NMR spectroscopy [Text] / B. Olsen, H.B. // Roskilde University, Novo Nordisk A/S & ATV. - 1996 . – P. 80.

[2] Richard R. Ernst, Bodenhausen G. Principles of Nuclear Magnetic Resonance in One and Two Dimensions [Text] / Richard R. Ernst. // Clarendon Press, Oxford . – P. 608.

[3] Peana, M. Manganese and cobalt binding in a multi-histidinic fragment [Text] / M. Peana, S. Medici, V. Nurch // The Royal Society of Chemistry . - 2013 . – P. 9.

[4] Истрате, А.Н. Структурный полиморфизм металлсвязывающего домена природных вариантов бета-амилоида в растворе как фактор агрегации при развитии болезни Альцгеймера [Текст] / А.Н. Истарте // Диссертация на соискание ученой степени кандидата химических наук. – Москва: Институт молекулярной биологии им. В. А. Энгельгардта Российской академии наук, 2016 . – 124 с.

[5] Kukol, A. Molecular modeling of proteins [Text] / A. Kukol, J. Walker // University of Hertfordshire, Hatfield, Hertfordshire, UK . – 2015 . – P. 474.

[6] Lacapere, J.J. Membrane protein structure determination [Text] / J.J. Kukol, J. Walker // University of Hertfordshire, Hatfield, Hertfordshire, UK . – 2010 . – 453.

[7] Leach, A.R. Molecular modelling principles and applications [Text] /A. Leach, A.R. // Edinburgh Gate Harlow, England . -2001 . – P. 396.

Analysis of manifestations of spin exchange and dipole-dipole interactions in EPR spectra of nitroxyl radical solutions

M.M. Bakirov

Zavoisky Physical-Technical Institute, Kazan 420029, Russian Federation

e-mail: pinas1@yandex.ru

The high sensitivity of the shape of the EPR spectra of stable nitroxide radicals to their chemical structure, the presence of paramagnetic additives, solvent polarity makes method of EPR oxymetry an effective tool [1-3]. EPR of radicals is a perspective technique for direct measurement of tissue pO_2, which has several advantages over the other existing methods for applications in which the parameter of interest is the pO_2 of tissues.

The shape of the EPR spectra of the spin probes depends on the spin decoherence and spin coherence transfer between probes induced by the spin exchange and dipole-dipole interactions. The description of the EPR of nitroxide radicals often use simplified algorithms that do not take into account all the processes due to exchange and dipole-dipole interactions. In papers [4,5] different algorithms of separating dipole-dipole and Heisenberg spin exchange interactions are proposed. In our work [6] the theory was extended to include into consideration all magnetic nuclei of the spin probes. The exact theoretical expressions which describe the EPR spectrum of spin probes with exchange, dipole-dipole, and hyperfine interactions were derived [6].

Dipole-dipole and exchange interaction contributions for EPR lineshape depends on the viscosity of solution. In this work we applied the developed method for situation of nitroxide radical solution with different temperature/viscosity ratio (T/η). For this purpose we made numerical calculations of spin exchange rates and dipole-dipole rates for nitroxyl radical in 60% water glycerol solution (fig.1).

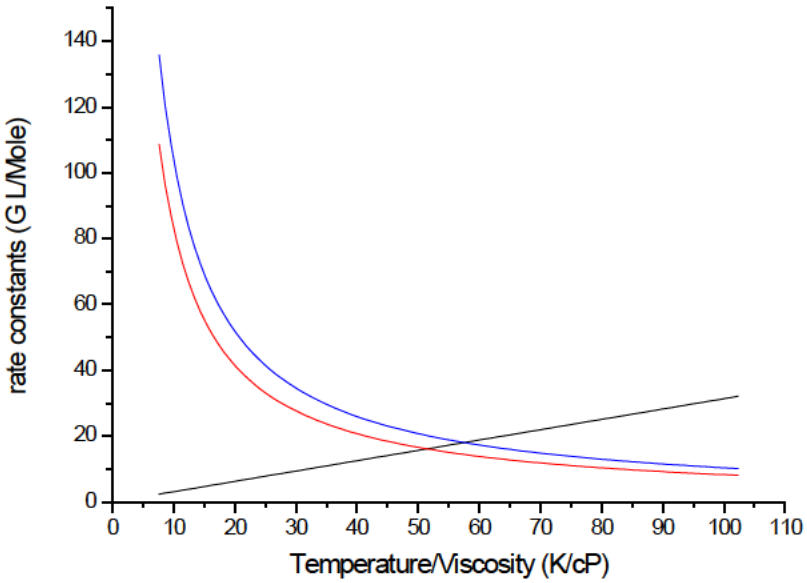

Fig.1. Dependences of K_{ex}, G L/mM (black line), V_0, G L/mM (red line), W_0, G L/mM (blue line) on the two spin probes mutual diffusion coefficient. Parameters used in these simulations: A_N = 16 G, r_0 = 0.7 nm, and x_0 = 3400 G

For several sets of A_N, σ, $1/T_2$, exchange constant (K_{ex}), constant of dipole spin coherence transfer (V_0) and constant of dipole spin dephasing (W_0) computer experiments with the model ^{15}N nitroxide radical were performed. Analysis of these computer experiments

were compared with input parameters. This routine was done the same way like in [6]. Results for some cases are shown in fig.2: Input spin coherence transfer parameter $K_{sct}\,C$ was set on x-axis and value of $K_{sct}\,C$ that we got from EPR lineshape analysis is postponed on y-axis. Parameters used in these simulations are: $\Gamma_k = 0.2$ G, $A_N = 16$ G, $g = 2$, number of protons = 12, $A_P = 0.2$ G, $K_{ex} = 3$ G L/M, $V_0 = 86.5$ G L/M, $W_0 = 108$ G L/M (open orange square); $K_{ex} = 10.5$ G L/M, $V_0 = 24.8$ G L/M, $W_0 = 31$ G L/M (open red circles); $K_{ex} = 32$ G L/M, $V_0 = 8.1$ G L/M, $W_0 = 10.1$ G L/M (open blue circles).

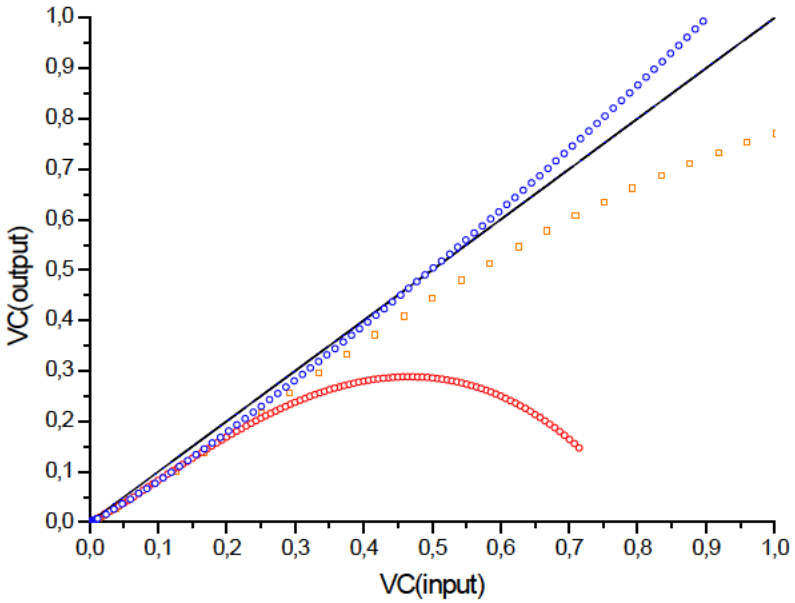

Fig.2. Correlation between the input and output spin coherence transfer rate $V = K_{sct}\,C$ used as the input of the computer simulation of the EPR spectrum and the value of the kinetic parameter $K_{sct}\,C$ obtained by analyzing the dispersion contribution to the simulated EPR spectrum component. The bisector is shown as the solid line.

Our routine was applied for calculated spectra and for EPR spectra of Tempol N15 in 60% water glycerol solution at different temperatures.

I am gratrfull to Dr. R.T. Galeev for numerous discussion.

References

[1] N. Khan, B.B. Williams, Swartz. “Clinical applications of in vivo EPR: Rationale and initial results.” Appl Magn Reson. **30**, 185-199 (2006)

[2] F. Villamena, J. Zweier. “Detection of reactive oxygen and nitrogen species by EPR spin trapping” Antioxidants and redox signaling. **6**, 619-629 (2004)

[3] L. Weiner. “Stable nitroxyl radicals as pH, thiol and electron transfer probes” Appl. Magn. Reson. 31, 357-37 (2007)

[4] K.M. Salikhov. “Contributions of Exchange and Dipole-Dipole Interactions to the Shape of EPR Spectra of Free Radicals in Diluted Solutions.” Appl.Magn.Reson. 38, 237-256 (2010)

[5] M. Peric, B Bales, M. Peric. “Electron Paramagnetic Resonance Line Shifts and Line Shape Changes Due to Heisenberg Spin Exchange and Dipole-Dipole Interactions of Nitroxide Free Radicals in Liquids 8. Further Experimental and Theoretical Efforts to Separate the Effects of the Two Interactions”, J. Phys. Chem. A, 116, 2855-2866 (2012)

[6] K.M. Salikhov, M.M. Bakirov, R.T. Galeev. ”Detailed Analysis of Manifestations of the Spin Coherence Transfer in EPR Spectra of ^{14}N Nitroxide Free Radicals in Non-viscous Liquids”, Appl Magn Reson, 47, 1095-1122 (2016)

Investigations of Y_2SiO_5:Nd^{143} by ESR method

R. Likerov[1], R. Eremina[1,2], T. Gavrilova[1,2], I. Yatsyk[1,2], I. Fazlizhanov[1,2], V. Shustov[2], Yu. Zavartsev[3], A. Zagumennyi[3], S. Kutovoi[3]

[1] Kazan (Volga Region) Federal University, Kremlevskaya st., 18, Kazan, 420008 Russia.
[2] Kazan E. K. Zavoisky Physical-Technical Institute of the RAS, Kazan, 420029, Russia.
[3] Prokhorov General Physics Institute of the RAS, Moscow, 119991 Russia.

e-mail: rodionlikerov@gmail.com

Yttrium silicate monocrystals (Y_2SiO_5) are known as the basis for perspective materials, especially then they are doped with rare-earth ions, for example with neodymium-143. These crystals, Y_2SiO_5:$^{143}Nd^{3+}$, have useful properties such as large optical density, which is important for making an efficient optical quantum memory, and large phase-relaxation times, which means that long-lived hyperfine states are possible to be obtained in these crystals [1].

To study the physical properties of Y_2SiO_5:$^{143}Nd^{3+}$ monocrystals X-ray and electron spin resonance (ESR) methods was used. The X-ray diffraction pattern of the sample was obtained using a DRON-7 diffractometer equipped with the CuK_α radiation source. The system was calibrated using annealed nickel foil. The diffractometer parameters were 40 kV, 20 mA, *a* 2μ scan range of 10° to 110°, step size of 0.02° and a scan speed of 5 s/step.

Electron spin resonance (ESR) measurements were carried out on a Bruker EMX/plus spectrometer equipped with continuous-flow He cryostats (Oxford Instruments) at X-band (9.4 GHz) frequency in the temperature range 5 to 40 K.

Experimental samples of Y_2SiO_5:$^{143}Nd^{3+}$ monocrystals were oriented by X-ray diffraction and cutted in the (*ab*), (*ac*), and (*bc*) crystallographic planes to form rectangular parallelepipeds measuring 1.5 × 2 × 3 mm. Y_2SiO_5:$^{143}Nd^{3+}$ monocrystals were synthesized at Prokhorov General Physics Institute of the Russian Academy of Sciences (GPI RAS) (Moscow, Russia). All crystals have been grown in iridium crucibles with a diameter of 40 mm by the Czochralski method at industrial installations with induction heating "Crystal-2" and "Crystal-3M".

First of all, the X-ray analysis of Y_2SiO_5 monocrystal showed that this crystal is in a single state, and its structure belongs to the space group $C_{2/c}$. Lattice parameters have these values: a = 10.410 Å, b = 6.721 Å, c = 12.490 Å, α = 90°, β = 102.65°, γ = 90°. These parameters are consistent with another one, which are given in literature reference [2]. Yttrium ions in the unit cell are located in two positions in Y (1) and Y (2) substituted by Nd^{3+} (see fig.1a and fig.1b).

The observed ESR spectrum Nd^{3+} in Y_2SiO_5 contains two groups of eight nonequidistant lines, which represent the hyperfine structure (HFS) components because of odd neodymium isotope ^{143}Nd pretend to take two structurally nonequivalent positions and the line from the even isotope is absent. The positions of observed ESR lines doesn't demonstrate the temperature dependence in the temperature range 5 K < T < 20 K. Fig.2

presents an angular dependency of HFS lines recorded in (*a***c*) and (*ab*)-planes, respectively. To fit the experimental data, effective spin Hamiltonian with the effective electron spin S = 1/2 and the nuclear spin $I = 7/2$ was calculated.

Hamiltonian structure:

$$H = S * \mathbf{A} * I + g * \mu_\beta * B * S \qquad (1)$$

Here, **A** is the tensor of HFS, g - g-tensor, B – magnetic field, μ_β - Bohr magneton.

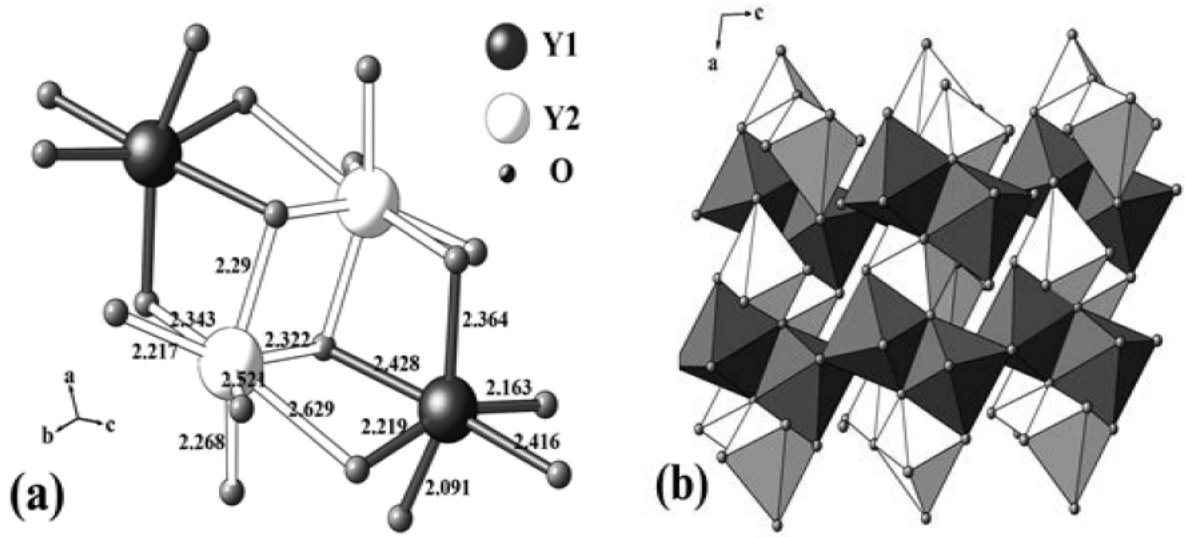

Fig.1. Crystal structure of Y2SiO5 (space group $C_{2/c}$): (a) two structurally nonequivalent positions of Y ions, which substituted by Nd^{3+} ions; distances are given in Å; (b) pairs of distorted octahedrons YO6 in (*ac*)-plane; nonequivalent octahedrons are shown by white and black colors, respectively to (a);

As seen from fig.2 the experimental resonance fields fit well to the calculated curves. The obtained values of the g and A (in K) tensors in crystallographic coordinate system are given in Tab.1. g-values, which were obtained from experiment are close to the values from [3].

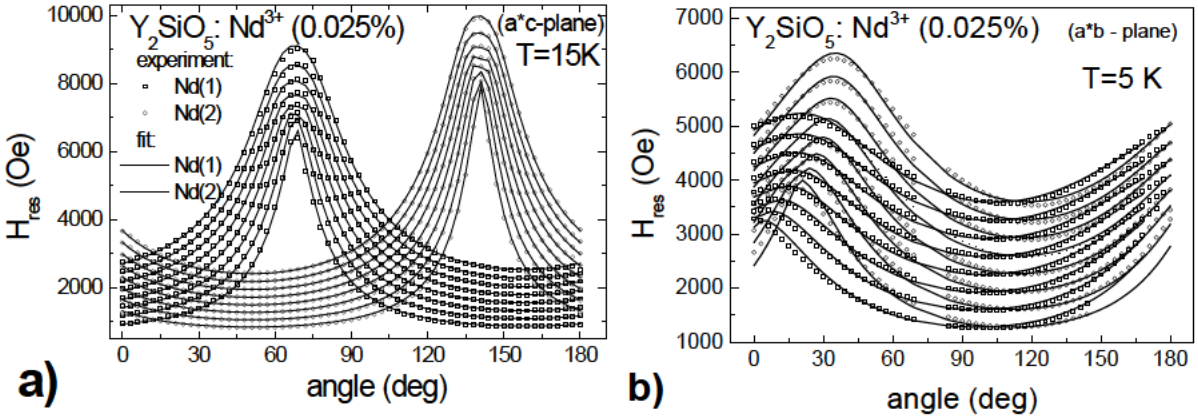

Fig.2. Angular dependencies of ESR lines in Y_2SiO_5:$^{143}Nd^{3+}$ (0.025%): (a) (*a***c*) — plane at $T = 15$ K; (b) (*ab*) — plane at $T = 5$ K.

Table 1. Microscopic parameters of the *g* and *A* (in K) tensors in crystallographic coordinate system for the first and second paramagnetic centers of Nd^{3+} ions doped in Y_2SiO_5.

	g			*A*		
Nd (1)	3.927	0.401	0.044	0.0632	0	0
	0.401	2.248	0.004	0	0.0273	0
	0.044	0.004	0.822	0	0	0.0168
Nd (2)	4.063	0.541	0.187	0.0635	–0.0095	0
	0.541	1.967	–0.016	–0.095	0.0245	0
	0.187	–0.016	0.7316	0	0	0.0119

Knowledge of these parameters allows to proceed the investigation of monocrystallic Y_2SiO_5:$^{143}Nd^{3+}$ as the material for modern quantum memory operating devices.

This work was supported by the Russian Science Foundation [grant number 16-12-00041].

References

[1] C.W, Thiel, et. al., Rare-earth-doped LiNbO3 and KTiOPO4 (KTP) for waveguide quantum memories, J. Phys. B: At. Mol. Opt. Phys. 45 (2013) 124013 1-14.

[2] W. Zhou, et.al., Study on the effects of 5d energy locations of Ce3+ ions on NIR quantum cutting process in Y2SiO5: Ce3+, Yb3+, Optics express 20 (2012) A510-A518.

[3] G. Wolfowicz, et. al., Coherent storage of microwave excitations in rare-earth nuclear spins, Phys. Rev. Lett. 114 (2015) 170503 1-5.

EPR investigation of the aggregation of copper porphyrin

A.E. Bardasova[1], A.A. Sukhanov[2], V.K. Voronkova[2], V.S. Tyurin[3]

[1]Kazan (Volga region) Federal University, Kremlevskaya str. 18, 420008 Kazan, Russian Federation

[2]Kazan E.K. Zavoisky Physical-Technical Institute, Russian Academy of Sciences, 420029, Kazan, Russian Federation

[3]A.N. Frumkin Institute of Physical chemistry and Electrochemistry RAS, 119071, Moscow, Russian Federation

e-mail: alinabardasova@gmail.com

At the present time there is considerable interest in intramolecular energy transfer in compounds, which absorb visible light, because it is crucial to the better understanding of photo-harvesting systems in photosynthesis and for utilizing solar energy [1-2]. Porphyrin dimers are one of the best systems for the investigation of light-induced intramolecular energy transfer. Many porphyrins and porphyrin dimers have been studied over the past decade [3], however small attention has been paid to the influence of paramagnetic metals on the photoinduced states of metalloporphyrins. Dimer porphyrin play specialized roles in photosynthetic plants and organisms [4]. In this work, Electron Paramagnetic Resonance Spectroscopy (EPR) is used to study such compounds.

Porphyrin molecules can be transferred from the diamagnetic state to the excited triplet paramagnetic state by the optical excitation. It is known that intramolecular nonradiative intersystem crossing (ISC) of the porphyrin molecules from the photoexcited singlet state to the triplet state is spin-selective and therefore the triplet spin sublevels of are not populated equally. This non-equilibrium distribution of populations is known as an example of the effect of the so-called chemically induced dynamic electron polarization [5]. The effect of the non-equilibrium electron spin polarization of photoexcited molecules can be registered using time-resolved EPR spectroscopy (TR EPR) [6]. In this method, we register the time-dependent signal is produced by laser excitation in magnetic field.

Aggregation and the resulting changes in visible light absorption have important consequences in nature and in technological applications. In general, aggregation of porphyrins was studied in aqueous solutions [7]. Aggregation in organic solutions is changing. The degree of aggregation depends on the conditions, concentration, and structure of porphyrins.

In this report, we present results of the CW and TR EPR investigations aggregation effect of new copper complex of tetra ethyl coproporphyrin I (CuCPP-1) (fig.1).

The CW and TR EPR experiments were carried out on frozen solutions of the CuCPP-1 complex in a mixture of chloroform and isopropanol (1:1) and in *o*-terphenyl. TR EPR experiments were carried out using laser excitation at 532 nm. The EPR measurements were performed on an X-band EPR Elexsys E-580 spectrometer (Bruker). The TR EPR spectra were obtained by the summation of the data in different time windows after the laser pulse.

The EPR spectrum of copper ion in the ground state of the CuCPP-1 complex in o-terphenyl

The CW EPR spectra of the ground state CuCPP-1 complexes in *o*-terphenyl is presented in fig.2. The spectra have the shape typical for the copper complex because in the

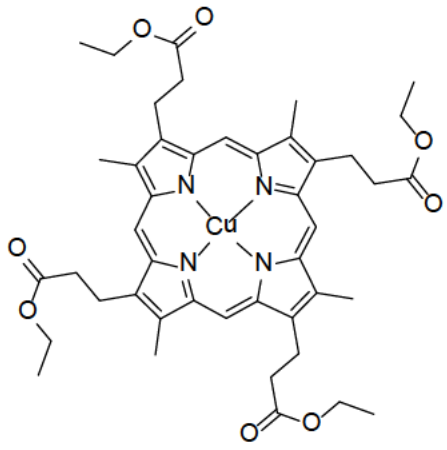

Fig.1. Chemical structure of CuCPP-1

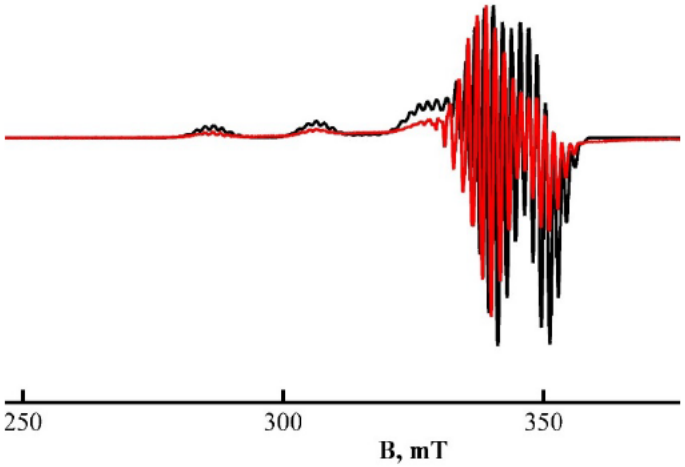

Fig.2. Experimental (red line) and simulated (black line) spectra of the CuCPP-1 complex in o-terphenyl at T = 80 K

ground-state CuCPP-1 complexes the copper ion is the only paramagnetic center [8]. The EPR spectra of the CuCPP-1 complexes before photoexcitation manifest the hyperfine structure due to the interaction of the copper ion unpaired electron with four nitrogen nuclei ^{14}N in the complex. The EPR spectrum was simulated in accordance with the Hamiltonian $H = \mu_B gB + SA\left(\mathrm{Cu}^{2+}\right)I_{\mathrm{Cu}} + \sum_{i=1}^{4} SA\left(N_i\right)I_N$, where $S = 1/2$, $I_{\mathrm{Cu}} = 3/2$, $I_N = 1$, $g_\perp = 2.038 \pm 0.001$, $g_\parallel = 2.190 \pm 0.001$, $A_\perp(\mathrm{Cu}^{2+}) = 57 \pm 3$MHz, $A_\parallel(\mathrm{Cu}^{2+}) = 603 \pm 5$ MHz, $A(\mathrm{N_1}) = A(\mathrm{N_2}) = A(\mathrm{N_3}) = A(\mathrm{N_4}) = 48 \pm 3$ MHz.

The EPR spectrum of copper ion in the ground state of the CuCPP-1 complex in frozen mixture solutions of chloroform and isopropanol

The CW EPR spectra of the ground state CuCPP-1 complexes in frozen mixture solutions of chloroform and isopropanol is presented in fig.3. The spectrum consists two type spectra. We supposed that this spectrum is the sum of spectra of dimer and monomer CuCPP-1 complex. According this theoretical consideration we simulated spectrum of dimer CuCPP-1. The EPR spectrum was simulated in accordance with the Hamiltonian $H = \mu_B \sum_{i=1}^{2}\left[g_i BS_i + I_i A\left(\mathrm{Cu}^{2+}\right)_i S_i\right] + S_1 JS_2 + S_1 DS_2$, where $S_1 = S_2 = 1/2$, $I_1 = I_2 = 3/2$. Two

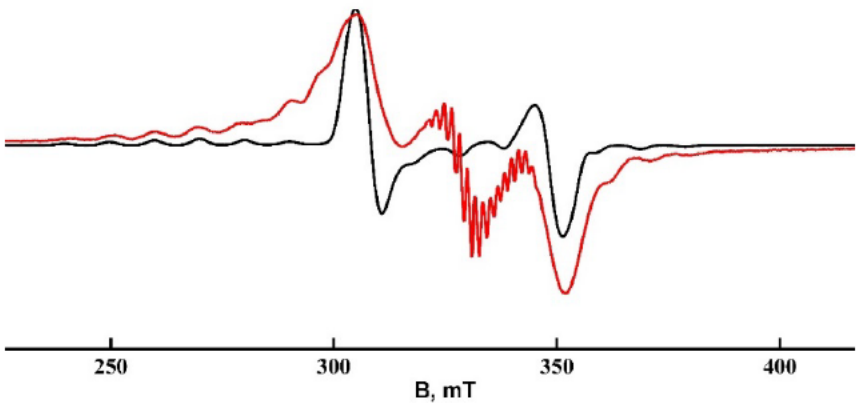

Fig.3. Experimental (red line) and simulated (black line) spectra of the CuCPP-1 complex in frozen mixture solutions of chloroform and isopropanol at T = 100 K

last terms in this spin-Hamiltonian describes exchange and dipole-dipole interactions between two spin S_1 and S_2, respectively. For simulation of spectra, we supposed that exchange interaction much more than hyperfine interaction ($J >> A(Cu^{2+})$). To describe experimental spectrum we fitted only value of dipole-dipole interaction. The best result of fitting is presented in fig.3 with following parameter set: $g_\perp = 2.05 \pm 0.001$, $g_\| = 2.180 \pm 0.001$; $A_\perp(Cu^{2+}) = 57 \pm 3$ MHz, $A_\|(Cu^{2+}) = 603 \pm 5$ MHz; $D_x = D_y = -800$ MHz, $D_z = 1600$ MHz.

Well known that dipole-dipole interaction defined as [9],

$$\mathbf{D} = \frac{\mu_B^2}{R^3}\left(\mathbf{g_1 g_2} - 3\left(\mathbf{g_1 R}\right)\left(\mathbf{R g_2}\right)\right),$$

where **R** – radius-vector connecting two spins.

According this expression we estimates distance (R) between two CuCPP-1 complexes in dimer. R is about 4.25 ± 0.03 Å.

The EPR spectrum of the photoexcited CuCPP-1 complex

Experimental results are presented in fig.4 and fig.5. At the fig.4 the TR EPR spectrum of the photoexcited CuCPP-1 complex in the frozen mixture solutions of chloroform and isopropanol is shown. The experimental spectra until about 40 μs after laser flash consist only of the absorption (A) signals, after 40 μs spectra consist only emission (E) signals. The spectrum shape changes on the detection time interval.

At the fig.5 the TR EPR spectrum of the photoexcited CuCPP-1 complex in *o*-terphenyl is shown. The experimental spectra consist only emission signal. The spectrum shape don'ts change on the detection time interval.

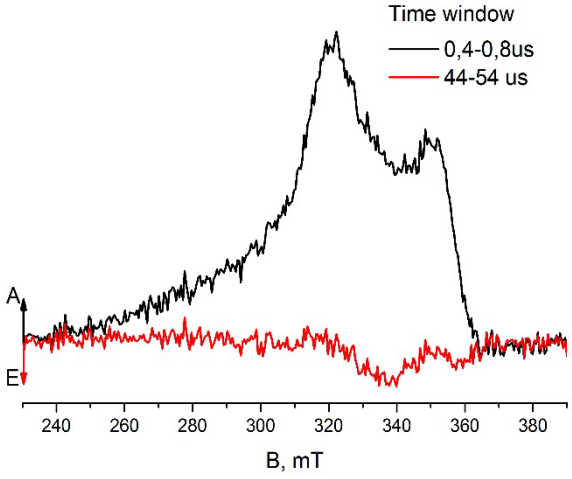

Fig.4. X-band TR EPR spectra of the photoexcited CuCPP-1 complex in the frozen mixture solutions of chloroform and isopropanol at T =40 K. Spectra are obtained by integrating the dataset in the selected time window given in the right top hand part of the figure.

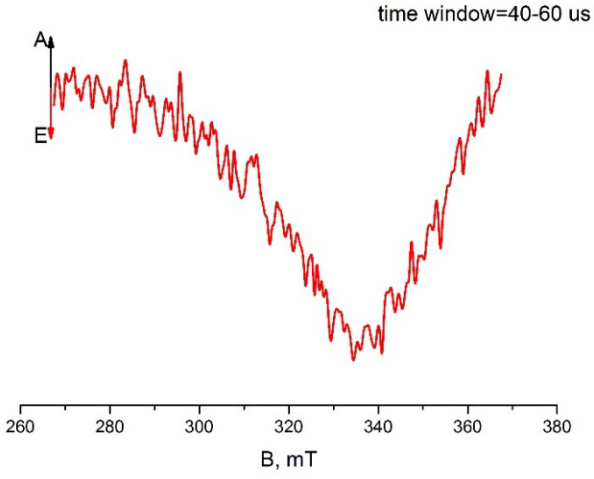

Fig.5. X-band TR EPR spectrum of the photoexcited CuCPP-1 complex in *o*-terphenyl at T=40 K is obtained by integrating the dataset in the 40 – 60 μs time window.

TR EPR spectra of CuCPP-1 complex in the frozen mixture solutions of chloroform and isopropanol and in *o*-terphenyl are different. We suppose that TR EPR spectra of CuCPP-1 in the frozen mixture solutions of chloroform and isopropanol consist different type TR EPR spectra. TR EPR spectra of CuCPP-1 in o-terphenyl are typical spectrum for ground state of

copper ion [10]. After about 40 us after laser flash TR EPR spectra of CuCPP-1 in the frozen mixture solutions of chloroform and isopropanol induced by ground polarized state of copper ion. At early time after laser flash TR EPR spectra of CuCPP-1 in the frozen mixture solutions of chloroform and isopropanol are more complicated.

Conclusions

The copper complex of tetra ethyl coproporphyrin I was experimentally studied by EPR techniques. We found that there is self-dimerization of this complex in the mixture solutions of chloroform and isopropanol (1:1). It was estimate the distance between CuCPP-1complex in the dimer. Ground polarized state of copper ion was found for the photoexcited CuCPP-1 complex in o-terphenyl. Polarized states of photoexcited CuCPP-1 complex in the mixture solutions of chloroform and isopropanol (1:1) are more complicated.

Acknowledgements

This work was supported in part of EPR studies by the Russian Foundation for Basic Research (project no. 16-03-00586) and Program of Presidium RAS (no.1.26).

References

[1] C. Stangel, C. Schubert, S. Kuhri et al., Nanoscale **7**, 2597-2608 (2015).

[2] L. Moreira, J. Calbo, B. Illescas et al., Angewandte Chemie International Edition **54**, 1255-1260 (2015).

[3] R. Paolesse, K.M. Kadish, K.M. Smith, R. Guilard, The Porphyrin Handbook. Kadish, K.M., 201-232 (2000).

[4] K. Sauer, J.R.L. Smith, A.J. Schultz, Journal of the American Chemical Society **88**, 2681-2688 (1966).

[5] J.B. Pedersen, J.H. Freed, Journal of Chemical Physics **58**, 2746-2762 (1973).

[6] H. Levanon, J.R. Norris, Chemical Reviews **78**, 185-198 (1978).

[7] M.Y Choi, J.A. Pollard, M.A. Webb, J.L. McHale, Journal of the American Chemical Society **125**, 810-820 (2003).

[8] A.A. Sukhanov, K.B. Konov, K.M. Salikhov, V.K. Voronkova et al., Applied Magnetic Resonance **46**, 1199-1220 (2015).

[9] A. Bencini, D. Gatteschi, Electron paramagnetic resonance of exchange coupled systems. Springer-Verlag (1990).

[10] V.S. Iyudin, Yu.E. Kandrashkin, V.K. Voronkova, V.S. Tyurin et al., Applied Magnetic Resonance **40**, 75-89 (2011)

EPR and spin-lattice relaxation in nanoscale hydroxyapatite powder

M.R. Gafurov[1], T.B. Biktagirov[1], G.V. Mamin[1], D.V. Shurtakova[1], E.S. Klimashina[2], V.I. Putlyaev[2], S.B. Orlinskii[1]

[1]Kazan Federal University, Institute of Physics, 420008, Kremlevskaya st, Kazan, Russian Federation

[2]Moscow State University, Moscow, 119992 Russia

e-mail: darja-shurtakva@mai.ru

Hydroxyapatite (HAp) is a calcium phosphate similar to the mineral component of bones and hard tissues in mammals. HAp is used for orthopedic, dental and maxillofacial applications. Improving the properties of calcium phosphate used in medicine is require go to the nanoscale HAp (less than 1000 nm). The properties of nanoscale materials may differ largely from bulk material.

The aims of the work were the synthesis of the "undoped" hydroxyapatite powder as well as doped by manganese ions in concentration of 0.05 mol.% with the size of crystallites of 30 nm and 1 micron and study the temperature dependences of relaxation rates of impurity paramagnetic centers in the temperature range 6 – 300 K.

After X-ray irradiation NO_3^{2-} complexes EPR spectrum was detected in undoped samples (fig.1). It has been approximated using a spin Hamiltonian [1]

$$\tilde{H} = \beta H(g_{||}S_z\cos\theta + g_{\perp}S_y\sin\theta) + A_{||}S_zI_z + A_{\perp}(S_xI_x + S_yI_y) - \beta H(g_{||}^1 I_z\cos\theta + g_{\perp}^2 I_x\sin\theta)$$

As seen from the figure insert hyperfine coupling constants distribution need to add to models. This parameter can be connected with distribution of particle size in powder. The parameters of the EPR spectrum of NO_3^{2-} complexes in the undoped hydroxyapatite had found for both (30 and 1000 nm) samples. It was found, the parameter such as the width of the distribution of the hyperfine coupling constants differs by almost 2 times for nano-sized and micro-sized samples.

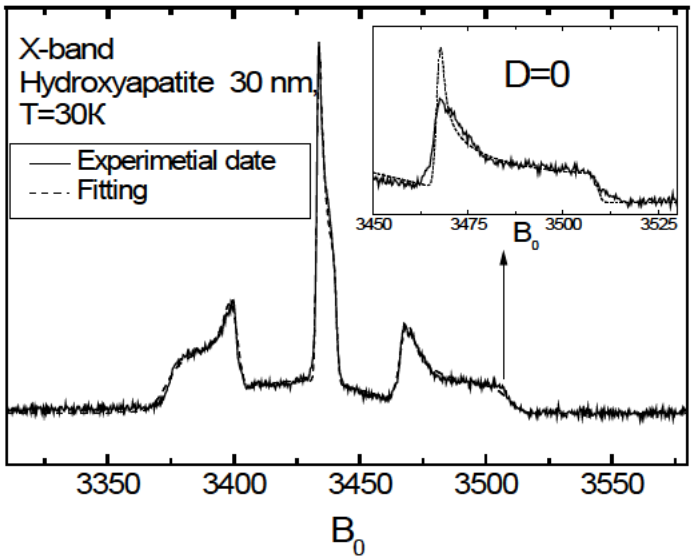

Fig.1. The experimental EPR spectrum of NO_3^{2-} complexes in hydroxyapatite powder (solid line) and its simulated (dash line).

The temperature dependences of spin-lattice relaxation rates of NO_3^{2-} complexes for both nano-sized and micro-sized samples are shown in fig.2. The experimental data were described in the theoretical Orbach's model and Debye temperature (Θ) values were extracted from the fittings. These values of Θ are found to be different for nano-sized (Θ_{nano} = 275 K) and micro-sized (Θ_{micro} = 328 K) samples. Both these values are lower than the Debye temperature extracted from the heat capacity model. ($\Theta_{thermal}$ = 420 K) [2].

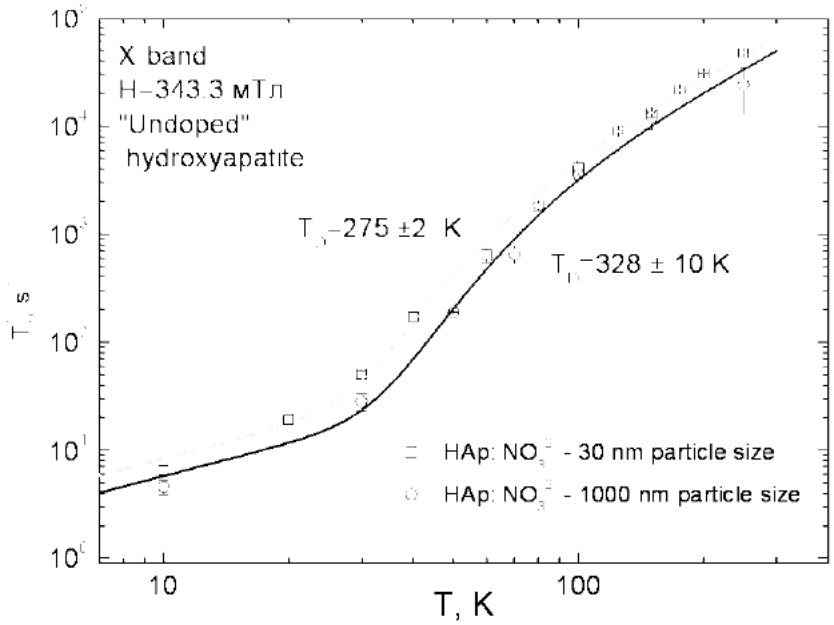

Fig.2. The temperature dependence T_1^{-1} spin-lattice relaxation of NO_3^{2-} complexes in "undoped" hydroxyapatite samples with particle size 30 nm (dash line) and 1000 nm (solid line). The approximation in theoretical Orabh's model is shown by solid lines.

Also the hydroxyapatite powder with the particle size of 30 nm doped by manganese ions (0.5 mol.%) was studied. EPR characteristics of the Mn^{2+} containing ions for "dry" and "wet" samples (with the addition of alcohol) were measured. The temperature dependence of spin-lattice relaxation rates is shown in fig.3. The influence of alcohol phonon bridges

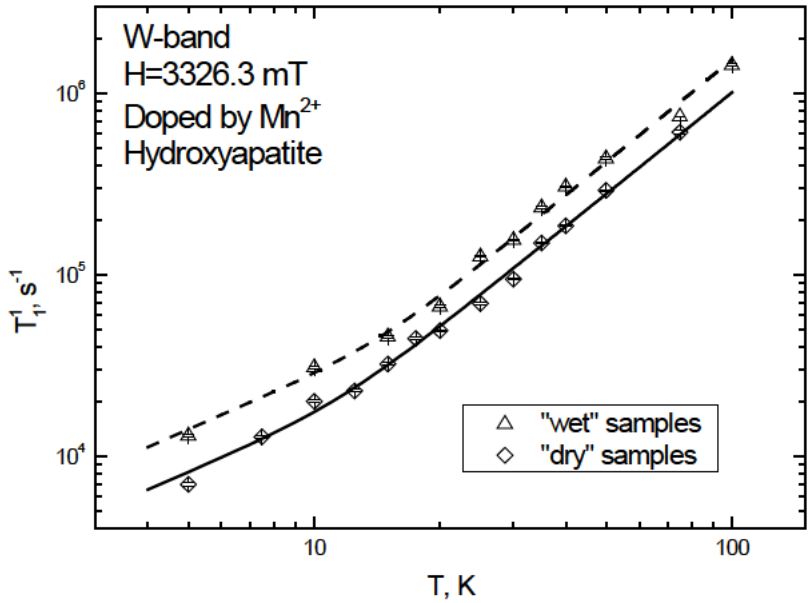

Fig.3. The temperature dependence T_1^{-1} for ions Mn^{2+} in doped with manganese hydroxyapatite samples, for "dry" and "wet" samples in в W-band.

between nanoparticles on relaxation parameters can be observed.

The obtained results show how the study of the relaxation characteristics can be used to track the size effects. Further theoretical description of the obtained experimental findings is in need.

References

[1] Gafurov, M. R. Study of the Effects of Hydroxyapatite Nanocrystal Codopingby Pulsed Electron Paramagnetic Resonance Methods /M. R. Gafurov, T. B. Biktagirov, G. V. Mamin, D. V. Shurtakova, E. S. Klimashina, V. I. Putlyaev, and S. B. Orlinskii // Physics of the Solid State, 2016, Vol. 58, No. 3, pp. 469–474.

[2] Schaefer, H. E. Nanoscience: the science of the small in physics, engineering, chemistry, biology and medicine / H. E. Schaefer.–Stuttgart: Springer, 2010. – P. 772.

Dysfunction of mitochondria and adipose tissue inflammation in patients with rectal cancer

A.P. Burlaka[1], I.I. Ganusevych[1], A.V. Vovk[1], V.V. Golotiuk[2], A.A. Rodionov[3], S.M. Lukin[1]

[1]Kavetsky Institute of Experimental Pathology, Oncology and Radio-biology of NAS of Ukraine, Kyiv, Ukraine

[2]Ivano-Frankivsk National Medical University, Ukraine

[3]Kazan Federal University, Kazan, Russia

e-mail: apburlaka@gmail.com

Cancer, including colorectal cancer (CRC), is one of the causes of increase in mortality in the developed world. It is known that there is a causal relation between obesity and cancer, but the mechanisms responsible for this are not clear. To date obesity is considered as a chronic inflammatory disease and obesity factors as additional damaging factor for metabolic disorders. On the other hand, chronic inflammation is recognized as etiopathogenetical factor in the development of some cancers of epithelial origin (in particular, there are evidences regarding cancer of the esophagus, liver, colon, mammary gland in postmenopausal and endometrial cancer). Superoxide radicals (SR), generated by adipocytes, and presence of free lipids, released by adipocytes to the tumor microenvironment, promote the adhesion, migration and invasion of tumor cells and support the tumor progression and its uncontrolled growth. One of the targets sensitive to damaging influence of tumor in obesity are mitochondria of adipocytes. It is known that the levels of proinflammatory cytokines – a serumal tumor necrosis factor (tumor necrosis factor α - TNF-α) – increase in obesity and decrease with weight loss [1-3].

Considering the above, the purpose of the work was to investigate the redox-dependent mechanism in normal adipose tissues (NAT) of patients without cancer; in adipose tissues (AT) of patients with CRC adjacent to the tumor (ATAT) and at a distance of 3 cm from it (ATD); activity of matrix metalloproteinase (MMP-2 and -9) in these tissues, and the impact of TNF-α on them.

The research was carried out on 46 samples of ATAT and 26 samples of ATD of patients with CRC at disease stages II-III. As a control, the NAT of 11 healthy people was used which was obtained after liposuction performed in a specialized medical center in compliance with sterility. The samples from 25 men and 21 women with the average age of 64.0 ± 1.6 years were examined. Methods of electron paramagnetic resonance (EPR) including spin-trapping techniques for SR and nitrogen oxide (NO) detection and quantification, polyacrylamide gel zymography, different biochemical and statistical methods were used [4-9].

The obtained results are presented in fig.1 – fig.4. They show that under the influence of factors of malignant tumor the precancerous phenotype of ATAT is formed which is characterized by high levels of SR and activity of MMP. The incubation of NAT, ATD and ATAT with pro-inflammatory cytokine TNF-α causes changes in redox state of mitochondria and activation of a number of factors of inflammation (SR, $NO^{\cdot}$, MMP) only in tissues where the reprogramming of metabolism has already occurred under the influence of tumor – in ATAT and to a lesser degree in ATD.

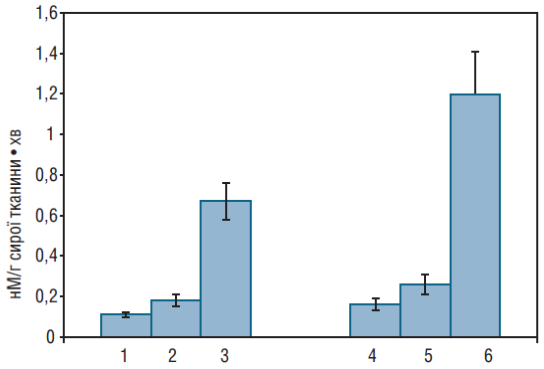

Fig.1. Rate of SR generation by mitochondria of NAT (1), ATD (2) and ATAT (3) before and after (respectively 4, 5, 6) the incubation with TNF-α

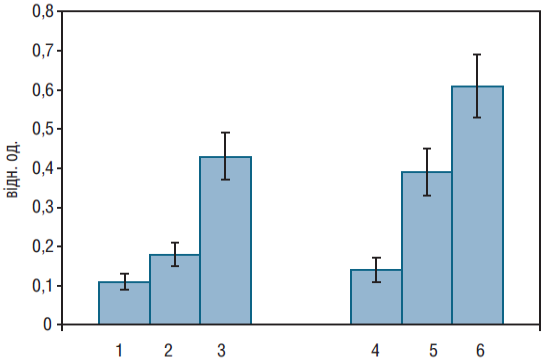

Fig.2. Level of NO-FeS-proteins complexes in ETC of mitochondria in cells of NAT (1), ATD (2) and ATAT (3) before and after (respectively 4, 5, 6) the incubation with TNF-α

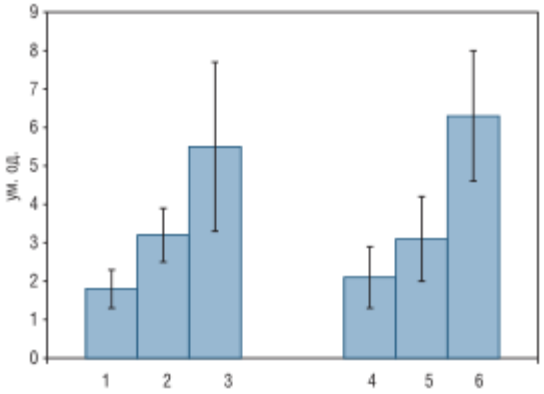

Fig.3. Activity of MMP-2 in NAT (1), ATD (2) and ATAT (3) before and after (respectively 4, 5, 6) the incubation with TNF-α

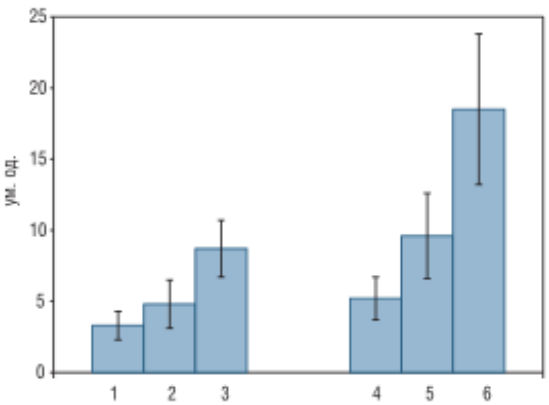

Fig.4. Activity of MMP-9 in NA (1), ATD (2) and ATAT (3) before and after (respectively 4, 5, 6) the incubation with TNF-α

References

[1] Marseglia L, Manti S, D'Angelo G, et al. (2015) Oxidative stress in obesity: a critical component in human diseases. Int J Mol Sci 16 (1): 378–400.

[2] Schwartz B, Yehuda-Shnaidman E. (2014) Putative role of adipose tissue in growth and metabolism of colon cancer cells. Front Oncol 4: 164.

[3] Shabalina IG, Vrbacky M, Pecinova A, et al. (2014) ROS production in brown adipose tissue mitochondria: the question of UCP1-dependence. Biochim Biophys Acta 1837: 2017–2030.

[4] Burlaka AP, Sidorik EP, Ganusevich II, et al. (2006) High formation of superoxide anion and nitric oxide, and matrix metalloproteinases activity in vascular wall of rectal carcinoma vessels. Exp Oncol 28: 323–325.

[5] Burlaka AP, Sidorik EP (2014) Redox-dependent signal molecules in mechanism of tumor process. Naukova dumka, Kyiv

[6] Burlaka AP, Ganusevich II, Lukin SN, Gafurov MR, Sidorik EP (2014) Superoxide- and NO-Dependent Mechanisms of the Reprogramming of Bone Marrow Cells by Tumor Cells. Appl. Magn. Reson. 45:1261-1273

[7] Burlaka AP, Ganusevich II, Gafurov MR, et. al. (2016) Stomach Cancer: Interconnection between the Redox State, Activity of MMP-2, MMP-9 and Stage of Tumor Growth. Cancer Microenviroment, 9: 27-32.

[8] Burlaka AP, Ganusevich II, Golotiuk VV, Vovk AV, Lukin SM (2016) Superoxide- and NO-dependent mechanisms of antitumor and antimetastatic effect of L-arginine hydrochloride and coenzyme Q10. Exp Oncol. 38: 31-35.

[9] Burlaka AP, Gafurov MR, Iskhakova KB et al. (2016) Electron Paramagnetic Resonance in the Experimental Oncology: Implementation Examples of the Conventional Approaches. BioNanoScience DOI: 10.1007/s12668-016-0238-5 (in press)

Conformational NMR analysis of small flexible molecules by 2D NOESY

I.A. Khodov[1,2], S.V. Efimov[2], V.V. Klochkov[2] M.G. Kiselev[1]

[1]G.A. Krestov Institute of Solution Chemistry of the Russian Academy of Sciences, 153045, ul. Akademicheskaja d. 1, Ivanovo, Russian Federation.

[2]Institute of Physics of the Kazan Federal University, 420008, Kremlevskaya St. 18, Kazan, Russian Federation.

e-mail: iakh@isc-ras.ru

In recent decades two-dimensional NMR spectroscopy has been showed to be a useful technique for the spatial structure determination of small flexible molecules [1,2]. Knowing the conformational state of small drug molecules, is important to considering the phenomenon of polymorphism [3,4]. Information on the conformation distribution in saturated solutions can facilitate our understanding of the mechanisms of nucleation of a given crystalline form of the studied compound. NMR spectroscopy has become the leading method in the field. There are several spectroscopic ways to obtain information on the preferred conformation of small molecules. The first way is the analysis of NMR lineshapes or measuring integral intensities from two different conformers of a small molecule at a low temperature.[5-7]. The ain restriction of this approach is the fact that conformational preferences may be different at various temperatures. This approach is useful only for conformers with a significant difference in their energies. The second way is to analyze the ^{1}H-^{1}H scalar coupling constants ($^{2}J_{HH}$ and $^{3}J_{HH}$) to obtain the configuration of pairs of geminal and vicinal protons.[8]. The value of this constant provides detailed information on the orientation and dihedral angle between the two hydrogen atoms. However, it deals with one-dimensional ^{1}H NMR spectra which usually do not allow to observing observe NH and OH groups. The third way is based on the residual dipolar coupling (RDC) effect. It is observed if the molecules in solution exhibit a partial alignment in anisotropic media. The resulting RDC values are used in determination of proton dipole-dipole interaction. This approach is less sensitive to small population changes.[4]. The best way of structure determination of small molecules is the nuclear Overhauser effect spectroscopy (NOESY) analysis. It was shown by Craig Butts [1-3] and others that the NOESY technique yields reasonably accurate interproton distances (with the relative inaccuracy of several per cent) for small organic molecules, as exemplified on strychnine – the model compound for NMR studies. Note that this method is readily applied only for rigid molecules, and special precautions should be made when studying compounds with fast conformational exchange. Intramolecular mobility should be taken into account and effective (mean) internuclear distances should be correctly found. Moreover, the influence of spin diffusion (relayed magnetization transfer) should be considered for in studies of small flexible molecules because it can distort the results noticeably. These techniques were critically analysed, and two methods were tested during the study of felodipine as the drug molecule of small size. 2D QUIET-NOESY was found to be a powerful technique to the conformational preference determination. The second way, combined analysis of two sets data of spectra, NOESY and T-ROESY, was tested and proved to be the most correct way of obtaining conformational preference for the flexible molecule in solution.

Acknowledgments

The authors thank Prof. S. Berger and Prof. Daniel Huster (University of Leipzig, Germany). IK is thankful for partial funding from the President of the Russian Federation and from the Russian Foundation for Basic Research (project nos. MK-9048.2016.3 and 16-03-

00640, 16-53-150007). Part of this work performed at Kazan University was funded by the subsidy of the Russian Government to support the Program of Competitive Growth of Kazan Federal University among World's Leading Academic Centers.

References

[1] Butts C.P., Jones C.R., Towers E.C., Flynn J.L., Appleby L., Barron N.J. Interproton distance determinations by NOE – surprising accuracy and precision in a rigid organic molecule. Org Biomol Chem. 2011;9(1):177-184. doi:10.1039/C0OB00479K.

[2] Jones C.R., Butts C.P., Harvey J.N. Accuracy in determining interproton distances using Nuclear Overhauser Effect data from a flexible molecule. Beilstein J Org Chem. 2011;7:145-150. doi:10.3762/bjoc.7.20.

[3] Butts C.P., Jones C.R., Song Z., Simpson T.J. Accurate NOE-distance determination enables the stereochemical assignment of a flexible molecule - arugosin C. Chem Commun. 2012;48(72):9023-9025. doi:10.1039/C2CC32144K.

[4] Oparin R.D., Moreau M., De Walle I., Paolantoni M., Idrissi A., Kiselev M.G. The interplay between the paracetamol polymorphism and its molecular structures dissolved in supercritical CO2 in contact with the solid phase: In situ vibration spectroscopy and molecular dynamics simulation analysis. Eur J Pharm Sci. 2015;77:48-59. doi:10.1016/j.ejps.2015.05.016.

[5] Khodov I.A., Efimov S.V., Klochkov V.V., Alper G.A., Batista de Carvalho L.A.E. Determination of preferred conformations of ibuprofen in chloroform by 2D NOE spectroscopy. Eur J Pharm Sci. 2014;65:65-73. doi:10.1016/j.ejps.2014.08.005.

[6] Belova N.V., Girichev G.V., Oberhammer H., Hoang T.N., Shlykov S.A. Tautomeric and conformational properties of benzoylacetone, CH 3-C(O)-CH 2-C(O)-C 6H 5: Gas-Phase electron diffraction and quantum chemical study. J Phys Chem A. 2012;116(13):3428-3435. doi:10.1021/jp2118967.

[7] Belova N.V., Oberhammer H., Trang N.H., Girichev G.V. Tautomeric properties and gas-phase structure of acetylacetone. J Org Chem. 2014;79(12):5412-5419. doi:10.1021/jo402814c.

[8] Belova N.V., Sliznev V.V., Oberhammer H., Girichev G.V. Tautomeric and conformational properties of β-diketones. J Mol Struct. 2010;978(1-3):282-293.

[9] Bothner-by A.A. Advances in Magnetic Resonance. Vol 1.; 1965. doi:10.1016/B978-1-4832-3114-3.50011-8.

Supramolecular systems of peptides and cucurbit[7]uril

E.A. Kovalenko

Nikolaev Institute of Inorganic Chemistry, SB RAS, 630090, Lavrentiev av., 3, Novosibirsk, Russia.

e-mail: e.a.kovalenko@niic.nsc.ru

Supramolecular systems are regularly used regarding their reversibility, dynamic interactions with biomolecules and easy modification via non-covalent synthesis. Directional non-covalent interactions such as hydrogen bonding and host–guest interactions have the advantage of specificity and tunability. This is reflected in recent research on the co-assembly of peptides and organic compounds yielding new interesting properties. Host–guest assemblies based on cyclodextrin and cucurbit[n]uril have been shown to form stable complexes with varying degrees of selectivity and reversibility.

Here we report about supramolecular complexation of dipeptides (Gly-Val and Gly-Leu, fig.1), tetrapeptide Tuftsin (Thr-Lys-Pro-Arg) and cucurbit[7]uril (CB[7]), which were investigated by NMR in solution for different experimental conditions. ^{1}H NMR spectra of the solutions of the peptides complexes with CB[7] indicates a balance between free peptides and forms, differing in the nature of inclusion in cucurbit[7]uril. Chemical shift upfield change and broad forming signals confirm host–guest interactions (fig.2.).

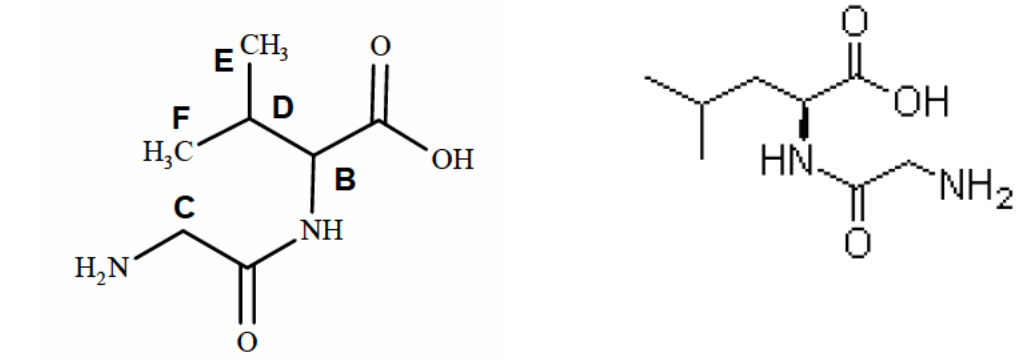

a) b)

Fig.1. Structures of dipeptides: a) Gly-Val and b) Gly-Leu

The host–guest complexation between Tuftsin and CB[7] was also confirmed by fluorescent titration procedure. Quantum chemical calculations were used to complement experimental results. According to DFT calculations, a structural binding motif involve hydrogen bonding. The most energetically stable form is when Arg-side (fig.3) chain situated in CB[7] cavity.

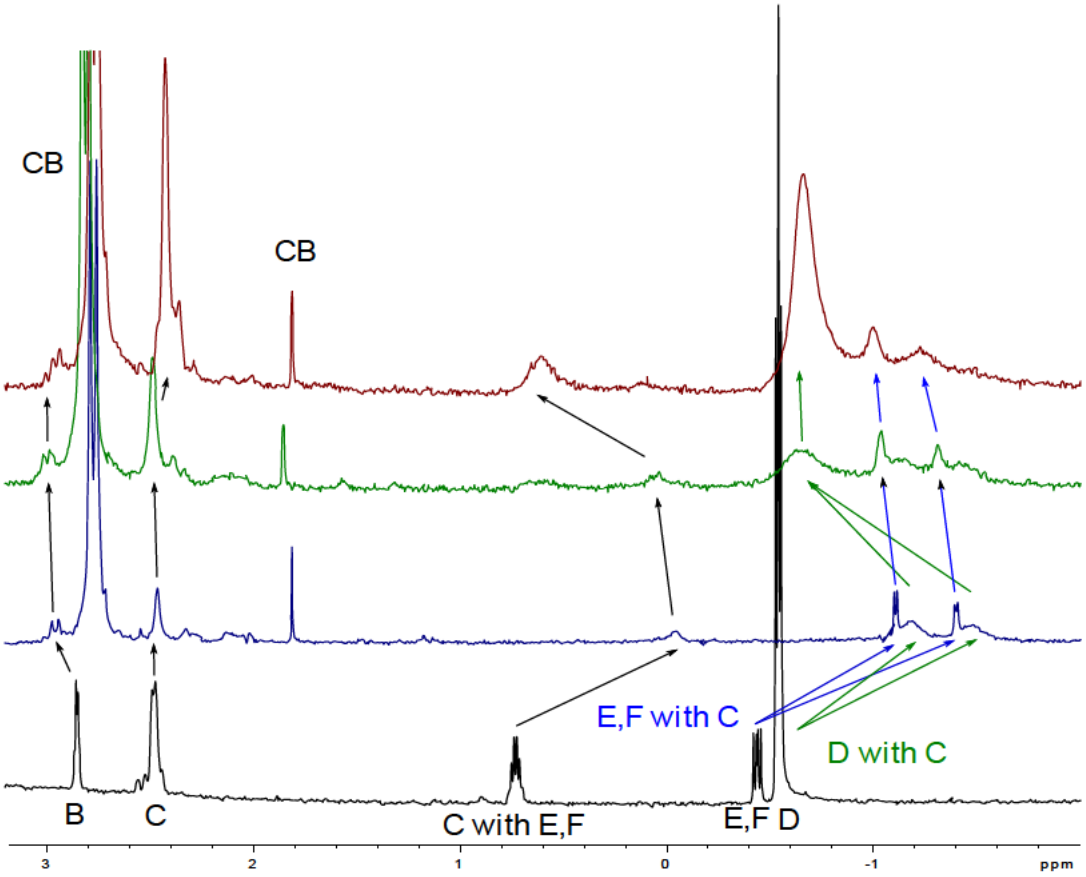

Fig.2. ^{1}H NMR spectra of free Gly-Val, Gly-Val:CB[7] mixture in the molar ratio 1:1, 2:1, 3:1 (upwards) in D_2O solution.

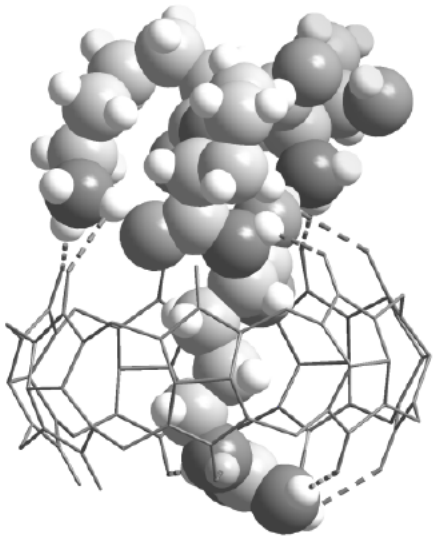

Fig.3. Structure of Tuftsin@CB[7] from DFT calculation

This work was supported by the Council on Grants at the President of the Russian Federation (Government Support Program of Leading Scientific Schools NSh-7178.2016.3)

^{87}Sr NMR study of inhomogeneous state in $Sr_{1-x}La_xMnO_3$ (x = 0; 0.02; 0.04)

A. Germov, Z. Volkova, A. Gerashenko, S. Verkhovskii, K. Mikhalev

Institute of Metal Physics, Ural Branch of the Russian Academy of Sciences, 620990, S. Kovalevskaya st. 18, Yekaterinburg, Russian Federation.

e-mail: germov@imp.uran.ru

Introduction

Electron-doped manganites with perovskite structure display a great variety of electronic properties. One of the main issues of these materials arises from competition of the antiferromagnetic (AF) superexchange interaction between localized spins and the ferromagnetic (FM) double-exchange interaction of the localized spins of doped carriers. At recent studies [1-3] the magnetic state of perovskites is considered as nonhomogeneous with FM domains embedded in antiferromagnetic lattice.

Cubic perovskite $SrMnO_3$ is a rare example of G-type cubic antiferromagnet. High symmetry influences on its properties such as increasing covalence of the Mn-O-Mn bonds. Also, cubic $SrMnO_3$ lightly doped (~1%) by substitution of La^{3+} and Ce^{4+} for Sr^{2+} reveals a metallic-like conductivity behavior. Such behavior is accompanied by picture of a canted AF metal as ground state [4].

Our recent research [5] evidences for inhomogeneous magnetic state where AF insulator lattice contains FM clusters. However, ^{55}Mn spectra could be obtained only in magnetic ordered state (T_N = 230). Thus, in order to obtain the information about the electronic structure and the local field distribution in paramagnetic state we have to use other NMR probe like ^{87}Sr.

Experimental results and discussion

We have obtained the NMR spectra of ^{87}Sr in electron-doped cubic polycrystalline manganites $Sr_{1-x}La_xMnO_3$ (x=0; 0.02; 0.04) in external magnetic field 11.747 T at the temperature range from 20 K to 370 K (fig.1.).

Spectrum of $SrMnO_3$ is represented by single symmetric line, showing negligible quadrupole broadening and peaking at the high frequency (K=0.27%) with respect to the line position of standard reference $SrCl_2$ (K=0). The line width has nonmonotonic temperature dependence (fig.2.). Most interesting sharp growth of the line width below 60 K is connected with magnetic polaron localization [5]. Exactly at these temperatures sharp growth of bulk magnetization is observed [6].

Unlikely to initial $SrMnO_3$, the spectra of La-doped samples reveal sufficient growth of spectral intensity at higher frequency (fig.1.). The spectral line width at half maximum of La-doped samples increases with decreasing temperature up to 120 K and then decreases in two times at lower temperatures (fig.2.). The broadening of spectra occurs mainly due to distribution of local magnetic fields at the Sr sites. The fluctuating component of local fields results in distribution of the rate of ^{87}Sr spin echo decay, thus allowing separating the Sr sites with different environment of La atoms. It has been confirmed by spectrum with distinct delay time (t_{delay}) between pulses at room temperature (fig.1).

The spectra of La-doped samples include the line of initial $SrMnO_3$. This line is most probably connected with Sr^{2+} ions that placed far from FM correlated formations, including La^{3+} ions. Decreasing of the intensity of this line with increasing doping concentration

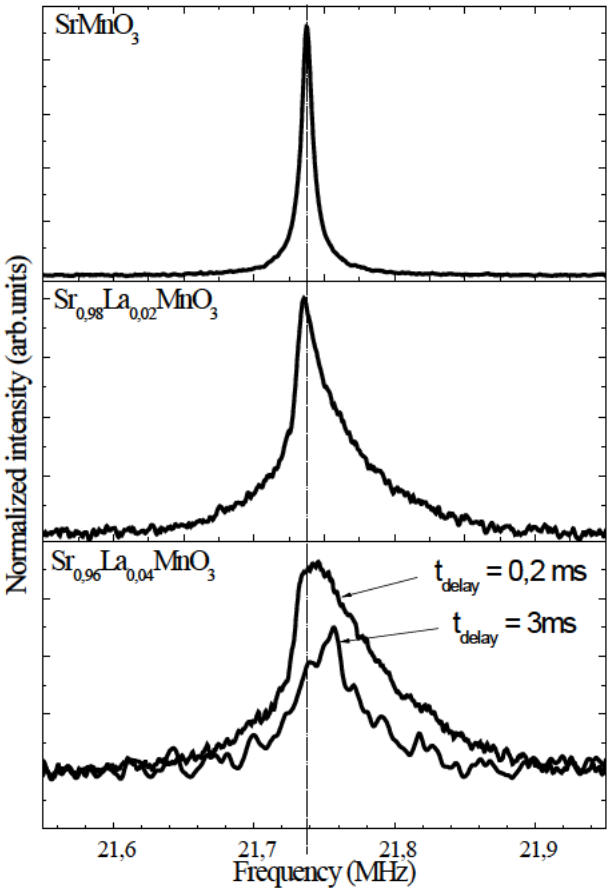

Fig.1. ^{87}Sr NMR spectra of $Sr_{1-x}La_xMnO_3$ (x =0; 0.02; 0.04) in external magnetic field 11.747 T at 295 K.

confirms nonhomogeneous state of the samples. Percolation phenomenon may take place. In addition this points out on reduced dimensionality of the FM clusters. In summary, our ^{87}Sr NMR results is directly evidence for inhomogeneous distribution of the doped carriers in paramagnetic state of the $Sr_{1-x}La_xMnO_3$ (x = 0.02; 0.04).

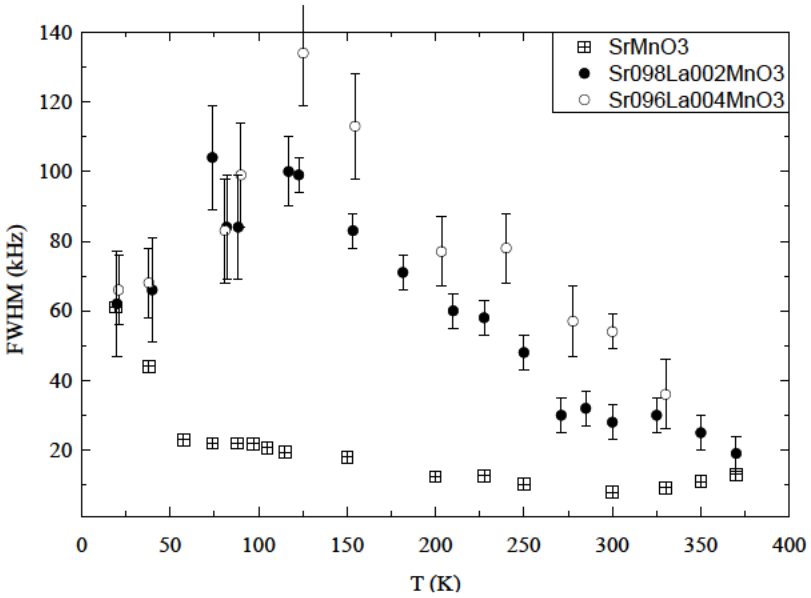

Fig.2. Temperature dependencies of the ^{87}Sr NMR spectra line width of $Sr_{1-x}La_xMnO_3$ (x =0; 0.02; 0.04).

Acknowledgements

This study is supported by the project of fundamental researches of the Ural Branch of the Russian Academy of Sciences № 15-9-2-49 in the assignment of the state program «Spin» № 01201463330.

References

[1] J. J. Neumeier and J. L. Cohn, Phys. Rev. B **61**, 14319 (2000).

[2] C. Chiorescu, J. L. Cohn, and J. J. Neumeier, Phys. Rev. B **76**, 020404(R) (2007).

[3] H. Terashita and J. J. Neumeier, Phys. Rev. B **71**, 134402 (2005).

[4] H. Sakai et. al., Phys. Rev. B **82**, 180409 (2010).

[5] A. Trokiner et. al., Phys. Rev. B **93**, 174413 (2016).

[6] A. Germov et. al., JETP letters, **102**, 11, 727 (2015).

Dipolar relaxation of multiple-quantum MNR coherences in a linear homogeneous chain of ^{19}F nuclei in calcium fluoroapatite

G.A. Bochkin, E.B. Fel'dman, S.G. Vasil'ev

Institute of Problems of Chemical Physics of Russian Academy of Sciences, Chernogolovka, 142432, Moscow Region, Russia

e-mail: bochkin.g@yandex.ru

Experimental and theoretical investigations of dynamics and relaxation of multiple quantum NMR coherences of the zeroth and second orders are performed in a quasi-one-dimensional chain of nuclear spins of ^{19}F in calcium fluorapatite. MQ NMR dynamics are studied on the preparation period of the MQ NMR experiment in the approximation of nearest neighbor interactions. The density matrix of the system at the end of the preparation period is used as the initial condition for the study of the relaxation process on the evolution period of the MQ NMR experiment. The relaxation asymptotics of the intensity of the MQ NMR coherence of the zeroth order is obtained. Relaxation of the MQ NMR coherence of the second order is investigated with ZZ part of the dipole-dipole interactions. The experimental data qualitatively agree with the results of the developed theory.

1. Introduction

It is well known that multiple quantum (MQ) NMR is widely used to study the nuclear spin distributions in solids. However, MQ NMR is also an important method for the investigation of various problems of quantum information processing [2] such as transmission of quantum information [3] and decoherence processes [4]. MQ NMR not only creates multi-qubit states but also allows the investigation of their relaxation under the action of the correlated spin reservoir. Relaxation of the MQ NMR coherences can be considered as the simplest model for the study of decoherence processes.

One-dimensional spin systems open up new possibilities for the investigation of dynamics and relaxation of multi-qubit clusters because a consistent quantum-mechanical theory of MQ NMR dynamics has been developed only for one-dimensional systems [5-8]. That theory shows that only MQ NMR coherences of the zeroth and plus/minus second orders arise in a one-dimensional spin chain initially prepared in the thermodynamic equilibrium state [5-8].

Relaxation of MQ coherences in one-dimensional systems has been studied earlier [4,22] using the second moments of the line shapes of the MQ coherences of the zeroth and second orders. We suggest to perform an analogous investigation using the ZZ model, where only the ZZ part of the DDI is taken into account.

The paper is organized as follows. A short review of the theory of MQ NMR dynamics [5-8] of one-dimensional systems is given is Section 2. In Section 3 we show that the intensity of the MQ NMR coherence of the zeroth order does not disappear completely due to the relaxation process and obtain the stationary intensity of that coherence. Relaxation of the MQ NMR coherence of the second order is studied in Section 4 using the ZZ model. We briefly summarize our results in section 5.

2. The theory of MQ NMR dynamics in one-dimensional systems

The theory [5-8] is based on the fact that the non-secular two-spin/two-quantum Hamiltonian [1] describing the MQ NMR dynamics is the XY Hamiltonian [10] which for a

one-dimensional system can be diagonalized exactly in the approximation of nearest neighbor interactions [10]. As a result, MQ NMR dynamics in such systems can be studied analytically. The developed theory [5-8] allows us to obtain the density matrix $\sigma(\tau)$ on the preparation period of the MQ NMR experiment [1] in the approximation of nearest neighbor interactions [11]. According to that theory [5,6] the density matrix $\sigma(\tau)$ at the moment τ can be represented as

$$\sigma(\tau) = \sigma_0(\tau) + \sigma_2(\tau) + \sigma_{-2}(\tau), \tag{1}$$

where $\sigma_i(\tau)$ $(i = -2,0,2)$ describes the MQ NMR coherence of order i.

If the number of spins $N >> 1$, the contributions $\sigma_0(\tau), \sigma_2(\tau), \sigma_{-2}(\tau)$ are [5,6]

$$\sigma_0(\tau) = \frac{1}{2}\sum_k \cos[2D\tau \sin k](1 - a_k^+ a_k), \tag{2}$$

$$\sigma_2(\tau) = -\frac{1}{2}\sum_k \sin[2D\tau \sin k] a_k a_{-k}, \tag{3}$$

$$\sigma_{-2}(\tau) = \frac{1}{2}\sum_k \sin[2D\tau \sin k] a_k^+ a_{-k}^+, \tag{4}$$

where $k = \frac{2\pi n}{N}\left(n = -\frac{N}{2}, -\frac{N}{2}+1, \ldots \frac{N}{2}-1\right)$, D is the dipolar coupling constant of nearest neighbors in the spin chain and the fermion operators a_k^+, a_k are defined as

$$a_k^+ = \frac{1}{\sqrt{N}}\sum_m \Psi^+_m e^{ikm}, \qquad a_k = \frac{1}{\sqrt{N}}\sum_m \Psi_m e^{-ikm} \tag{5}$$

where the operators Ψ_m, Ψ_m^+ can be expressed with the Jordan-Wigner transformations [12] via the spin operators

$$\Psi_m = 2^{m-1} I_1^z I_2^z \ldots I_{m-1}^z I_m^+, \qquad \Psi_m^+ = 2^{m-1} I_1^z I_2^z \ldots I_{m-1}^z I_m^- \tag{6}$$

where I_m^α $(\alpha = x, y, z)$ are the spin angular momentum operators of spin m and I_m^+, I_m^- are the raising and lowering spin angular momentum operators of spin m.

Formulas (2-6) lead to very simple expressions for the experimentally observed intensities of the MQ NMR coherences of the zeroth order ($G_0(\tau)$) and plus/minus second orders ($G_{\pm 2}(\tau)$) [5,6] for linear chains with $N >> 1$

$$G_0(\tau) = \frac{1}{2} + \frac{1}{2} J_0(4D\tau) \tag{7}$$

$$G_{\pm 2}(\tau) = \frac{1}{4} - \frac{1}{4} J_0(4D\tau) \tag{8}$$

where J_0 is the Bessel function of the first kind of order 0.

In order to verify Eqs. (7,8) we have performed a MQ NMR experiment using quasi-one-dimensional chains of ^{19}F in calcium fluorapatite ($Ca_5(PO_4)_3F$) [13]. The experiments were performed on a Bruker Avance III spectrometer with static magnetic field of 9.4 T (the corresponding frequency on ^{19}F nuclear spins is 376.6 MHz). The results in fig.1 demonstrate a good agreement of the experimental data with the theory. The best agreement was observed for $D = 16.0 \cdot 10^3$ s^{-1} (the theoretical value of $D = 16.4 \cdot 10^3$ s^{-1}).

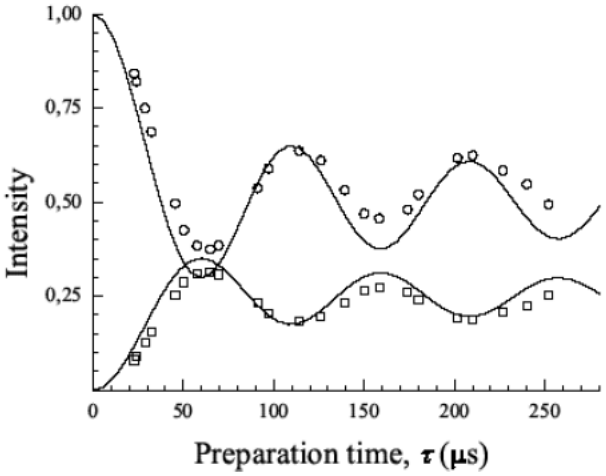

Fig.1. Experimental intensities of MQ NMR coherences of the zeroth (circles) and plus/minus second (squares) orders versus the duration of the preparation period. Solid lines are theoretical curves of Eqs. (7), (8) with dipolar coupling constant $D = 16.0 \times 10^3$ s^{-1}.

Below we use the density matrix of Eq. (1) as the initial condition for the density matrices describing the relaxation process on the evolution period of the MQ NMR experiment.

3. Relaxation of the MQ NMR coherence of the zero order

Relaxation of MQ NMR coherences on the evolution period is caused by the secular (with respect to the external magnetic field directed along the z axis) DDI

$$H_{dz} = \sum_{i<j} D_{ij}(3I_i^z I_j^z - \vec{I}_i \vec{I}_j) = \sum_{i<j} D_{ij}(2I_i^z I_j^z - I_i^x I_j^x - I_i^y I_j^y), \tag{9}$$

where D_{ij} is the coupling constant between spins i and j, and $D_{i,i+1} = D$.

The experimental results of the investigation of relaxation of the MQ NMR coherence of the zeroth order are presented in fig.2 for different durations τ of the preparation period. Unfortunately, the MQ NMR coherence of the zeroth order is not subject to relaxation in the ZZ model [13]. It is important that the experimental data in fig.2 demonstrate that relaxation does not lead to a full disappearance of the MQ NMR coherence of the zeroth order. Relaxation ends with the stationary intensity of that MQ coherence. The point is that the density matrix of Eq. (2) contains a part which is proportional to the operator I_z commuting with the DDI Hamiltonian (9). The stationary MQ NMR coherence of the zeroth order in the high temperature approximation [11] is described by the density matrix aI_z, wherein the parameter a can be found from the conservation law ($\langle I_z \rangle = \text{const}$):

$$\mathrm{Tr}[\sigma_0(\tau) I_z] = a\,\mathrm{Tr}(I_z^2). \tag{10}$$

A simple calculation with Eqs. (2,5,6) yields in the limit $N \to \infty$ [13]

$$a = J_0^2(2D\tau). \tag{11}$$

Taking into account that the experimental data were chosen equal to one at $t = 0$ in the experimental conditions one can find the stationary intensity of the MQ NMR coherence of the zeroth order F_0^{st}:

$$F_0^{st} = \frac{J_0^2(2D\tau)}{G_0(\tau)} = \frac{2J_0^2(2D\tau)}{1 + J_0(4D\tau)}. \tag{12}$$

The experimental dependence of the stationary intensity of the MQ NMR coherence of the zeroth order on the duration of the preparation period is presented in fig.3. One can see a satisfactory agreement of the theoretical predictions with the experimental data.

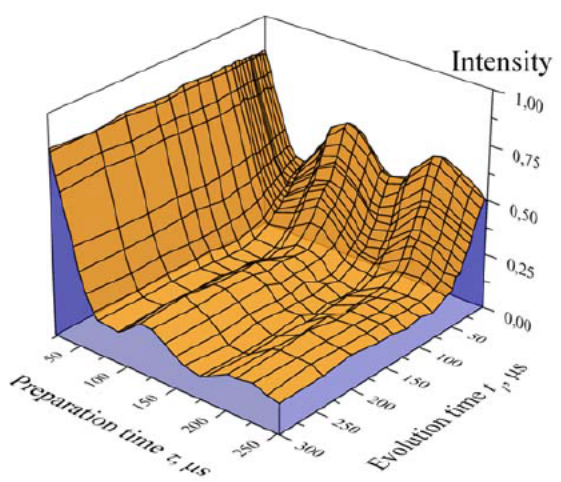

Fig.2. Intensities of the MQ coherence of zeroth order depending on lengths of the preparation and evolution periods. The external magnetic field is directed along the chain.

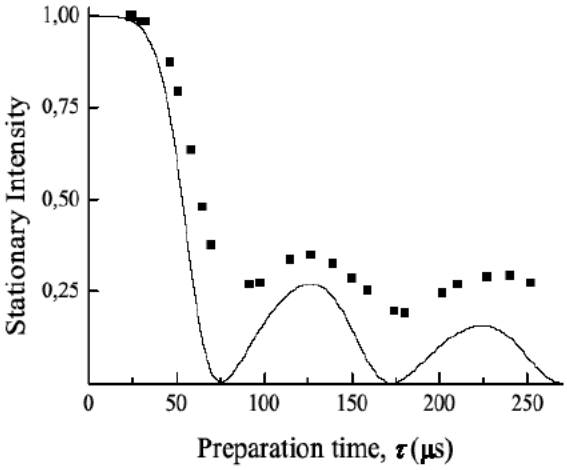

Fig.3. Stationary intensity of the MQ NMR coherence of the zeroth order on the evolution period versus the duration τ of the preparation period. The solid line is the theoretical curve of Eq. (12)

4. Relaxation of the MQ NMR coherence of order two

An investigation of the relaxation process with the DDI Hamiltonian of Eq. (9) is too complicated. However, the problem is substantially simplified if we restrict ourselves to the ZZ part of H_{dz} only and consider the Hamiltonian

$$H_{zz} = 2\sum_{i<j} D_{ij} I_i^z I_j^z = \sum_{i \neq j} D_{ij} I_i^z I_j^z \,. \tag{13}$$

We will refer to the problem with Hamiltonian H_{zz} as the ZZ model [13]. The intensity $F_{\pm 2}(\tau, t)$ of the MQ NMR coherence of the plus/minus second orders in the course of the evolution period at time instant t is

$$F_{\pm 2}(\tau, t) = \frac{\mathrm{Tr}\left[e^{-iH_{zz}t} \sigma_{\pm 2}(t) e^{iH_{zz}t} \sigma_{\mp 2}(t) \right]}{\mathrm{Tr}(I_z^2)} \,. \tag{14}$$

Using Eqs. (3-6) and the commutation properties of the spin operators [11] one can obtain

$$F_{\pm 2}(\tau, t) = \frac{1}{8N} \sum_{m,m'} \prod_{n \neq (m,m')} \cos[(D_{nm} + D_{nm'})t] \cdot [1 - (-1)^{m-m'}]^2 J_{m-m'}^2 (2D\tau) \tag{15}$$

One can find from fig.4 that the decay of the MQ NMR coherence of the second order conforms reasonably well to a Gaussian function $S(t) = \exp(-M_2(\tau) t^2 / 2)$, where the second moment $M_2(\tau)$ of the line shape of this coherence is

$$M_2(\tau) = -\frac{1}{G_2(\tau)} \frac{d^2 F_2(\tau, t)}{dt^2} \bigg|_{t=0} \tag{16}$$

In fig.5, the dependencies of the experimental and theoretical dipolar relaxation times on the duration of the preparation period are shown. These data were obtained from fig.4 as the times t_e when the intensities of the MQ NMR coherences of the second order decrease by a factor of e, i.e. $t_e = \sqrt{2 / M_2(\tau)}$ .One can see that the theoretical predictions satisfactorily describe the experimental dependencies.

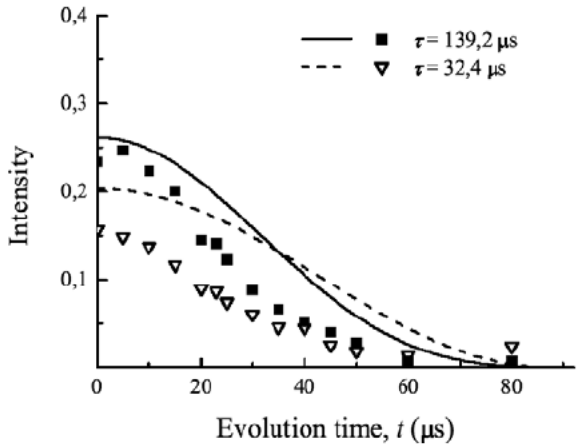

Fig.4. The experimental intensities of the MQ NMR coherence of the second order on the evolution period t at different durations of the preparation period τ. Solid lines are theoretical curves of Eq. (15) with N=150

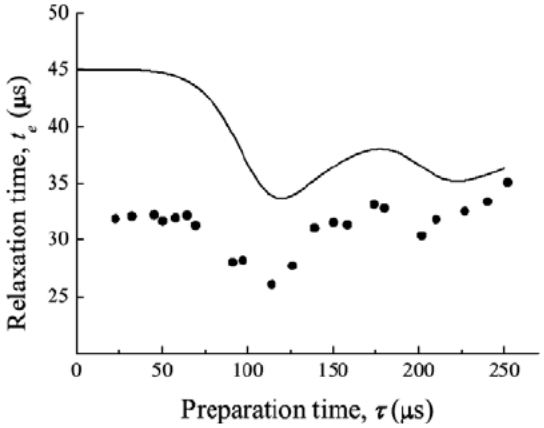

Fig.5. The experimental times of the dipolar relaxation of the MQ NMR coherence of the second order versus the duration of the preparation period τ. Solid lines are the theoretical times t_e of the dipolar relaxation obtained as $t_e = \sqrt{2/M_2(t)}$, where the second moment

$$M_2(t) = -\frac{1}{G_2(\tau)} \frac{d^2 F(\tau,t)}{dt^2}\bigg|_{t=0}$$

The flip-flop part of the DDI was neglected in the developed ZZ model of relaxation of the MQ coherences of the plus/minus second orders. This is one of the possible sources of the discrepancy between the theoretical predictions and the experimental results. The other sources are various kinds of experimental imperfections, the DDI with spins of surrounding chains and heteronuclear interactions.

5. Conclusions

We studied theoretically and experimentally the relaxation of the MQ NMR coherences of orders zero and two in the MQ NMR experiment [1]. The experimental investigation of the dipolar relaxation of the MQ NMR coherences was performed on the quasi-one-dimensional chains of ^{19}F nuclear spins in calcium fluorapatite. We have shown that the intensity of the MQ NMR coherence of the zeroth order does not decay completely in the relaxation process. The calculated stationary value of the intensity of the MQ NMR coherence of the zeroth order agrees with the experimental data.

Relaxation of the MQ NMR coherences of orders tow and minus two was investigated in the ZZ model. A satisfactory agreement between the developed theory and the experimental data was obtained.

The work is supported by the Russian Foundation for Basic Research (grants No. 16-03-00056 and No. 16-33-00867) and the Program of the Presidium of RAS No.1.26 “Electron Spin Resonance, Spin-Dependent Electron Effects and Spin Technologies”.

References

[1] J.Baum, M.Munoviz, A.N.Garroway, A.Pines, J.Chem.Phys.**83**, 2015 (1985).

[2] M.A.Nielsen, I.L.Chuang. Quantum Computation and Quantum Information, Cambridge University Press, Cambridge (200).

[3] P.Cappellaro, C.Ramanathan, D.G.Cory, Phys.Rev.Lett **99**, 250506 (2007).

[4] G.Kaur, A.Ajoy, P.Cappellaro, New J.Phys.**15**, 093035 (2013).

[5] E.B.Fel'dman, S.Lacelle, Chem.Phys.Lett. **253**, 27 (1996)

[6] E.B.Fel'dman, S.Lacelle, J.Chem.Phys. **107**, 7067 (1997)

[7] S.I.Doronin, I.I.Maksimov, E.B.Fel'dman, J.Exp.Theor.Phys. **91**, 597 (2000)

[8] E.B.Fel'dman, Appl.Magn.Reson. **45**,797 (2014)

[9] S.I.Doronin, E.B.Fel'dman, I.I.Maksimov, J.Magn.Reson. **171**, 37 (2004)

[10] D.C.Matts. The Many Body problem: An Encyclopedia of Exactly Solved Models in One Dimension. World Scientific, Singapore (1993)

[11] M.Goldman. Spin Temperature and Nuclear Magnetic Resonance in Solids. Clarendon, Oxford (1970)

[12] P.Jordan, E.Wigner, Z.Phys. **47**, 631 (1928)

[13] G.A.Bochkin, E.B.Fel'dman, S.G.Vasil'ev, Z.Phys.Chen. **230** (2016).

Experimental vs GIAO calculated NMR spectra for 5,8-dihydro-4*H*-pyrazolo[5,1-*d*][1,2,5]triazepin-4-ones

S.I. Serobaba, V.Yu. Popov, A.Yu. Popov, E.V. Raksha, A.B. Eresko

L.M. Litvinenko Institute of Physical Organic and Coal Chemistry, 83114, Universitetskaya str., 24, Donetsk

e-mail: a_eresko2002@yahoo.com

Abstract

Several derivatives of new heterocyclic system – pyrazolo[1,2,5]triazepinones have been prepared. GIAO-calculated NMR chemical shifts (^{1}H and ^{13}C) as well as experimental solution data are reported for the obtained new compounds.

Keywords: heterocycles, pyrazolo[1,2,5]triazepinones, NMR ^{1}H and ^{13}C, chemical shift, magnetic shielding constant, GIAO.

Introduction

The benzodiazepinone scaffold is an extremely rewarding template for drug discovery. Biological activity of compounds bearing a 1-aryl-2,3-benzodiazepine skeleton is best demonstrated by tofisopam, a well-known anxiolytic drug from this family [1], or the former drug candidate talampanel [2, 3], that reached the human clinical development stage. The structurally related 1-aryl-2,3-benzodiazepine-4-ones were also exhaustively investigated as non-competitive AMPA receptor antagonists with marked anticonvulsant activity [4, 5]. Related fused heterocyclic systems, such as pyrazolo[1,2,5]triazepines, can therefore be regarded as potentially useful scaffolds for drug discovery. In this work we report the results of molecular modeling of structure and NMR shieldings for derivatives of a new class of compounds, pyrazolo[1,2,5]triazepines.

Results and discussions

Our planned approach to pyrazolo[1,2,5]triazepinones **3** involved cyclization of pyrazole derivatives **2**, synthesized by the reaction of 3-R-1*H*-pyrazole-5-carboxylate **1** having an NH moiety with 2-bromo-1-phenylethanone. Heating of alkylated pyrazole derivatives **2** with hydrazine monohydrate in ethylene glycol monoethyl ether at reflux temperature produced the desired cyclization products **3**, which were isolated in good yields (61−73%) after purification. The structures were determined by NMR spectral data.

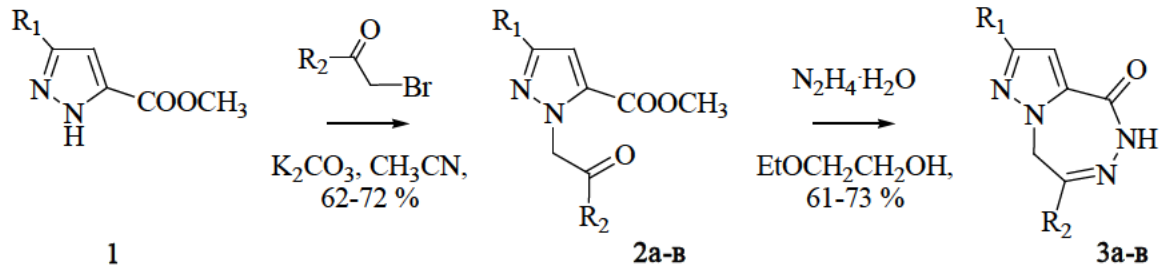

1 **2a-в** **3a-в**

The equilibrium structures of the most stable pyrazolo[1,2,5]triazepinones conformers are shown on fig.1.

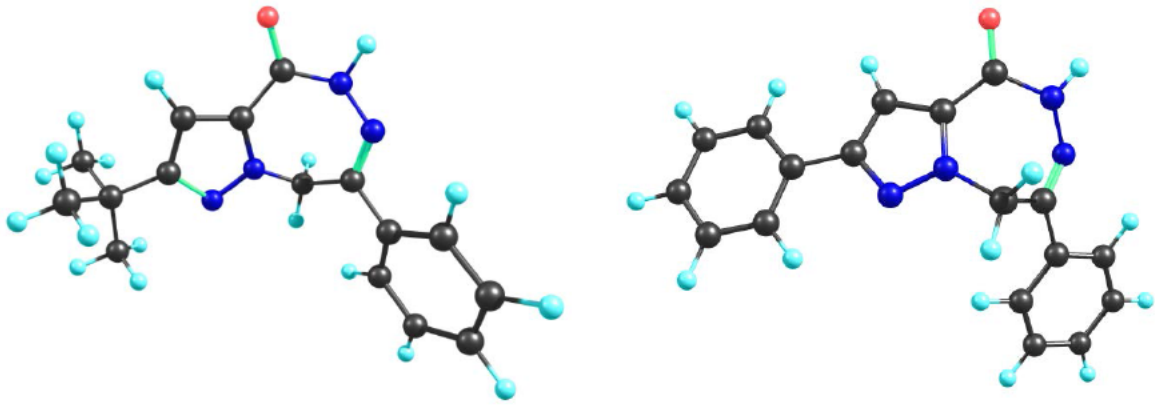

3a **3b**

Fig.1. The equilibrium configurations of the pyrazolo[1,2,5]triazepines **3a,b**

For the most stable conformers of pyrazolo[1,2,5]triazepinones molecules ^{1}H and ^{13}C chemical shifts were estimated. The B3LYP/6-31G(d,p) optimized geometries were used for magnetic shielding tensors calculation by standard GIAO method. Concerning the spectral patterns of protons and carbons, inspection of calculated and experimental values reveals the following features. The patterns of ^{1}H and ^{13}C spectra for pyrazolo[1,2,5]triazepinones are correctly reproduced at used computational level. A linear correlation between the theoretical and experimental carbon and proton chemical shifts is clearly visible in fig.2.

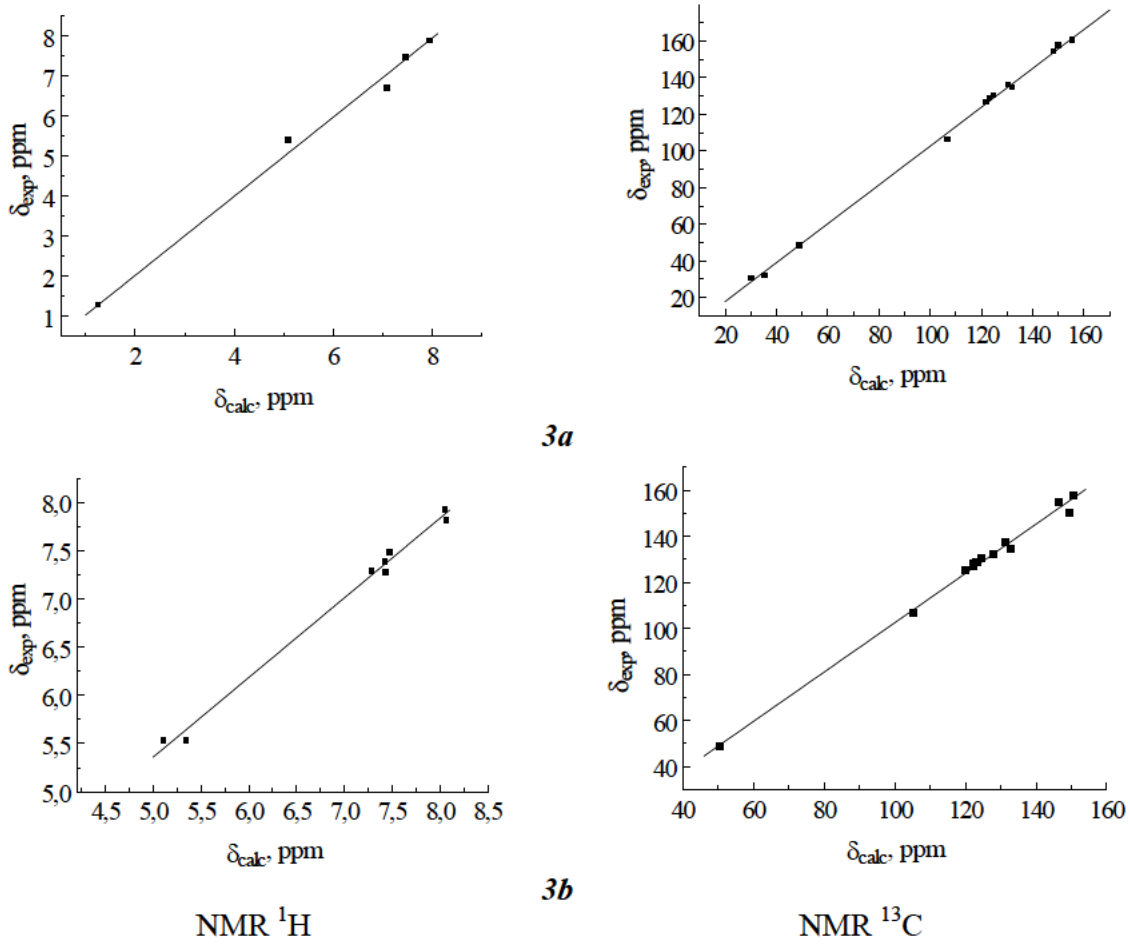

Fig.2. Linear correlation between the theoretical and experimental carbon and proton chemical shifts of pyrazolo[1,2,5]triazepinones

The following correlations were obtained:

3a ^{1}H: $\delta_{exp} = (0.989 \pm 0.012)\cdot\delta_{calc} + (0.04 \pm 0.06)$, R = 0,99884;
^{13}C: $\delta_{exp} = (1.061 \pm 0.009)\cdot\delta_{calc} - (3.52 \pm 1.06)$, R = 0,99944;
3b ^{1}H: $\delta_{exp} = (0.826 \pm 0.012)\cdot\delta_{calc} + (1.23 \pm 0.023)$, R = 0,99579;
^{13}C: $\delta_{exp} = (1.072 \pm 0.022)\cdot\delta_{calc} - (4.7 \pm 2.8)$, R = 0,99648.

Good quantitative agreement within 0.5 – 7.9 ppm for the carbons and within 0.003 – 0.4 ppm for the protons is observed of these compounds, which appears to be very satisfactory, taking into consideration the fact that the experimental chemical shifts in solution are subject to solvent, concentration and temperature effects.

Experimental

^{1}H NMR spectra were recorded on a Bruker DRX 400 (400 MHz) in DMSO-d_6 with TMS as an internal standard. The CHN elemental analysis was performed using a Fisons AE1108 analyzer, and the results were found to be in good agreement (±0.25%) with the calculated values.

2-Tert-butyl-7-phenyl-5,8-dihydro-4H-pyrazolo[5,1-d][1,2,5]triazepin-4-one **3a**

A solution of derivative **2a** (1.5 g; 0.005 mol), 80% aqueous hydrazine (0.015 mol) in ethylene glycol monoethyl ether (10 ml) was heated at reflux with stirring for 5 hours. The reaction mixture was then evaporated to dryness, and the residue was recrystallized from a 2-propanol to afford compound **3a**. Yield: 0.86 g 61%; M.p.: 240-242 ºC; ^{1}H NMR (400 MHz, DMSO-d_6): δ = 1.27 (9H, s, $C(CH_3)_3$), 5.38 (2H, s, CH_2), 6.68 (1H, s, H-3), 7.45 (3H, sbr, H-3',4',5'), 7.88 (2H, sbr, H-2',6'), 7.57 (2H, t, *J* = 8.0 Hz, H-3'',5''),7.68 (1H, t, *J* = 8.0 Hz, H-4''), 7.82 (2H, d, *J* = 8.0 Hz, H-2',6'), 11.26 (1H, s, NH) ppm; ^{13}C NMR (100 MHz, DMSO-d_6): δ = 30.2 (3C), 31.7, 48.2, 105.9, 126.5 (2C), 128.5 (2C), 130.1, 134.4, 135.8, 154.1, 157.6, 160.5 ppm; Anal. Calcd. for: $C_{16}H_{18}N_4O$: C, 68.06; H, 6.43; N, 19.84; O, 5.67; Found: C, 68.15; H, 6.42; N, 19.77.

2,7-Diphenyl-5,8-dihydro-4H-pyrazolo[5,1-d][1,2,5]triazepin-4-one **3b**

A solution of derivative **2b** (1.6 g; 0.005 mol), 80% aqueous hydrazine (0.015 mol) in ethylene glycol monoethyl ether (10 ml) was heated at reflux with stirring for 7 hours. The reaction mixture was then evaporated to dryness, and the residue was recrystallized from a methanol to afford compound **3b**.Yield: 1.1 g 73%; M.p.: 215-217 ºC; ^{1}H NMR (400 MHz, DMSO-d_6): δ = 5.53 (2H, s, CH_2), 7.27 (1H, sbr, H-3), 7.29 (1H, t, *J* = 8.0 Hz, H-4'), 7.38 (2H, t, *J* = 8.0 Hz, H-3',5'), 7.48 (3H, sbr, H-3'',4'',5''), 7.81 (2H, d, *J* = 8.0 Hz, H-2',6'), 7.92 (2H, sbr, H-2'',6''), 11.43 (1H, s, NH) ppm; ^{13}C NMR (100 MHz, DMSO-d_6): δ = 48.5, 106.6, 125.1 (2C), 126.6 (2C), 127.7, 128.3 (2C), 128.5 (2C), 130.2, 131.9, 134.3, 137.1, 150.0, 154.5, 157.4 ppm; Anal. Calcd. for: $C_{18}H_{14}N_4O$: C, 71.51; H, 4.67; N, 18.53; O, 5.29; Found: C, 71.59; H, 4.73; N, 18.64.

Initial molecular geometry of the pyrazolo[1,2,5]triazepines was generated using the algorithm of complete inclusion of possible geometric and steric factors implemented in the Conformer plugin of the Marvin software package [6]. Molecular geometry and electronic structure parameters, thermodynamic characteristics of the pyrazolo[1,2,5]triazepines were calculated using the Gaussian 09 [7] software package. Geometric parameters, harmonic vibrational frequencies, and the vibrational contribution to the zero-point vibrational energy were determined after full geometry optimization in the framework of B3LYP/6-31G(d,p) density functional calculations. The magnetic shielding tensors (χ, ppm) for ^{1}H and ^{13}C nuclei of the triazepine derivatives were calculated with the B3LYP/6-31G(d,p) optimized geometries by standard GIAO (Gauge-Independent Atomic Orbital) approach [8]. The

calculated magnetic isotropic shielding tensors, χ_i, were transformed to chemical shifts relative to TMS, δ_i, by $\delta_i = \chi_{ref} - \chi_i$, where both, χ_{ref} and χ_i, were taken from calculations at the same computational level. χ Values for magnetically equivalent nuclei were averaged.

Conclusions

Correlations between experimental chemical shifts and GIAO-calculated isotropic shielding constants of protons and carbons as obtained from four new 2-R-7-phenyl-5,8-dihydro-4*H*-pyrazolo[5,1-*d*][1,2,5]triazepin-4-ones were established in order to assess the performance of NMR spectral calculations. The B3LYP method with the 6 – 31 G(d,p) basis set was considered for geometry optimization and spectral calculations. Linear regressions $\delta_{calc} = a\delta_{exp} + b$ yield standard deviations of 1.09 – 4.71 ppm for hydrogen and carbon atoms.

References

[1] Körösi, J.; Láng, T.; Komlós, E.; Erdélyi, L. HU 155572 Hung. Pat.; Chem. Abstr. 1969, 70, 115026.

[2] Luszczki, J.J. Third-generation antiepileptic drugs: mechanisms of action, pharmaco-kinetics and interactions. *Pharmacol. Rep.* **2009**, *61*, 197–216.

[3] Iwamoto, F. M.; Kreisl, T. N.; Kim, L.; Duic, J. P.; Butman, J. A.; Albert, P. S.; Fine, H. A. Phase 2 trial of talampanel, a glutamate receptor inhibitor, for adults with recurrent malignant gliomas. *Cancer* **2010**, *116*, 1776–1782.

[4] Zappala, M.; Postorino, G.; Micale, N.; Caccamese, S.; Parrinello, N.; Grazioso, G.; Roda, G.; Menniti, F. S.; De Sarro, G.; Grasso, S. Synthesis, Chiral Resolution, and Enantiopharmacology of a Potent 2,3-Benzodiazepine Derivative as Noncompetitive AMPA Receptor Antagonist *J. Med. Chem.* **2006**, *49*, 575–581

[5] Grasso, S.; De Sarro, G.; De Sarro, A.; Micale, N.; Polimeni, S.; Zappala, M.; Puia, G.; Baraldi, M.; De Micheli, C. Synthesis and anticonvulsant activity of novel and potent 1-aryl-7,8-methylenedioxy-1,2,3,5-tetrahydro-4*H*-2,3-benzodiazepin-4-ones. *Bioorg. Med. Chem. Lett.* **2001**, *11*, 463–466.

[6] Marvin 5.10.4, ChemAxon, Calculator Plugins, **2014**, http://www.chemaxon.com/.

[7] Gaussian 09, Revision B.01, M. J. Frisch, G. W. Trucks, H. B. Schlegel, G. E. Scuseria, M. A. Robb, J. R. Cheeseman, G. Scalmani, V. Barone, B. Mennucci, G. A. Petersson, H. Nakatsuji, M. Caricato, X. Li, H. P. Hratchian, A. F. Izmaylov, J. Bloino, G. Zheng, J. L. Sonnenberg, M. Hada, M. Ehara, K. Toyota, R. Fukuda, J. Hasegawa, M. Ishida, T. Nakajima, Y. Honda, O. Kitao, H. Nakai, T. Vreven, J. A. Montgomery, Jr., J. E. Peralta, F. Ogliaro, M. Bearpark, J. J. Heyd, E. Brothers, K. N. Kudin, V. N. Staroverov, T. Keith, R. Kobayashi, J. Normand, K. Raghavachari, A. Rendell, J. C. Burant, S. S. Iyengar, J. Tomasi, M. Cossi, N. Rega, J. M. Millam, M. Klene, J. E. Knox, J. B. Cross, V. Bakken, C. Adamo, J. Jaramillo, R. Gomperts, R. E. Stratmann, O. Yazyev, A. J. Austin, R. Cammi, C. Pomelli, J. W. Ochterski, R. L. Martin, K. Morokuma, V. G. Zakrzewski, G. A. Voth, P. Salvador, J. J. Dannenberg, S. Dapprich, A. D. Daniels, O. Farkas, J. B. Foresman, J. V. Ortiz, J. Cioslowski, and D. J. Fox, Gaussian, Inc., Wallingford CT, 2010.

[8] K. Wolinski, J.F. Hilton, P. Pulay. Efficient implementation of the gauge-independent atomic orbital method for NMR chemical shift calculations. *J. Am. Chem. Soc*. 112 (1990) 8251-8260.

Ab initio study of single-crystalline $BiMnO_3$

D. Nazipov[1], A. Nikiforov[1], L. Gonchar[1,2]

[1]Ural Federal University, 19 Mira St., Ekaterinburg, Russia

[2]Ural State University of Railway Transport, 66 Kolmogorov St., Ekaterinburg, Russia

e-mail: qwear0@gmail.com

Multiferroics are actively studied and have a wide practical application. The effect of ferroelectricity and at the same time long-range magnetic order in multiferroic opens the possibility of creation of electronic devices with controllable magnetic characteristics. At the present time being searched for multiferoics combining magnetic and ferroelectric properties. Among the materials, perovskite-like $BiMnO_3$ has attracted particular attention of researchers. Complicated orbital structure [1,2] on Mn^{3+} ions leads to ferromagnetic ordering below T_c=100K and existence of lone pair of $6s^2$ electrons of Bi^{3+} may lead to ferroelectric effect. Thus, a detailed analysis of the microscopic mechanisms of interaction between the magnetic and crystal subsystems is required.

In this paper we present the results of ab initio calculations of the crystal structure parameters and the phonon spectrum of $BiMnO_3$. Lattice constants, coordinates of ions in cell and bond lengths have been obtained for the ferromagnetic C2/c phase in a good agreement with experiment [3]. Calculated frequencies and intensities of the active modes in IR (figure 1) have been compared with the experiment [4].

The magnetic moments of Mn^{3+} ions are obtained from first principles. Charge density maps have been drawn to investigate a charge distribution around Bi^{3+} ions. Figure 2 shows a localization of negative charge near Bi^{3+} ion and a formation of the dipole moment. It has been found that the arrangement of the dipole moments corresponds to antiferroelectric ordering.

Calculations have been performed in solid state calculations package *CRYSTAL14* [5] in the framework of MO LCAO approximation, using density functional theory method with hybrid DFT/HF functionals. The ions are described by full-electron Gauss-type basis sets and pseudopotential for Bi^{3+}.

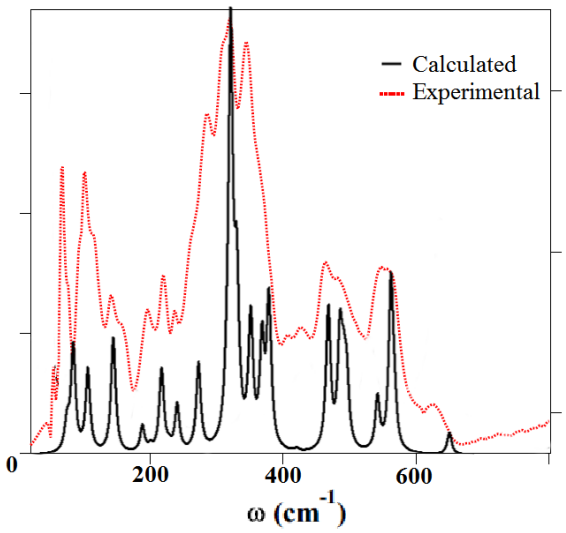

Fig.1. Calculated and experimental (T = 10 K) infrared spectrum

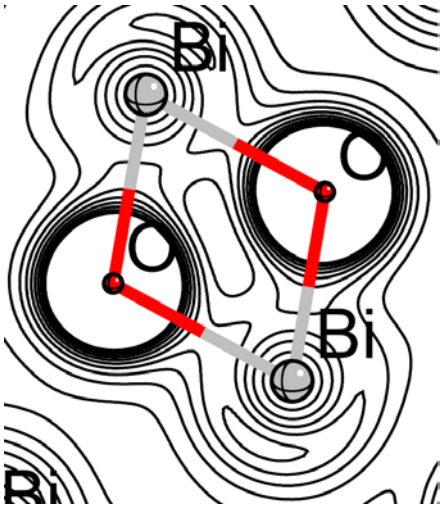

Fig.2. Charge density map in plane of two Bi^{3+} ions

References

[1] A.M. dos Santos, A.K. Cheetham, T. Atou, Y. Syono, Y. Yamaguchi, K. Ohoyama, H. Chiba, C.N.R. Rao, Phys. Rev. B **66,** 064425 (2002).

[2] L.E. Gonchar, A.E. Nikiforov, Phys. Rev. B **88**, 094401 (2013).

[3] A.A. Belik, S. Likubo, T. Yokosawa, K. Kodama, N. Igawa, S. Shamoto, M. Azuma, M. Takano, K. Kimoto, Y. Matsui, E. Takayama-Muromachi, J. Am. Chem. Soc. **129**, 971 (2007).

[4] W. S. Mohamed, A. Nucara, G. Calestani, F. Mezzadri, E. Gilioli, F. Capitani, P. Postorino, P. Calvani, Phys. Rev. B **92**, 054306 (2015).

[5] URL: http://www.crystal.unito.it/index.php

The long-range magnetic order in shattuckite $Cu_5(OH)_2(SiO_3)_4$

A.V. Koshelev[1], A.N. Vasiliev[1], O.S. Volkova[1], E.A. Zvereva[1], D.A. Chareev[2].

[1]Lomonosov Moscow State University, 119991, Leninskie Gory, Moscow, Russia
[2]Institute of Experimental Mineralogy, 142432, Academica Osypyana, Chernogolovka, Russia

e-mail: anatolkosh@mail.ru

The sample of shattukite $Cu_5(SiO_3)_4(OH)_2$ was purchased from the stone shop, its origin was claimed to be Kaokoveld Plateau, Namibia. The X-rays diffraction pattern of natural shattuckite reveals a high purity of the sample with only trace amounts of secondary phases of clinozoisite $Ca_2Al_2(Si_2O_7)(SiO_4)O(OH)$ and tentatively ankerite $Ca(Mg,Mn,Fe)(CO_3)_2$. The piece of blue colored shattuckite of about 100 mg in weight was grinded in agate mortar into fine powder, pressed into pellets and investigated through measurements of magnetization, specific heat and electron spin resonance.

In orthorhombic crystal structure of shattuckite $Cu_5(SiO_3)_4(OH)_2$ [1], shown in fig.1, the apices of the silicate tetrahedra are condensed on both sides of an extended copper-oxygen layer CuO_2. The oxygen sites in this brucite-like layer [2] that are not supplied by SiO_4 tetrahedra are occupied by OH groups. The CuO_2 layer is strongly bent at the region of contact of adjacent silicate chains, giving the layers, which lie parallel to the *ac*-plane, a corrugated aspect. The triple layers stack against each other along the *b* axis with their corrugations nested. These layers are linked together by additional copper atoms which are bonded to the outer unshared oxygen atoms of the silicate chains from adjacent triple layers to form square planar CuO_4 plaquettes that are joined in twisted CuO_2 ribbons parallel to the *c* axis.

Electron spin resonance

The X-band ESR spectra for a powder sample of shattuckite $Cu_5(OH)_2(SiO_3)_4$ were recorded in the paramagnetic phase from room temperature down to 8 K. At lower temperature the rapid signal fading occurs due to onset of long-range magnetic ordering and subsequent opening of the gap for resonance excitations. The representative example is given in fig.2. The ESR powder pattern is characteristic of Cu^{2+} ions with anisotropic *g*-tensor over the whole temperature range studied. For estimation of the parallel $g_{||}$ and perpendicular $g_{\perp}$ the lineshape was analyzed by sum of standard Lorenzian functions as shown in fig.2. Both principal components of g-tensor remain almost temperature independent over the whole range investigated and are on average $g_{||} = 2.19 \pm 0.01$ and $g_{\perp} = 2.07 \pm 0.01$ resulting in $g_{av} = 2.11 \pm 0.01$ corresponding to the stabilization of Cu^{2+} ions in distorted square coordination [3] being in agreement with earlier reported values for shattuckite [4]. At low temperatures, the partially resolved hyperfine structure was also visible in the spectrum. Since both stable copper isotopes ^{63}Cu (natural abundance 69.09%) and ^{65}Cu (natural abundance 30.91%) have non-zero nuclear magnetic moment $I = 3/2$, one can expect four hyperfine components ($N_{hf} = 2I + 1$) in ESR spectrum due to interaction between the electron magnetic moment of unfilled electron *d*-shell of Cu^{2+} ions and nuclear magnetic moment of ^{63}Cu and ^{65}Cu isotopes. Indeed, at 8 K two sets of four lines superimposed over a broad anisotropic central line for the parallel and perpendicular principal components of *g*-tensor may be identified. The hyperfine-interaction constants were estimated to be about $^{63,65}A_{||} \approx 399$ MHz and $^{63,65}A_{\perp} \approx 96$ MHz, respectively.

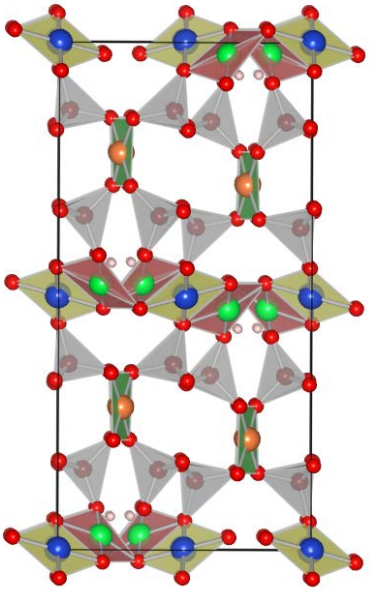

Fig.1. The polyhedral representation of the crystal structure of $Cu_5(SiO_3)_4(OH)_2$ along the c axis.

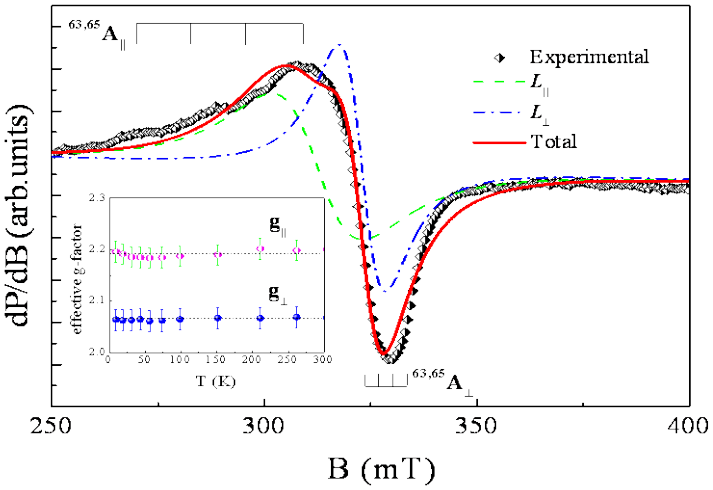

Fig.2. ESR spectrum of $Cu_5(SiO_3)_4(OH)_2$ at 8 K: experimental data are shown by circles, their analysis in accordance with sum of two Lorentzian profiles are shown by lines, dashed and dash-dotted lines represent two resolved components and solid line is their sum. The inset represents the temperature dependences of principal values of *g*-tensor.

Thermodynamics

The temperature dependences of reduced magnetization $\chi = M/B$ taken at various magnetic fields in $Cu_5(SiO_3)_4(OH)_2$ are shown in fig.3. In a wide temperature range, this quantity is almost field-independent, but it is quite sensitive to magnetic field at low temperatures. The field dependences of magnetization taken at various temperatures are shown in the upper inset to fig.3. The hysteretic behavior in magnetization appears sharply at low temperatures, cf. curves taken at 6 and 8 K. At 2 K, the value of spontaneous magnetization constitutes about 0.075 μ_B/f.u., i.e. about 1.4×10^{-2} of magnetization saturation. At higher fields, the *M* vs. *B* curve is essentially linear which is typical for antiferromagnets with large values of exchange interaction parameters. No signature for a spin-flop transition was evidenced up to 9 T.

In paramagnetic state, the temperature dependence of reduced magnetization taken at 0.1 T in $Cu_5(SiO_3)_4(OH)_2$ can be approximated by the Curie-Weiss law $\chi = \chi_0 + C/(T - \Theta)$ with addition of the temperature independent term. The fitting in the temperature range 150 – 300 K gives $\chi_0 = 6.5\times10^{-5}$ emu/mol, the Curie constant $C = ng^2\mu_B^2S(S + 1) = 2.23$ emu·K/mol, and the Weiss temperature $\Theta = -13.5$ K. The value of the Curie constant somewhat exceeds that expected for number of Cu^{2+} ions ($n = 5$) in the formula unit of shattuckite and averaged *g*-factor of copper g_{av} determined in ESR measurements. The negative sign of Θ indicates the predominance of antiferromagnetic exchange interactions at elevated temperatures. The sign and value of the temperature independent term χ_0 reflect the competition between diamagnetic Pascal contribution $\chi_{dia} = -2.23\times10^{-4}$ emu/mol and paramagnetic van Vleck contribution $\chi_{vV} = 2.74\times10^{-4}$ emu/mol.

At lowering temperature, the experimental data deviates downward from the extrapolation of the fitting curve signaling further strengthening of antiferromagnetic interactions contribution. Most clearly it is seen in the C vs. T dependence shown in the lower

inset to fig.3. This representation of experimental data is most suitable for low-dimensional low-spin magnetic systems where the presence of temperature independent term can significantly distort the temperature dependence of inverse magnetic susceptibility. At $T_N = 7$ K, the temperature dependence of reduced magnetization M/B exhibits either sharp upturn at $B = 0.1$ T or rounded maximum at $B = 9$ T. These features signal the transition into long-range antiferromagnetic state with finite spontaneous magnetization.

The transition into long-range ordered state in $Cu_5(SiO_3)_4(OH)_2$ was further confirmed in the measurements of specific heat C_p. As shown in fig.4, the C_p vs. T dependence taken at $B = 0$ T exhibits the rounded maximum at $T_N = 7$ K. The application of magnetic field $B = 9$ T smears and shifts the anomaly to higher temperatures. This is a signature of the presence of spontaneous magnetization in the ordered phase of shattuckite. Such a behavior is typical for ferromagnets since larger fields develop magnetization already well above the zero field T_N and the magnetization does not arise spontaneously below a critical temperature anymore [5]. The magnetic entropy released below $T_N = 7$ K in $Cu_5(SiO_3)_4(OH)_2$ constitutes less than one third of the expected value $S_{mag} = 5R \ln 2$. This observation is in correspondence with the temperature dependence of the Curie constant in shattuckite which exhibits pronounced deviation from the Curie-Weiss law already below ~ 150 K. It means that the significant part of magnetic entropy is released at elevated temperatures. In the absence of non-magnetic counterpart of the title compound it is difficult to separate phonon and magnon contributions to specific heat at low temperatures. The temperature dependence of the total entropy in $Cu_5(SiO_3)_4(OH)_2$ is shown in fig.4. At $T < T_N$, it represents basically the magnetic entropy since the lattice contribution in this temperature range is usually negligible [6].

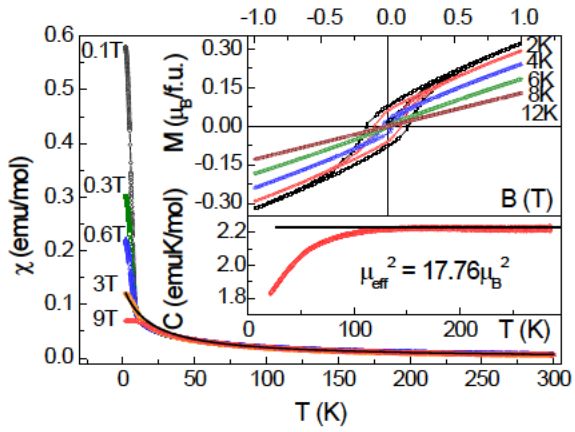

Fig.3. The temperature dependences of reduced magnetization $\chi = M/B$ taken at various magnetic fields in $Cu_5(SiO_3)_4(OH)_2$. The lower inset represents the temperature dependence of the Curie constant $C = (\chi - \chi_0)(T - \Theta)$ at $B = 0.1$ T; the upper inset represents the hysteresis loops taken at various temperatures.

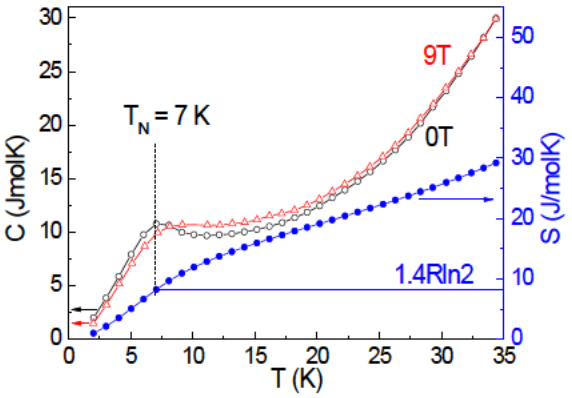

Fig.4. The temperature dependences of the specific heat in $Cu_5(SiO_3)_4(OH)_2$ at $B = 0$ (circles) and $B = 9$ T (triangles), the temperature dependence of the entropy at $B = 0$ (right axis).

References

[1] Ewans HT, Mrose Jr and ME (1977) The crystal chemistry of the hydrous copper silicates, shattuckite and plancheite. Am. Mineral. 62:491.

[2] Mara RT and Sutherland GBBM (1956) Crystal Structure of Brucite and Portlandite in Relation to Infrared Absorption. J. Opt. Soc. Amer. 6:464.

[3] Krishna RM and Gupta SK (1994) Electron Paramagnetic Resonance Investigations of the Cu^{2+} ion in a Variety of Host Lattices-A Review. Bull. Magn. Resonance, 16:239.

[4] Sarma KBN, Reddy BJ and Lakshman SVJ (1982) Absorption spectra of Cu^{2+} in shattuckite and plancheite , Phys. Lett. 92A:305.

[5] Falkowski M, Reiffers M, Zapotokova M, Kowalczyk A, Tolinski T and Gazo E (2009) Heat capacity studies of NdNi4Si compound. Acta Physica Polonica A 115:126.

[6] Tari A (2003), The specific heat of matter at low temperatures. Imperial College Press, 348 p.

Antiferromagnetic resonance in noncollinear antiferromagnet $Mn_3Al_2Ge_3O_{12}$

Y.V. Krasnikova[1], V.N. Glazkov[1,2], T.A. Soldatov[1,2]

[1]P.L. Kapitza Institute for Physical Problems RAS, 119334, Kosygin str. 2, Moscow, Russia
[2]Moscow Institute of Physics and Technology, 141700, Dolgoprudny, Russia

e-mail:krasnikova.mipt@gmail.com

Manganese garnet $Mn_3Al_2Ge_3O_{12}$ demonstrates unusual magnetic order at low temperatures, its ions form 12 noncollinear sublattices (fig.1). Antiferromagnetic resonance (AFMR) of garnet species has been studied before [1]. Recently, a non-linear NMR absorption was observed in this magnet, which was attributed to antiferromagnetic domain walls oscillations [2].

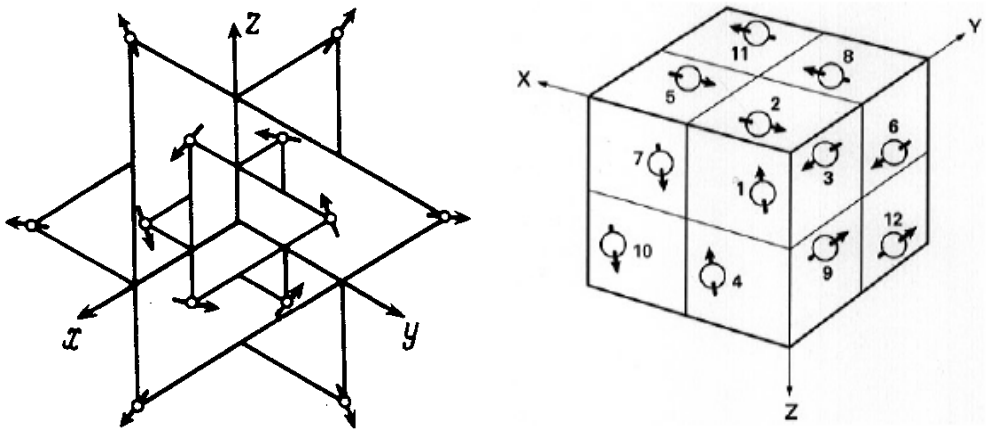

Fig.1. Scheme of 12-sublattice order of Mn magnetic moments in $Mn_3Al_2Ge_3O_{12}$. There are 12 magnetic ions in primitive cell [1,2].

We have measured frequency-field dependence of AFMR for manganese garnet in wide range of frequencies (5 – 143 GHz) in different orientations (fig.2). Our measurements complement earlier studies of AFMR in this compound [1]. We have observed three modes of oscillations. Spectrum has two gaps: 40 and 70 GHz at temperature 1.7 K. Spin-reorientation transition took place at H ∥ [100] at the field about 20 kOe. One of the AFMR modes is expected to soften at this transition [1]. On the other hand, manganese NMR frequency is about 600 MHz at zero field [3], thus NMR mode will cross softening AFMR mode in the transition field vicinity. This crossing usually results in the formation of collective electron-nuclear modes of precession and repulsion of AFMR and NMR precession modes. We observed AFMR signal at the spin reorientation field down to 4.5GHz. This observation allows an upper estimate of the modes repulsion effect.

To describe frequency-field dependence we have used Andreev-Marchenko theory [1,4]. We have modeled numerically frequency-field dependences using an algorithm described in [5]. We have found that experimental data can be fully described by this theoretical approach.

Also we have observed hysteresis of microwave absorption at low fields near gap frequencies. This hysteresis could be connected with domain structure of the magnet. Domain structure of manganese garnet was reported before [6]. According to [1] magnetic structure of

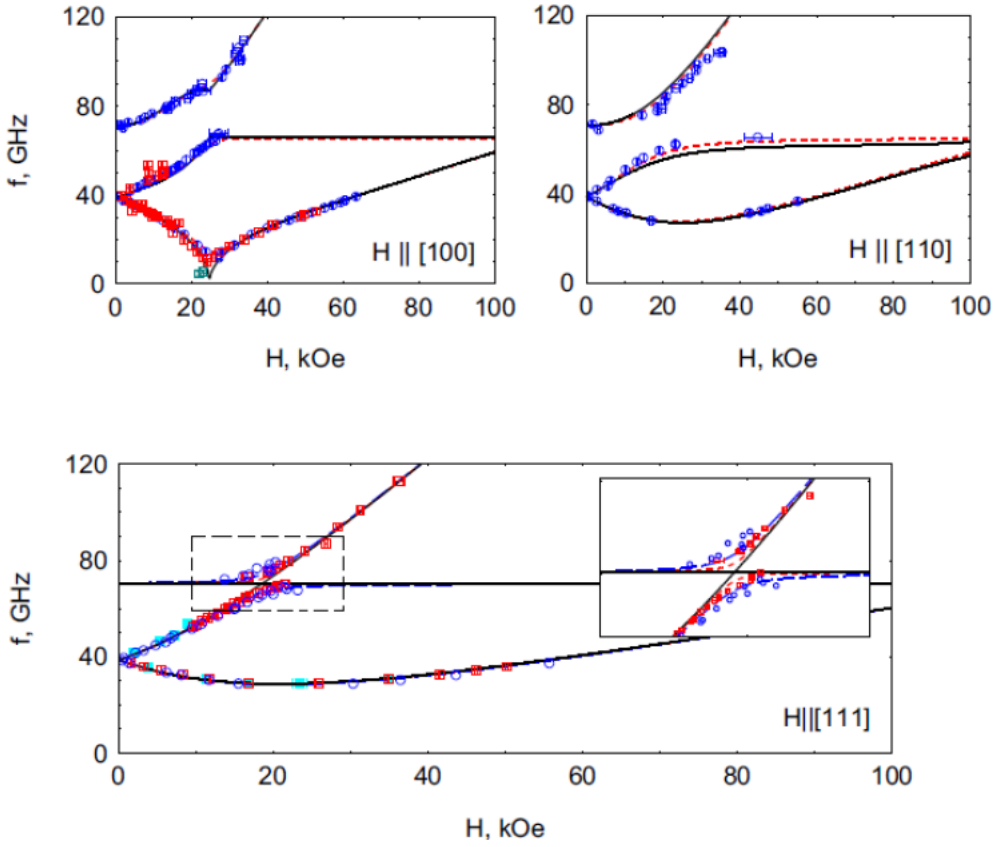

Fig.2. Frequency-field dependence of AFMR in orientations H || [100], H || [110] and H || [111]. Symbols — experimental data, different symbols mark data measured with different spectrometers, solid lines — computed theoretical curves, dashed lines — computed theoretical curves with 5° field deviation.

$Mn_3Al_2Ge_3O_{12}$ is coplanar, all spins lies in <111>, so it is possible to identify four types of magnetic domains. Some of these domains became nonequivalent under applied magnetic field. Suppression of the energetically unfavorable domains explains observed hysteresis. We have found that domain structure can be fully suppressed by the moderate field of about 10 kOe, but it slowly recovers when field is ramped to zero. Characteristic time of this recovery process was found to be about 20 seconds. We suppose that existence of this relaxation is related to reconstruction of equilibrium domains configuration.

We thank Prof. B.V. Mill (MSU) for samples preparation, Prof. V.I. Marchenko and Dr. A.M. Tikhonov (Kapitza Institute) for valuable and stimulating discussions. The work was supported by Russian Foundation for Basic Research Grant No. 16-02-00688.

References

[1] L.A. Prozorova, V.I. Marchenko, Y.V. Krasnyak, JETP 41, 522 (1985)

[2] A. Gukasov, V.P. Plakhty, B. Dorner, et al., J.Phys.: Condens. Matter, 11, 2869 (1999)

[3] A.M. Tikhonov, N.G. Pavlov, JETP 99, 255 (2014)

[4] A. F. Andreev, V. I. Marchenko, UFN, 130, 1 (1980)

[5] V. Glazkov, T. Soldatov, Yu. Krasnikova, Appl. Magn. Reson., 47, 1069 (2016)

[6] Z. A. Kazei, N. P. Kolmakova, M. V. Levanidov, et al., Zh. Eksp. Teor. Fiz., 92, 2277 (1987)

Application of Overhauser DNP and K optics INTERMAGNET quantum magnetometers to fundamental physics and cosmology

V.A. Sapunov[1], J. Rasson[2], A.V. Sergeev[1], E.D. Narkhov[1], B.Y. Rubinstein[3], A.V. Sapunov[1,4]

[1]Ural Federal University, Quantum magnetometry laboratory, 620002,Mira str., 21, Russia
[2]Institut Royal Météorologique Centre de Physique du Globe, Belgium
[3]Stowers Institute for Medical Research, USA
[4]Bernecker + Rainer Industrie Elektronik GmbH, Austria

e-mail: sergeev.ftf@gmail.com, vasapunov@urfu.ru

The recent LIGO project successful proof of the basic statements of Einstein theory on existence of the gravitational waves was a major motive of this proposal. Similar to magnetic field that appears to be a consequence of the electrical field relativistic transformation under condition of speed of light invariance, experimental proof of the gravitational waves leads to a conclusion of existence of the quasi-magnetic gravitational field initiated by accelerated motion of masses [2]. The extremely high cost of the developed network of the LIGO laser detectors naturally leads to increased attention to alternatives methods for gravitational waves detection based on high precision nuclear magnetometers and theoretically predicted spin-gravitational effects. High precision atomic magnetometers can be used for other fundamental research including spin-gravity coupling, tests of Lorentz and CPT violations, detection of dark matter and dark energy [3-5]. In particular, in [3] it is discussed a use of so-called comagnetometers made of two scalar magnetometers, for example, built on a pair of nuclear magnetometers, or nuclear (proton) and electron K optical quantum magnetometers. The fig.1 and text with the permission of the authors the design of co- magnetometer shows.

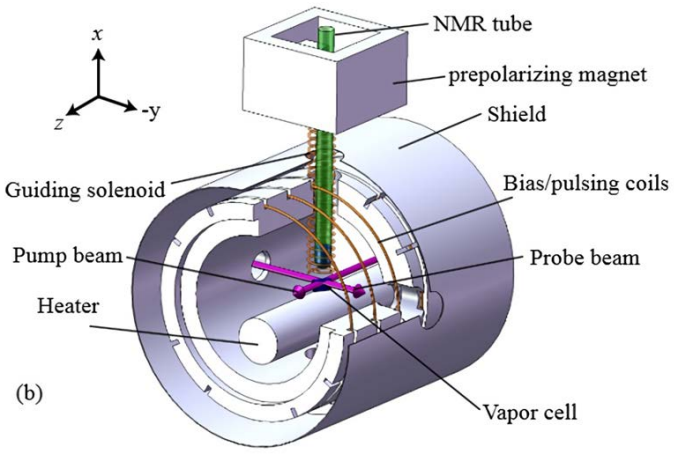

Fig.1. "Experimental setup for the pentane nuclear-spin co-magnetometer. A sample of pentane is polarized in 2 T magnet an moved into a low-field detection region. After the guiding field is removed, the spins precession in a Z directed magnetic field about of 1 mG (100 nT). This precession is monitored by an alkali vapor (K) magnetometers operating in the continues regime."

The best known application of such devices is high precision gyroscope sensors based on the observation that the proton precession frequency changes due to sensor rotation [6]. There is already the similar network GNOME [7]. In fact, these systems are based on the observation of the stability of the word gyroscopic constants and their mutual change when viewed as part of

multi-sensor remote networks over long distances.

A short incomplete list of the requirements to such systems is presented below:

- Minimal possible level of industrial magnetic interferences
- Maximal homogeneity and stability of a weak magnetic field in which the nuclear and electron precession is measured
- Network of spin-gravitational sensors placed at maximal large distances with data transmission to a single data center
- High precision measurement synchronization (for example, using the GPS)
- Long term (multiyear) data accumulation in a single (or cloud) data center with public access for independent processing
- Highly qualified research and management personnel servicing spin-gravitational sensors and data processing of high precision multi-parameter measurements

It is easy to see that these requirements are completely satisfied by the existing network of magnetic observatories INTERMAGNET (including some magnetometer sensor types as a proton precession and K optic quantum magnetometers).

The developers of magnetometer spin-gravitational sensors are working on resolving difficult scientific and technical problems from industrial interference magnetic shielding to sensor deployment in space. Various sensors are under development, including those analogous to optical potassium (K) or cesium magnetometers, and NMR magnetometers with nuclear magnetization amplification based on hyperpolarization (including Overhauser nuclear dynamical polarization). The above considerations lead to a proposal of development of a network for cosmological spin-gravity effects detection based on existing network of magnetic observatories. The development cost of such network (with insignificant hard- and software tuning and access to the original measurements database for data analysis using specialized soft) as it shown on the fig.2.

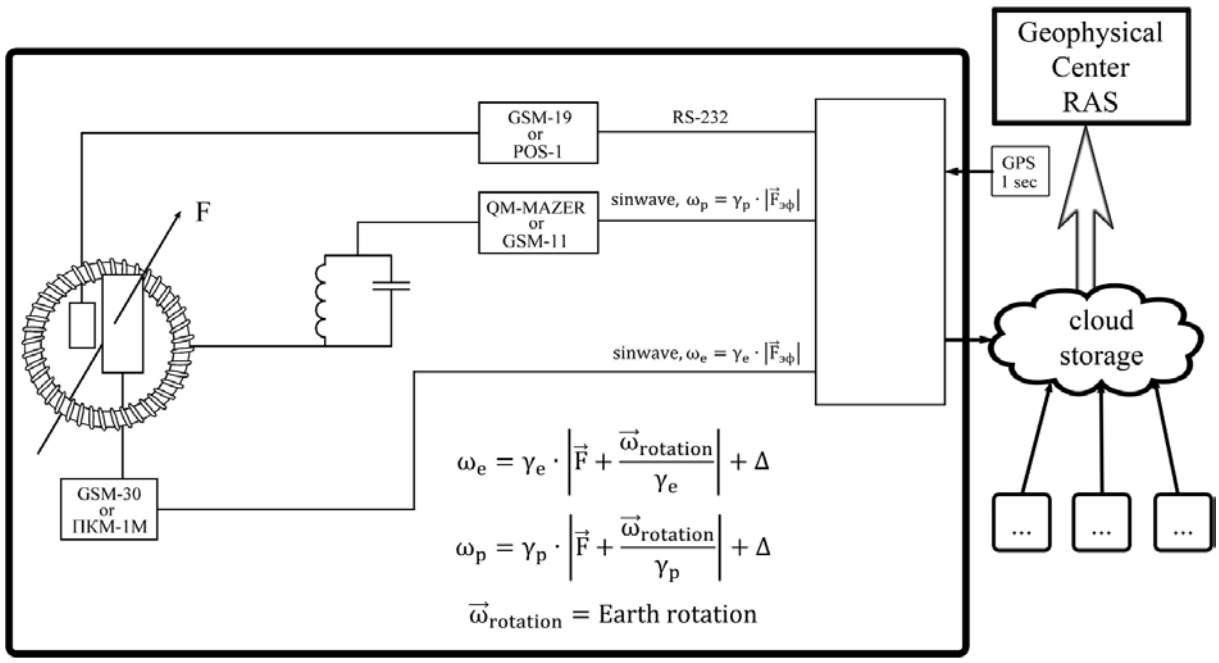

Fig.2. Simultaneous measurement circuit of the proton and K optic continuous magnetometers

An existence of the IAGA developed network of seismic observation bases supports the proposed network of spin-gravitational sensors which in its turn might appear a powerful tool for global seismic prognosis as ground-based spin-gravitational sensor measurements are significantly dependent on geolocation and Earth rotation parameters.

It is assumed that the spin-gravitational effect signal would of the order of magnitude of few fT with the registration time of 100 s and over. Such a signal can be easily detected by K optical magnetometer and potentially by the Overhauser magnetometer with large volume sensors and special algorithms for the signal accumulation. It requires synchronous operation of multiple pairs of magnetometers to eliminate gyroscopic and seismic effects and mutual verification.

The report shows that the magnetometer equipment GEM employed in INTERMAGNET network might satisfy the required parameters after some tuning aimed to direct output of the original electron and proton precession signals to the specialized registration device resolution. It will allow significant increase of magnetic field measurements. A multiyear signal accumulation will make possible to reach the precision level of a few fT in measurement of gradient between Overhauser and potassium magnetometers.

We discuss development of the Overhauser POS magnetometer with GPS synchronization of the proton precession signal. The signal processing algorithm also includes a possibility of real time output time series of the zero crossing for data accumulation and significant increase measurement sensitivity and bit depth. We also describe a regime of precession wide-band registration [8] of several nuclei simultaneously. Simultaneous Overhauser polarization of these nuclei is also possible with the coefficients of an order of (gyromagnetic electron ratio/gyromagnetic nucleus ratio). This option can be useful for development and design of new types of gyroscope and spin-gravitational sensors.

In other words, the rotating Earth is just a float bobbing in a gravitational wave and the INTERMAGNET network can serve as a fishing net for the gravitational waves.

References

[1] Abbott, B.P. et al. Observation of gravitational waves from a binary black hole merger, (2016) Phys. Rev. Lett., 116 (6), art. no. 061102

[2] Jackson Kimball, D.F., Lamoreaux, S.K., Chupp, T.E. Tests of fundamental physics with optical magnetometers (2011) Optical Magnetometry, pp. 339-368.

[3] Ledbetter, M.P., Pustelny, S., Budker, D., Romalis, M.V., Blanchard, J.W. Liquid-State Nuclear Spin Comagnetometers (2012) Phys. Rev. Lett., 108 (24)

[4] Pospelov, M., Pustelny, S, Ledbetter, M. P.,. Jackson Kimball, D. F., Gawlik, W. and Budker, D. (2013) Detecting Domain Walls of Axionlike Models Using Terrestrial Experiments, Phys. Rev. Lett., 110, 021803

[5] Dmitry Budker, Peter W. Graham, Micah Ledbetter, Surjeet Rajendran and Alexander O. Sushkov (2014) Proposal for a Cosmic Axion Spin Precession Experiment (CASPEr), PHYSICAL REVIEW X, 4, 021030

[6] Alexandrov E. B., Pazgalev, A. S. and. Rasson, J. L. (1997) Opt. Spectrosc. 82, 14

[7] https://budker.uni-mainz.de/gnome

[8] Denisov A., Sapunov V., Rubinstein B. Broadband mode in proton-precession magnetometers with signal processing regression methods, Meas. Sci. Technol, 25, №055103,. DOI: 10.1088/0957–0233/25/5/055103, 2014

Multiple-quantum NMR in hybrid organic-inorganic silica gels and aerogels

S.G. Vasil'ev, E.B. Fel'dman

Institute of Problems of Chemical Physics of Russian Academy of Sciences, Chernogolovka, 142432, Moscow Region, Russia

e-mail: viesssw@mail.ru

1. Introduction

Most of the solid materials of practical importance are macroscopically homogeneous but reveal heterogeneity at the microscopic scale. A good example is hybrid organic-inorganic silica-based materials which have a wide range of successful commercial applications [1]. Apparently the properties of such materials depend not only on the bulk chemical composition but substantially upon the molecular level organization. Due to the lack of long-range order experimental results in many cases cannot provide a complete picture of such structures.

Solid state NMR provides a number of powerful tools for investigation of disordered systems. Among them is multiple-quantum (MQ) NMR [2] which possesses advantage in observing various multiple-spin transitions between the Zeeman levels of a system of interacting spins in an external magnetic field which in principle can be used to obtain information on the structure at considerably greater scales [3]. MQ NMR was successfully applied to study organic solids, amorphous semiconductors, adsorbates on catalysts and chromatography columns, polymer networks [4,5]. MQ NMR is also an important method for the investigation of various problems of quantum information processing such as transmission of quantum information and decoherence processes [6].

In the present study we investigate possibilities of MQ NMR to discriminate between silicone materials with similar chemical composition but different structures and also trace the influence of the ^{1}H abundance in the systems.

2. Materials and methods

Four samples for investigation were chosen: adamatnane (sample a) and two different types of silicone materials - QM silicone resins (samples c and d) and aerogel (sample b). Adamantane is used here as the most studied from the point of view of MQ NMR experiments substance. QM resins are compounds constituted of tetra-functional Q (SiO_2) and mono-functional M ($OSi(CH_3)_3$) units forming a core-shell structure with inorganic core [7,8]. Aerogels are highly porous materials with typical sizes of particles of 2-5 nm. Aerogel used in this study was obtained from methyltrimethoxysilane by sol-gel process with subsequent supercritical drying [9]. The constituting unit is tri-functional in this case (O_3SiCH_3). For all silicone materials the source of ^{1}H NMR signal is methyl groups neglecting small silanol functionalities inherently present in such materials.

Experiments were performed on a Bruker Avance III spectrometer at room temperature on ^{1}H nuclei at 400 MHz (9,4 T) using a home-built probe [10]. Powdered samples were packed in a 2 mm glass tubes. The pulse sequence used for excitation of MQ NMR coherences is described in the seminal works on spin-counting experiments of Baum and Pines [2,11]. Phase-incremented spin-counting experiments were performed by incrementing phase of the pulses on the preparation period in 128 steps for subsequent slices of a 2D experiment. Signal in indirect dimension was concatenated four times prior to Fourier

transformation. The duration of the basic cycle consisting of eight 90 pulses was 58.8 μs, duration of the pulse - 0.9 μs. Basic cycle was repeated up to 10 times to obtain the desired preparation time τ in different experiments. Repetition time was chosen to be $\geq 5T_1$.

3. Results and discussion

Profiles of the MQ NMR coherences of the investigated samples for different preparation times are presented in fig.1. Two samples of QM resins (fig.1c) and fig.1d)) have the same constituting units but in different proportion. The sum of intensities in fig.1. is normalized to 1 for each preparation time τ. For all samples redistribution of intensities to the higher coherence orders with increasing preparation time is observed.

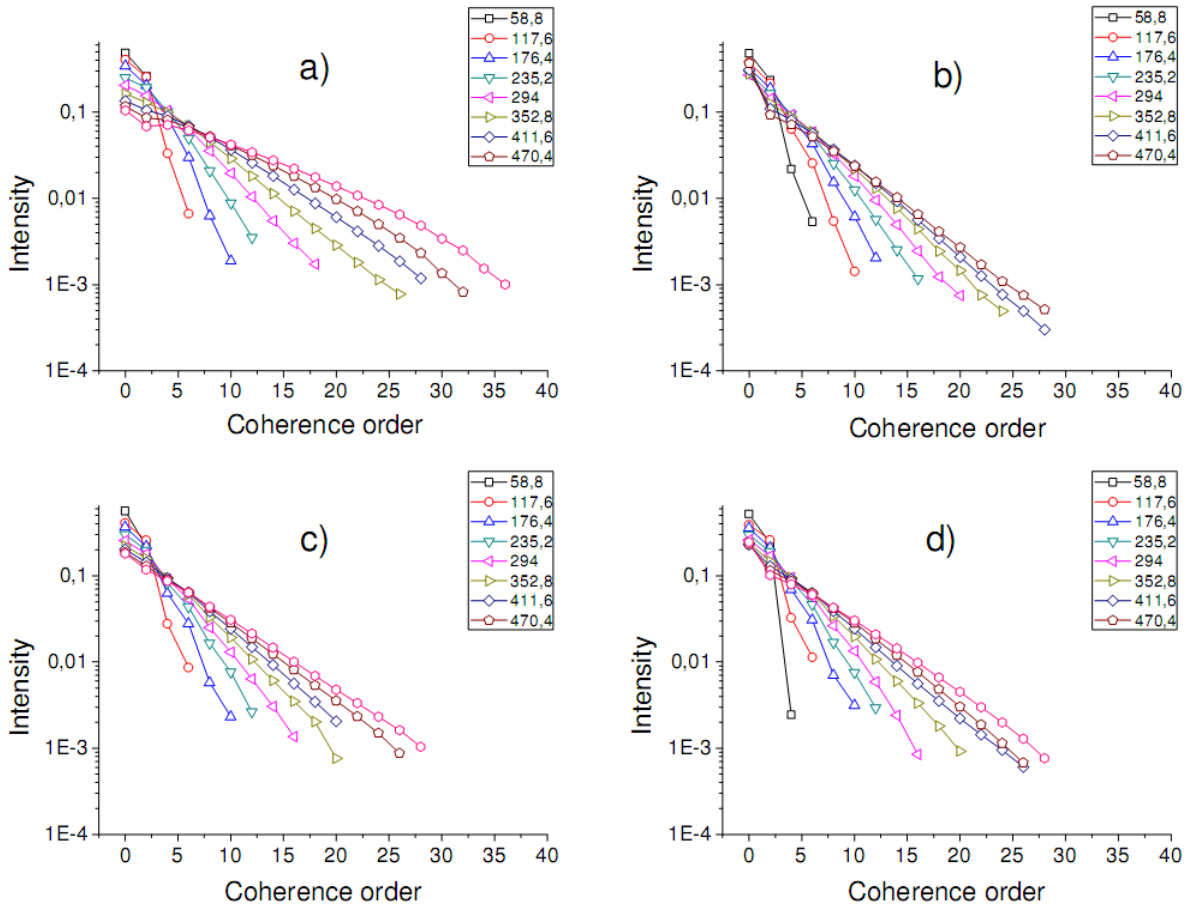

Fig.1. Profiles of MQ NMR coherences of a) adamantane; b) T-aerogel; c) and d) QM resins with Q:M ratio of 1:1 and 2:1 respectively. Preparation times τ of the MQ NMR experiments are indicated in the insets (in μs).

The simplest way of interpretation of MQ spectra relies on the fact that the maximum possible MQ coherence order that can be excited gives a count of the number of spins in an isolated cluster. Spin counting may also be applied to extended networks of spins. A Gaussian model based on the statistical arguments was proposed for this case [2]. Amount of n-quantum coherence *I(n)* in dipolar-coupled *N*-spin cluster is given by C_{N-n}^{2N}, which is further approximated by a Gaussian function as exp(-n^2/*N*). By fitting the observed *I(n)* to exp(-n^2/*N*) one can obtain the effective spin-cluster size *N*. Although it was noted that this model oversimplifies spin dynamics [3,12] it was shown to be practically useful in many cases [4].

Fig.2. represents the changes of the effective spin cluster size during the irradiation on the preparation period. All samples show the unlimited monotonic growth of the cluster size

with increasing τ. This indicates that ^{1}H spins in investigated systems represent extended homogeneous networks rather than isolated clusters. For the adamantane the *N(τ)* curve exhibits a concave upward shape while for other samples smoother growth is observed. This difference could be attributed to the influence of the dimensionality of ^{1}H spins distribution in samples. Adamantane is an example of 3D distribution of spins [4] while the investigated samples bear the proton-containing groups on the surface of the SiO_2 frame. QM resins represent a core covered by methyl groups on the surface. T - aerogel have the loose frame covered by methyl groups.

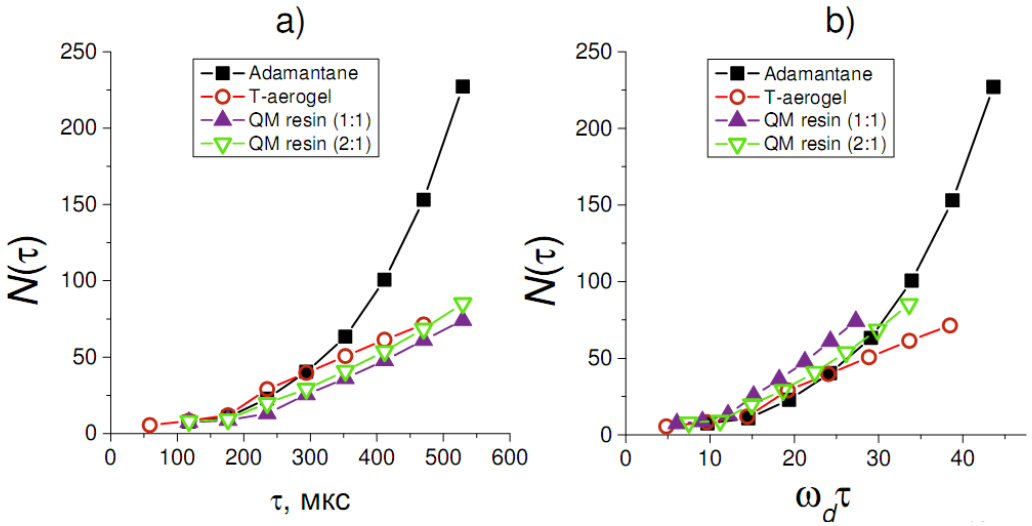

Fig.2. Effective number of correlated nuclei N(τ)as function of the duration of preparation period τ.

The rate of the MQ NMR coherences development is affected by the dipolar coupling between spins. To account for this fact we have scaled the curves by multiplying τ by the linewidths of the ^{1}H spectra of corresponding sample (fig.2b)). In such scale QM resin with the ratio of 1:1 (sample c fig.2b)) shows the fastest growth. Apparently this reflects the abundance of the ^{1}H spins in the system since the sample c contains more protons than samples b and c. Samples b and c have almost the same proton content. Differences in this case could be ascribed to the differences in the structures – loosely distributed methyl groups in aerogel shows the slower growth of the MQ NMR coherences.

4. Conclusions

Development of MQ NMR coherences on the evolution period of MQ NMR experiment of methyl groups in different types of silicone compounds was investigated. The distribution of ^{1}H in the T-aerogel and QM resins was shown to be uniform. In addition to the traditional NMR which is sensitive to the bulk chemical composition, local chemical environment and motions MQ NMR gives more detailed information about the architecture of non-crystalline solids. Our experimental results show that the growth rate of the MQ NMR coherences reflects not only the abundance of ^{1}H spins in investigated silicone materials but also density.

These findings are valuable for characterization of the distribution of functional groups in silicone materials and could be useful in investigation of surface area and porosity.

The work is supported by the Russian Foundation for Basic Research (grants No. 16-33-00867 and No. 16-03-00056)

5. References

[1] B. Arkles, MRS Bull. **26**, 402–407 (2001)

[2] J.Baum, M.Munoviz, A.N.Garroway, A.Pines, J. Chem. Phys. **83**, 2015-2025 (1985)

[3] S.I. Doronin, I.I. Maksimov, and E. B. Fel'dman, JETP, **91**, 597–609 (2000)

[4] K.K. Gleason Multiple Quantum NMR in Solids in Encyclopedia of Magnetic Resonance (2007)

[5] C. E. Hughes. Prog. Nucl. Magn. Reson. Spectrosc., **45**, 301–313 (2004)

[6] G.A. Bochkin, E.B. Fel'dman, S.G. Vasil'ev, Z. Phys. Chem. **230** (2016)

[7] V.V. Kazakova et al., J. Inorg. Organomet. Polym. **22**, 564–576(2012)

[8] S.G. Vasil'ev et al., Appl. Magn. Reson **44**, 1015–1025(2013)

[9] S.A. Lermontov et al., Russ. J. Inorg. Chem. **59**, 1392-1395(2014)

[10] S.I. Doronin, S.G. Vasil'ev, A.A. Samoilenko, E.B. Fel'dman, and B.A. Shumm, JETP Letters **101**, 613 (2015)

[11] D.N. Shykind, J. Baum, S.-B. Liu, A.Pines, A.N. Garroway, J. Magn. Reson. **76**, 149-154 (1988)

[12] S. Lacelle, S.-J. Hwang, B.C. Gerstein J. Chem. Phys. **99**, 8407 (1993)

ESR study of new low-dimensional magnet $Co(NO_3)_2$

R.S. Denisov[1], E.B. Deeva[1], E.A. Zvereva[1], I.V. Morozov[2], O.S. Volkova[2], A.N. Vasiliev[2]

[1]Faculty of Physics, Moscow State University, Moscow, 119991 Russia
[2]Faculty of Chemistry, Moscow State University, Moscow, 119991 Russia

e-mail: rsdenisov@gmail.com

EPR study of new low-dimensional magnet $Co(NO_3)_2$ was performed using an X-band EPR spectrometer CMS 8400 Adani(f = 9.5 GHz, B ≤ 0.7 T) equipped with a low temperature mount (6 – 300 K). The typical EPR absorption signal represent a superposition of two distinct asymmetric modes, which are denoted as L_N and L_W in fig.1. Taking into account the structural data two resonance modes were assigned to two different Co^{2+} sites in the crystal structure of $Co(NO_3)_2$.

For S = 3/2 spin system (HS Co^{2+}, d^7) in octahedral environment, the zero field perturbation splits the energy levels into two doublets, $|\pm1/2\rangle$ and $|\pm3/2\rangle$. Thus, the nature of each component in the spectrum, L_N or L_W, could be attributed to the transitions between the ground state Kramers doublet with anisotropic g-factor, which is assumed to originate from the involvement of an excited doublet with an effective spin of 3/2 [1]. Rather different values of the resonance fields for L_N and L_W modes clearly indicate two different type of Co^{2+} ions in $Co(NO_3)_2$ with different crystal field splitting of the energy levels.

In order to get quantitative estimations for the effective g-factors we have fitted the spectrum within two different field ranges corresponding to L_N and L_W lines. The reasonable description of the lineshape for the L_N and L_W modes can be achieved by sum of two Lorentzians (red dashed curve in fig.1) and by sum of threeLorentzians (blue solid curve in fig.1) respectively. The principal values of the g-tensor for Co1 position (L_N mode) were

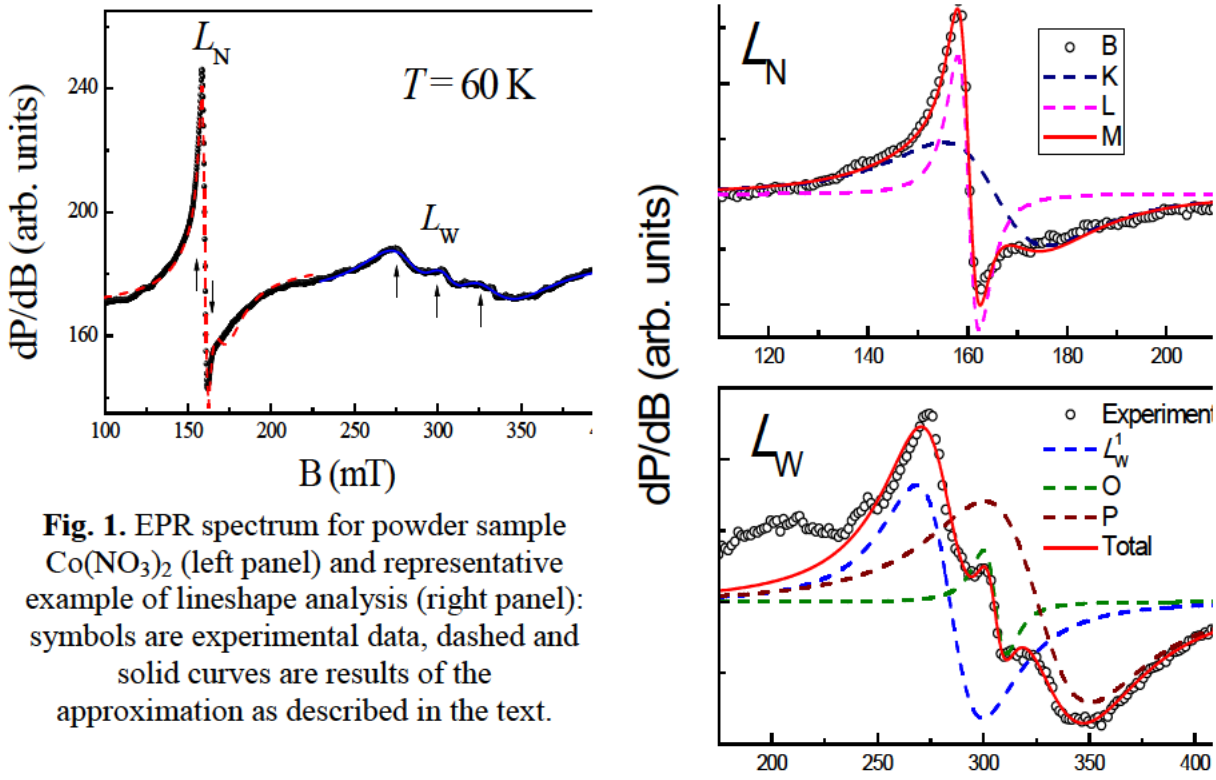

Fig. 1. EPR spectrum for powder sample $Co(NO_3)_2$ (left panel) and representative example of lineshape analysis (right panel): symbols are experimental data, dashed and solid curves are results of the approximation as described in the text.

found to be $g_{\perp}$ = 4.01(3) and $g_{\parallel}$ = 4.16(2), giving the sum ($2g_{\perp} + g_{\parallel} \approx 12.2$) in very good agreement with the theoretical value near 13 proposed by Abragam and Pryce [2] for high-spin Co^{2+} (S = 3/2) in pure octahedral oxygen coordination. At the same time, the *g*-tensor values for Co2 position (L_W mode) are g_1 = 2.33(6), g_2 = 2.17(6) and g_3 = 2.03(1) resulting in average value $g = 2.18 \pm 0.01$, which indicate a less symmetric environment of ligands for this site in full agreement with crystal structure data.

The temperature dependence of the main ESR parameters were also obtained and discussed in comparison with static magnetization data.

References

[1] A. Abragam and B. Bleaney, *EPR of Transition Ions*, Clarendon, Oxford, 1970

[2] A. Abragam and M. H. L. Pryce, Proc. R. Soc. London, Ser. A **200**, 173 (1951)

Perspective applications of NMR relaxometery to blood thromboelastography

A.V. Fedorov, E.D. Narkhov, E.D. Baglasov, A.V. Sergeev, A.Yu. Denisov, V.A. Sapunov

Ural Federal University, Quantum magnetometry laboratory, 620002,Mira str., 21, Russia

e-mail: fedorov.fti@gmail.com, vasapunov@urfu.ru

NMR relaxometry is widely applied in diffusive molecular motion research. Sometimes it is not possible to separate different phases of the compound and obtain individual NMR relaxation exponents leading to drastic drop in the quality of the results. We present a novel application field with numerous NMR relaxometry advantages (including low equipment cost), namely, a laboratory analysis of blood coagulation process and dynamics. The standard equipment is based on various types of viscometers including capillary and rotational ones. The NMR relaxation can provide some important information in addition to the standard coagulation dynamics. In our opinion, the best results in the field belong to Harvard University based company T2BioSystem (http://www.t2biosystems.com) [1-2]. Our results lag behind but still are quite important from the point of view of import replacement.

Fig.1 shows portable proton NMR relaxometer NP-1 (Dr. Kashaev, Idea Resonanse LLC, Kazan, Russia) we used in our research. In collaboration with Dr. Sukhanov lab, Clinical Homeostasiology Center, Yekaterinburg, Russia. We performed analysis of blood specimens, including blood samples and coagulation clots. The NMR signals of specimens of 1 cm^3 were detected easily. The measurement were performed using the spin echo method with phase alternation of 180 degree impulses. The blood samples produced $T_2 \sim 0.3$ s with clear single exponential signal decay. The clots demonstrated a double exponential signal decay with slow component of 0.1 s and fast component less than 10 ms which implies presence of free fluid in porous scaffold. Both fast and slow phases significantly varies between the samples, as the number of samples was insufficient to make any conclusions.

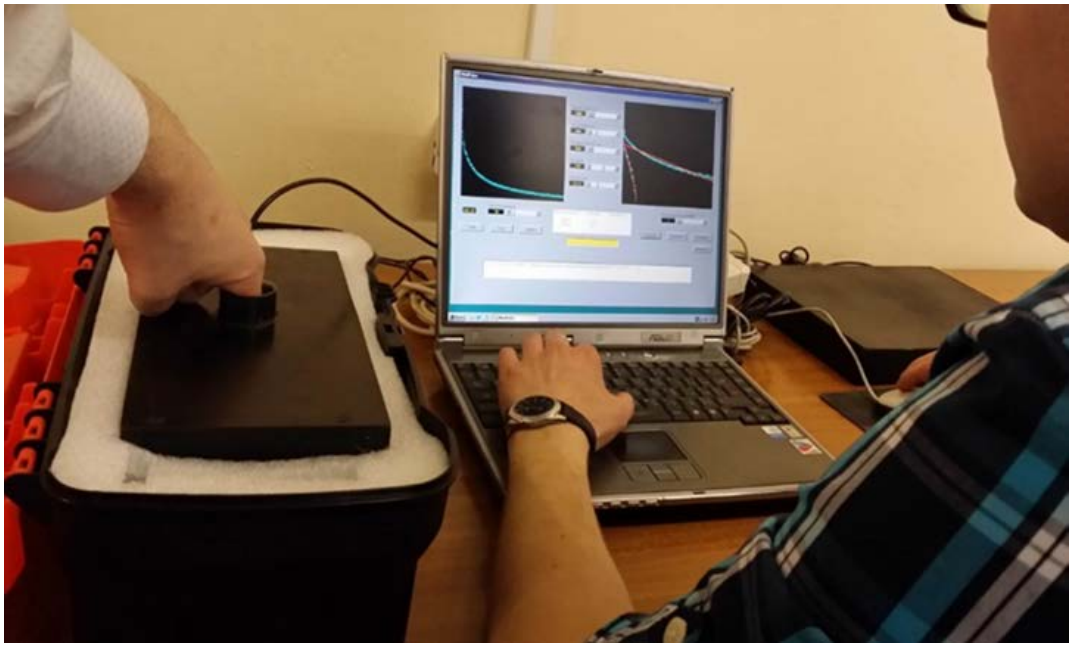

Fig.1. Portative proton NMR relaxometer NP-1 measures relaxation in male index finger

Table 1 presents a comparison of NP-1 and desktop Minispec Pc 120 (Bruker) relaxometers.

Specifications	PMR relaxometer NP-1	Minispec Pc 120, Bruker
Resonant frequency, MHz	10-12	10-40
Sample diameter, mm	10-30	10-40
Power consumption, Wt	15, no magnet temperature stabilizer	300 including magnet temperature stabilizer
Size, sm. Electronic blok Magnet	4x25x30 28x13x13	106x54x43 106x54x43
Weight, kg	15	80

We also applied the NMR relaxometer NP-1 to ***in vivo*** research. The magnet design as shown in fig.1 allows perform the measurements on human fingers inaccessible for other desktop relaxometers with permanent magnets. Fig. 2 shows the relaxometer display during the recording and double-exponent analysis of transversal relaxation process in index finder.

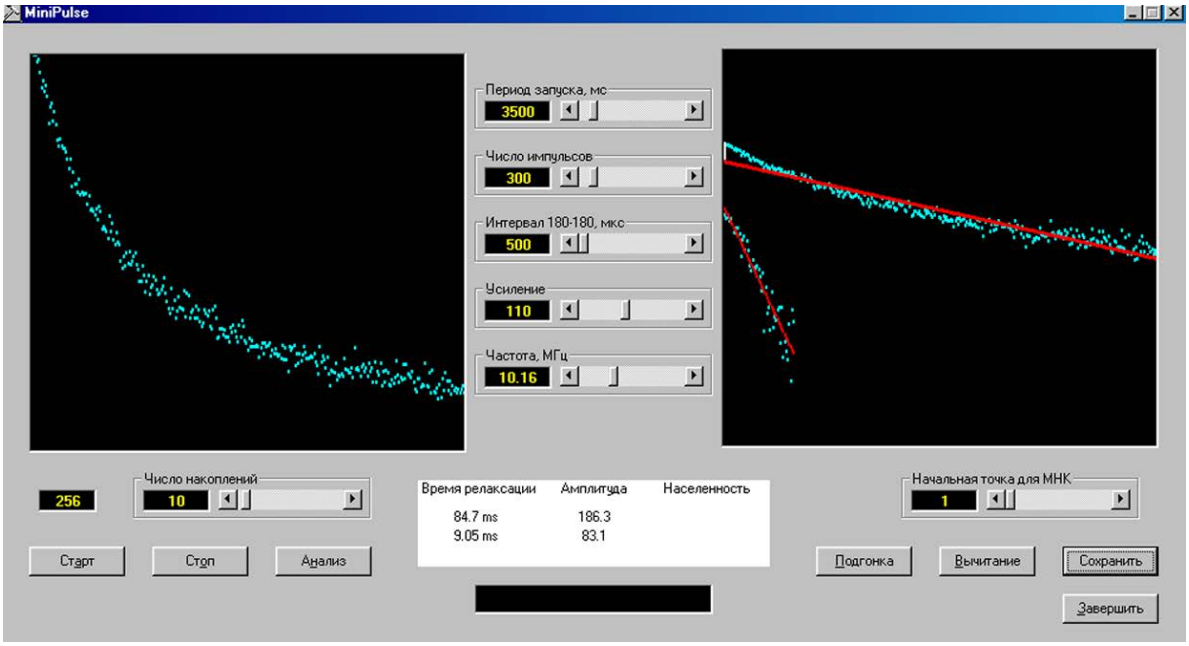

Fig.2. Relaxometer NP-1 display showing the male index finger data recording and analysis.

The students and professors of FTI, UrFU, Yekaterinburg, participated in the research. The working parameters NMR relaxometer were selected for the biological tissue investigation. We established the requirements for the specialized NMR sensor for *in vivo* measurements of relaxation NMR parameters of blood and biological fluids in middle and index fingers. All young participants showed the results similar to that of shown in Figure 2. Slow T_2 component was in the range 90-120 ms, while the fast one was 10-20 ms. Older participants demonstrated the relaxation time decrease of 10-15% with some variation of unknown nature. In some cases the fast component was not detected and we have no explanation for this behavior. We plan investigation of simultaneous recording of sample coagulation index and transversal relaxation time for finger blood to design of noninvasive express analysis approach.

References

[1] Luo, Z.X., Fox, L., Cummings, M. et. al. New Frontiers in *in vitro* Medical Diagnostics by Low Field T2 Magnetic Resonance Relaxometry. *Trends in Analytical Chemistry*. (2016)

[2] Sun, N., Yoon, T. J., Lee, H., et. al. (2011). Palm NMR and 1-chip NMR. *IEEE journal of solid-state circuits*, 46(1), 342-352.

New vector/scalar Overhauser DNP magnetometers POS-4 for magnetic observatories and directional oil drilling support

E.D. Narkhov[1], A.V. Sergeev[1], D.N. Milyukov[1], A.N. Shirokov[1], D.V. Saveliev[1], V.A. Sapunov[1], A.Y. Denisov[1], S.Y. Khomutov[2], P.A. Borodin[3]

[1]Ural Federal University, Quantum Magnetometry Lab., Mira., 21, Ekaterinburg, 620002, Russia

[2]Institute of Cosmophysical Research and Radio Wave Propagation, FEB RAS, Mirnaya, 7, Kamchatskiy Kray, Paratunka, 684034, Russia

[3]Geophysical Observatory "Arti", Institute of Geophysics, UB RAS, Geophysical st., 2a, Sverdlovsk region, Arti, 623350, Russia

e-mail: narhoved.ftf@gmail.com, vasapunov@urfu.ru

The physical base of proton Overhauser magnetometry is a Larmor precession of nuclear magnetic moments in a magnetic field. Proton magnetometers determine an absolute value of the measured magnetic field induction T_0 [1]

$$T_0 \equiv \left|\mathbf{T}_0\right| = \gamma_p^{-1}\omega_0, \tag{1}$$

where $\gamma_p = 2\pi \cdot 0.0425764$ rad/(nT s) [2] denotes the proton gyromagnetic ratio and ω_0 is the frequency of proton precession. These magnetometers are well-known as high precision stable sensors of magnetic field absolute value. They are widely used in various applications including geophysics and observatory measurements. Fig.1 shows the general scheme of proton precession Overhauser DNP measurement (Overhauser magnetometer).

In addition, absolute vector proton magnetometers based on the switching of bias magnetic fields were developed (for example [3]). In recent years, the development of proton vector magnetometers achieved significant progress due to implementation of the Overhauser effect which is related to the dynamic nuclear polarization (DNP) due to electron subsystem excitation. Additional gain provides stronger proton signal from smaller sensor size. This allows to reduce dimensions of the magnetic switching systems and as consequence, to improve measurements sensitivity.

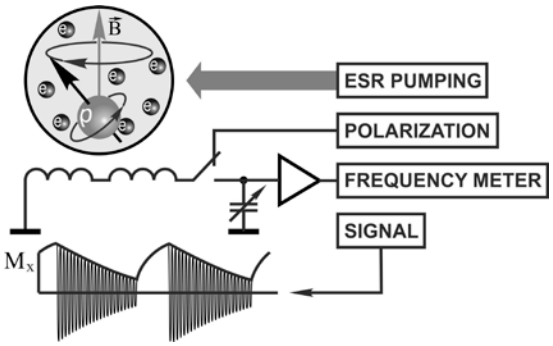

Fig.1. General scheme of DNP measurement

To measure the components of the geomagnetic field by a proton (scalar) magnetometer a number of methods are known. We discuss the setup based on the switching of bias magnetic fields **B** (cycle $+I$, $-I$, $I = 0$) with the measurement of resulting total field. The vector diagram for a switching method (fig.2) and formula (2) for calculation of the field component Z along switching bias field are shown below:

$$Z = \frac{T_1^2 - T_2^2}{2\sqrt{2(T_2^2 + T_1^2 - T_0^2)}}, \quad \mathbf{T}_{1,2} = \mathbf{T}_0 \pm \mathbf{B}. \tag{2}$$

It is a well-known formula, but, unfortunately, it does not provide any useful

information to select value of the switching bias field. Nor does it determine the effect of the selected parameters upon the resulting random and systematic measurements errors of Z.

Assume identical sensitivity for all measurements of the field absolute value $\sigma(T_0)=\sigma(T_2)=\sigma(T_1)=\sigma(T)$, then the value of dispersion of Z component measurement reads

$$\sigma^2(Z)=4\sigma^2(T)\left(1+2\,(T_0/B)^4\cos^2\alpha+(T_0/B)^2(1-3\cos^2\alpha)\right). \qquad (3)$$

Fig.3 shows the ratio $\sigma(Z)/\sigma(T)$ representing sensitivity deterioration of the Z component measurements compared to sensitivity of the scalar magnetometer as a function of the ratio (geomagnetic field absolute value)/(switching bias field) T_0/B at various angles between them.

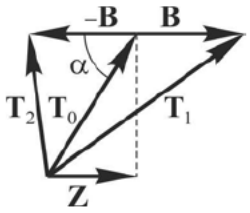

Fig.2. Vector circuit for a switching method

The sensitivity of component measurement is the best at $\alpha=0$, $T_0/B=0.5$ when the loss of sensitivity is $\sigma(Z)/\sigma(T)\sim 0.57$. Unfortunately, this case is not relevant for application because the increase of the bias field causes an increase of its gradient that means too high requirements for the switching magnetic system. Also, there is a restriction on the bias field amplitude due to the dynamic range of the proton magnetometer (usually 20000 – 100000 nT). More interesting is the intermediate range, when the sensitivity of component measurements does not depend on the orientation of the bias magnetic field and total intensity. This bias field should be approximately 70% of the geomagnetic field, with a factor 3 in the sensitivity deterioration.

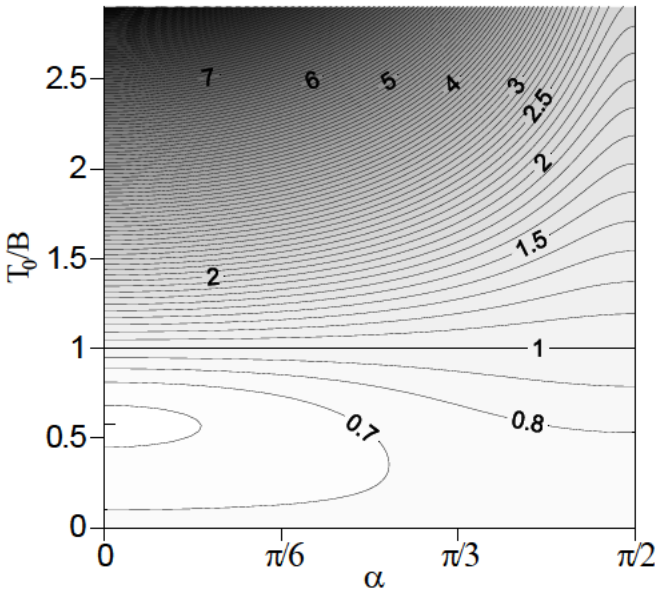

Fig.3. Loss of sensitivity of vector magnetometer in comparison to scalar magnetometer.

Error caused by instability of the bias field or the power source is a technically important kind of the error since it defines the requirements to the stability of the magnetic switching system and source of the switched current. We assume that the fields +**B** and –**B** differ by ΔB and find the error caused by the instability of the bias field or the power source as:

$$\Delta Z=0.5\,B\,(\Delta I/I)\left(1-(T_0/B)^2\cos^2\alpha\right)=0.5\,\Delta B\left(1-(T_0/B)^2\cos^2\alpha\right). \qquad (4)$$

Estimate the requirements on stability for the switching bias field or $\Delta I/I$ in conditions close to optimum (T_0/B about 1.5, B about 30000) and setting error $\Delta Z \approx 1$ nT. We find the value of $\Delta I/I$ to be about 10^{-4}. Thus requirements to short-term stability of the current I and switching bias field can be met engineering-wise and we have errors of 0.1 – 1 nT for instability $10^{-5} - 10^{-4}$. It is important to note that the long-term stability does not exert influence on the switching method in contrast to a method of the field component compensation.

It was revealed at experimental research of the Overhauser vector magnetometers in laboratory conditions, which were characterized by fast changes of the geomagnetic field, that the switching method has also a dynamic error. To estimate the error caused by a field variation, the jump function model of a variation was simulated. Namely, at the first measurement the geomagnetic field is displaced by $-\Delta\mathbf{h}$, in the second one there is no displacement and in the third one the field is displaced by $\Delta\mathbf{h}$. A vector proton magnetometer calculates the Z field component according to the basic formula (2). The error is defined as the difference between the measured and calculated component without the drift $\Delta\mathbf{h}$ that is $\Delta Z_1 = Z' - Z$:

$$\Delta Z_1 = \frac{T_1'^2 - T_2'^2}{2\sqrt{2(T_2'^2 + T_1'^2 - 2T_0'^2)}} - Z = \frac{1}{B^3}\left[\mathbf{T}_0 \times \mathbf{B}\right]\left[\mathbf{B} \times \Delta\mathbf{h}\right] \le \Delta h T_0 / B \qquad (5)$$

The analysis of this result shows that the drift error is due to a dynamic cross effect:

- There is an influence (error) due to variations of perpendicular components.
- The error is proportional to speed of variation, more precisely it is proportional to field change during the measurement cycle (~ the discretized time derivative of field).

Fig.4 shows an example of the drift error calculation. The top panel is a simulated Z variation. The variation in H direction is absent, and the measurement of H-component is made along the switching bias field and show presence of the dynamic cross effect.

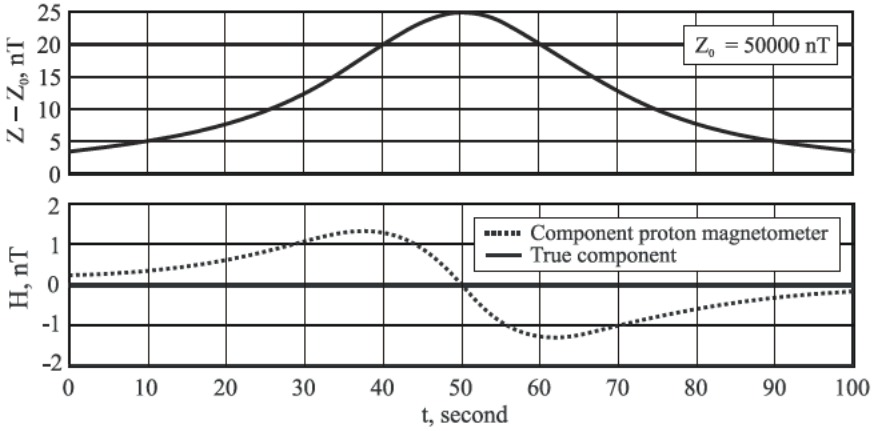

Fig.4. Error caused by the drift of the geomagnetic field as result of dynamic cross effect for the proton vector magnetometers (The calculation cycle is 3 s).

Some discrepancy of variation measurements relative to fluxgate vector magnetometers thus should be observed. Obviously the drift error can be eliminated by some modernization of the basic formula (2) or during measurement data processing taking into account variation speed.

The Quantum Magnetometry Laboratory designed and developed stable vector magnetometer POS-4 (fig.5) based on the module sensor POS-1. We discuss the long-term

test experiments at magnetic observatories Arti and Paratunka [4] in which stability 2 nT/year and sensitivity of the field components better than 0.1 – 0,3 nT and geomagnetic field absolute value in the range 0.01 – 0,03 nT were obtained.

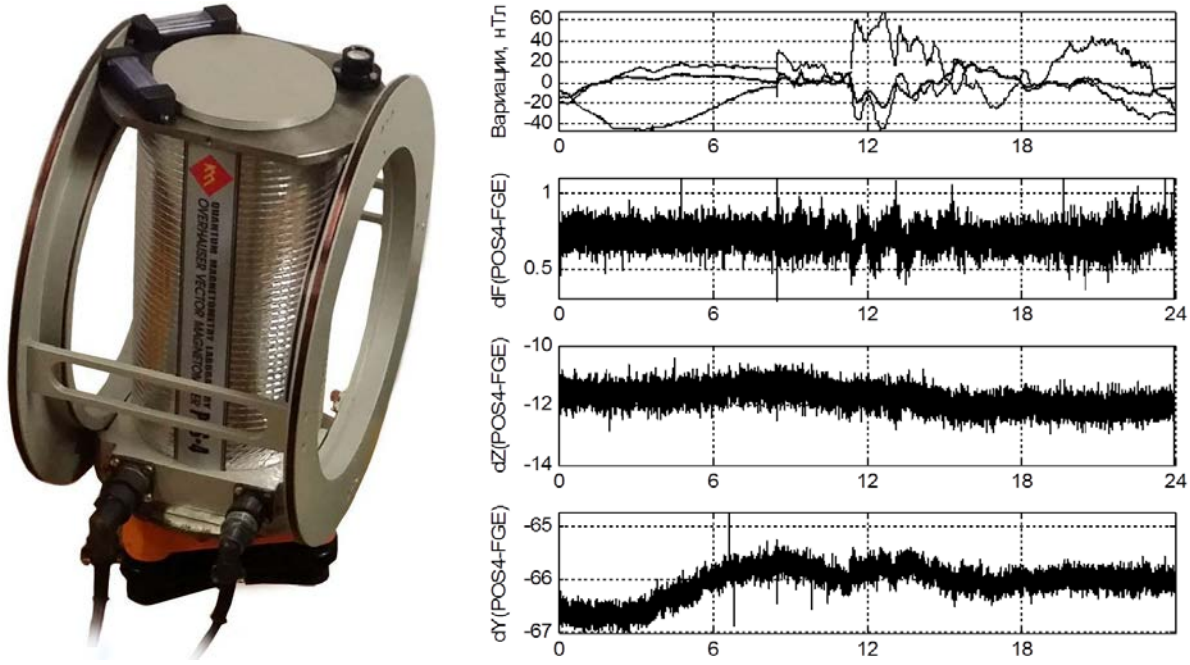

Fig.5. Magnetic system of scalar + vector magnetometer POS-4 and a daily record example signal relative to fluxgate magnetometer FGE.

The POS-4 is an analog of the famous Canadian dIdD+F magnetometer applied both in observatories and for directional drilling support of oil and gas wells [5]. The difference is in the absolute component measurement with the vertical orientation by the float. The azimuth angle declination D to the geographical north is provided by the telescope on the POS-4 magnetic switching system and GNSS markup.

References

[1] Denisov A., Sapunov V., Rubinstein B. Meas. Sci. Technol. **25**, 055103 (2014)

[2] Morh P.J., Taylor B.N., Newell D.B. Reviews of Modern Physics **84**, 1527 (2012)

[3] Sapunov V., Rasson J., Denisov A., Saveliev D., Kiselev S., Denisova O., Khomutov S. Earth, Planets and Space **58**, 711 (2006)

[4] Solar-Terrestrial Relations and Physics of Earthquake Precursors, VII International Conference, August 29, 2016, Paratunka, http://www.ikir.ru/ru/Events/Conferences/2016-VII-international/reports/downloads/sbornik/223-227.pdf

[5] Gvishiani A.D., Lukianova R.Yu., Soloviev A.A. Gornyi Zhurnal, **10**, 94 (2015)

Pulse NMR investigations of $MnCO_3$

Yu.M. Bunkov[1], A.V. Klochkov[1], T.R. Safin[1], K.R. Safiullin[1,2], M.S. Tagirov[1,2]

[1]Kazan Federal University, 420008, Kremlevskaya 18, Kazan, Russia.

[2]Institute of Perspective Research, TAS, 420111, L.Bulachnaya 36a Kazan, Russia.

e-mail: TiRSafin@gmail.com

Abstract. Solid state antiferromagnet $MnCO_3$ has been investigated by pulse magnetic resonance methods. The observation of the unusual spin echo signal behavior in the sample is reported. Experimental data confirm the formation of coherent spin precession in the sample.

There are different types of ordered states. Major class is presented by equilibrium macroscopic ordered states exhibiting spontaneous breaking symmetry. This class contains different types of ordered magnets; superfluids, Bose condensates and superconductors; etc. The main frame of the studied effect is Bose-Einstein condensation (BEC) of quasiparticles. It corresponds to the accumulation of the macroscopic number of particles at the ground-state level, described by a single wave function. The formation of this state for bosonic particles was predicted by S.N. Bose and A.Einstein in 1925. The "pure" BEC state of ^{87}Rb atoms was experimentally observed in 1995 by E.Cornell [1]. The BEC state of quasiparticles (magnons) was experimentally observed in ^{3}He-B superfluid phase in 1984 and explained theoretically at the same time [2,3] as a coherent precession of magnetization.

The very similar states of magnon BEC were found in easy-plane antiferromagnets $CsMnF_3$ and $MnCO_3$ [4-6]. These materials characterized by the coupled nuclear-electron precession. Magnetic moments are coupled to each other by strong exchange and dipole-dipole interaction. That is why the violation of the magnetic order does not localize and spreads as the wave across the sample. Such waves are called spin waves and quasiparticles, which correspond to the quanta energy — magnons. The Bose-Einstein of magnons is observed when major amount of magnons are condensed at the ground state with wave vector $k = 0$. The different coherent magnon states, similar to charge density waves in metallic wires was also found in yttrium iron garnet films [7].

In the present work the question about the magnons coherence during relaxation process after the magnon excitation has been raised. For the magnon BEC state the amplitude and frequency of the signal are usually determined by the density of excited magnons [8]. It was shown experimentally [9] that the BEC state relaxes without loss of the coherence. The amplitude and the frequency of BEC induction signal changes slowly as magnon density decays. The similar behavior has been found in the Q-ball state [10]. In the last case the redistribution of magnons from excited state to a ground state was also observed.

In our experiments with pulse nuclear magnetic resonance the magnetization is created by constant magnetic field. Pulse of radiofrequency field (RF) deflects the magnetization on the β angle, after that the free induction decay (FID) signal is measured. In the incoherent precession state spins almost instantly lose the information about primary phase and frequency after the RF pulse. The observed decay signal is extremely small due to this incoherent. In coherent state all spins precess in phase. That is mean that the whole macroscopic magnetization precesses in volume V of the sample.

The experimental data shows, that the echo signal does not form in the presence of coherent state, when the deflection angle more than critical angle [11], however echo signal can be formed after BEC state signal decays, fig.1.

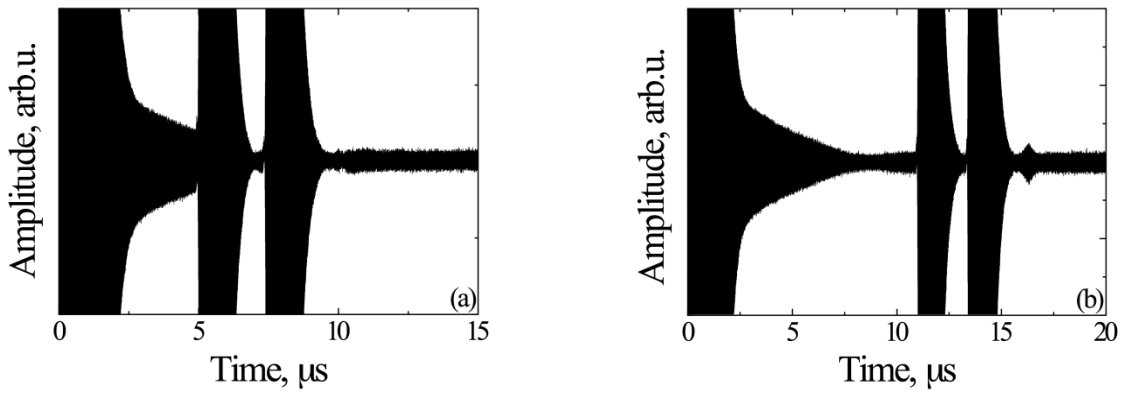

Fig.1. Free induction decay and echo signals. 5 μs (a) and 11 μs (b) delay between 100 ms pulse and echo pulse sequence has been applied.

References

[1] M.H. Anderson, J.R. Ensher, M.R. Matthews, C.E. Wieman and E.A. Cornell, *Science.* **269**, No. 5221, pp. 198-201 (1995).

[2] Borovik-Romanov A.S., Bunkov Yu.M., Dmitriev V.V., Mukharskiy Y.M., *JETP Lett.* **40**, 1033 (1984).

[3] Fomin I.A., *JETP Lett.* **40**, 1037 (1984).

[4] Bunkov Yu.M., Alakshin E.M., Gazizulin R.R., Klochkov A.V., Kuzmin V.V., Safin T.R., Tagirov M.S., *JETP Lett.* **94**, 68 (2011).

[5] Bunkov Yu.M., Alakshin E.M., Gazizulin R.R., Klochkov A.V., Kuzmin V.V., L'Vov V.S., Tagirov M.S., *Phys. Rev. Lett.* **108**, 177002 (2012).

[6] Alakshin E.M., Bunkov Yu.M., Gazizulin R.R., Klochkov A.V., Kuzmin V.V., Rakhmatullin R.M., Sabitova A.M., Safin T.R., Tagirov M.S., *Appl. Magn. Reson.* **44**, 595 (2013).

[7] Demokritov S.O., Demidov V.E., Dzyapko O., Melkov G.A., Serga A.A., Hillebrands B., Slavin A.N., *Nature* **443**, 430 (2006).

[8] Borovik-Romanov A.S., Bunkov Yu.M., Dmitriev V.V., Mukharskiy Y.M., Sergatskov D.A., *Phys. Rev. Lett.* **62,** 1631 (1989).

[9] A.S. Borovik-Romanov, Yu.M. Bunkov, V.V. Dmitriev, Yu.M. Mukharskiy, K. Flahbart, *Sov. Phys. JETP*. **61**, 1199 (1985).

[10] S. Autti, Yu.M. Bunkov, V.B. Eltsov, et al., *Phys. Rev. Lett.* **108**, 145303 (2012).

[11] R.R. Gazizulin, Yu.M. Bunkov, V.L. Safonov, JETP Lett. **102**, 766 (2015).

Superconducting fluctuations above critical temperature in the $Bi_2Sr_2Ca_{1-x}Y_xCu_2O_8$ single crystals

I.I. Gimazov[1,2], V.O. Sakhin[2], Yu.I. Talanov[2]

[1]Kazan (Volga Region) Federal University, 420008, Kremlevskaya, 18, Kazan, Russia
[2]Zavoisky Physical-Technical Institute, 420029, Sibirsky tract, Kazan, Russia

e-mail: ubvfp94@mail.ru

High temperature superconductors (HTS) differ significantly from low-temperature superconductors, which are described by the BCS theory. One of the main differences is the existence of pseudogap state above the critical temperature. As a consequence, the transition from a normal state to a superconducting one occurs in several stages: initially, at $T = T^*$ the pseudogap state with uncorrelated Cooper pairs is set; then, with lowering a temperature down to critical temperature T_c the phase coherence emerges, that results in the vanishing of a resistivity and the appearance of the Meissner screening currents. Close to T_c the fluctuations of superconducting order parameter (SOPF) exert an influence on all processes in a superconductor. Therefore, the information about SOPF will be useful upon improving the critical parameters of HTS materials.

In this work in order to obtain information about superconducting fluctuations, we use a combination of three experimental methods: the measurement of resistance, AC susceptibility (χ' and χ'') and a non-resonant microwave absorption (MWA). Each of these methods is based on a certain physical phenomenon. The diamagnetic susceptibility is determined by the screening currents (Meissner effect). Zero resistivity is due to the emergence of superconducting channels. MWA is determined by the sample conductivity as well. However, as the measurements are made at high frequencies, they allow us to detect and to study the superconducting fluctuations.

The objects of study were single crystals $Bi_2Sr_2CaCu_2O_8$ doped with yttrium ions. Changing the concentration of yttrium allows us to vary the density of charge carriers (holes). In the absence of yttrium sample has a concentration of carriers above the optimum level (overdoped sample, OD). Upon increasing the yttrium concentrations, the density of charge carriers decreases, and the optimally doped samples (OP) are obtained. Further yttrium addition results in underdoped samples (UD).

The temperature dependence of the susceptibility of three samples with different concentrations of charge carriers is shown in fig.1. At a certain temperature susceptibility becomes negative and then it increases in absolute value. As mentioned above, it is due to the occurrence of the screening currents. This sudden change in susceptibility allows us to determine the critical temperature of a superconductor. It is seen that as the yttrium concentration increases (decreasing density of carriers), the transition temperature decreases. The same behavior of the transition temperature can be detected by measuring the MWA. This dependence is shown in fig.2.

The temperature dependence of MWA is determined by the changing conductivity of the sample. But when we get the transition temperature from high temperatures, we find an unusual maximum, which is absent in the temperature dependence of the resistance. There is a hypothesis that this maximum is due to the fluctuations influence on the microwave absorption. These fluctuations lead to an increase in conductivity in CuO_2 planes. At the same time the density of normal (unpaired) carriers decreases and the resistivity in the direction perpendicular to the CuO_2 layers increases. This leads to that the skin depth increases, and

therefore the MWA increases. Thus superconducting fluctuations manifest themselves in the form of the MWA peak near the critical temperature.

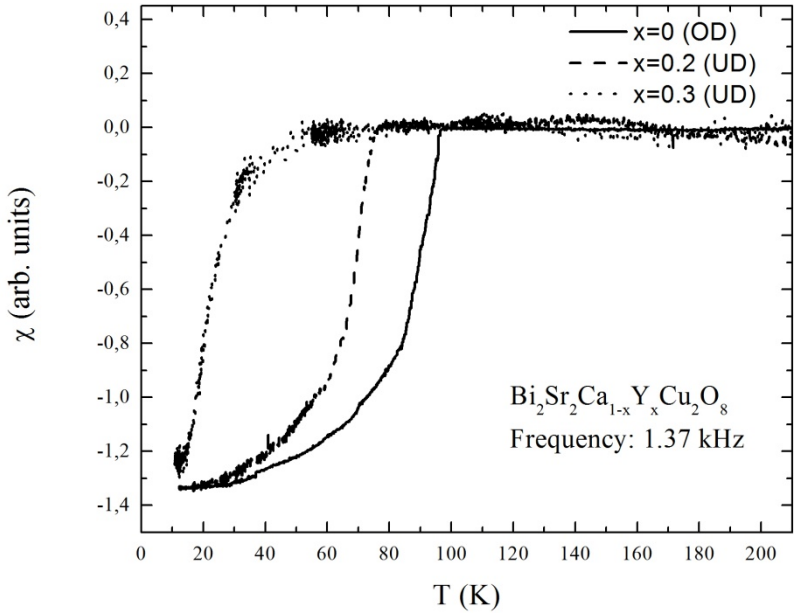

Fig.1. Temperature dependence of the AC suscep-tibility for samples with different carrier density.

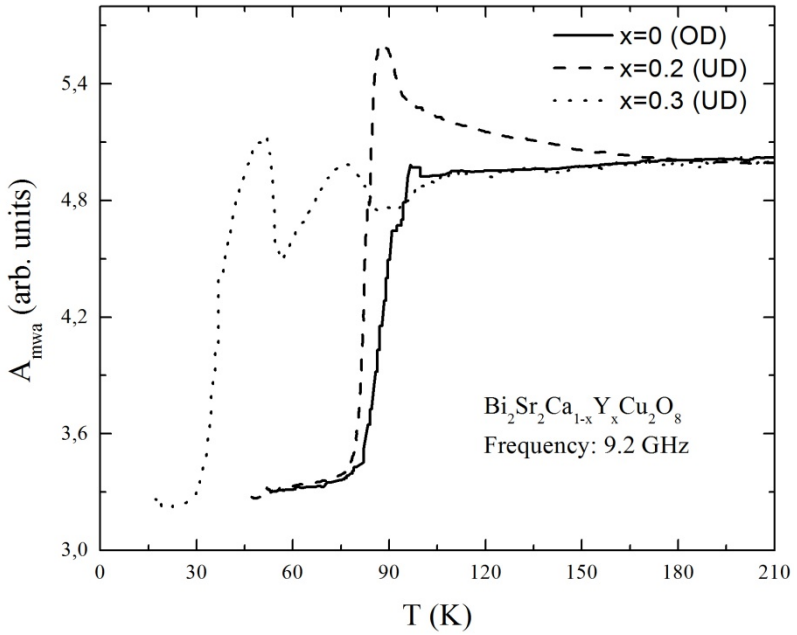

Fig.2. Temperature dependence of MWA for samples with different carrier density.

As one can see the temperature of transition from the superconducting state to the normal one obtained from the susceptibility measurement differs from the transition temperature from MWA. For one of the samples these relationships are shown in fig.3 along with the temperature dependence of the resistance. The transitions obtained from the resistivity and MWA are observed at about the same temperatures, because MWA is due to the conductivity. Susceptibility is determined by shielding currents, therefore it requires the formation of the bulk Meissner phase. It appears at lower temperature than the temperature of occurrence of the superconducting channels.

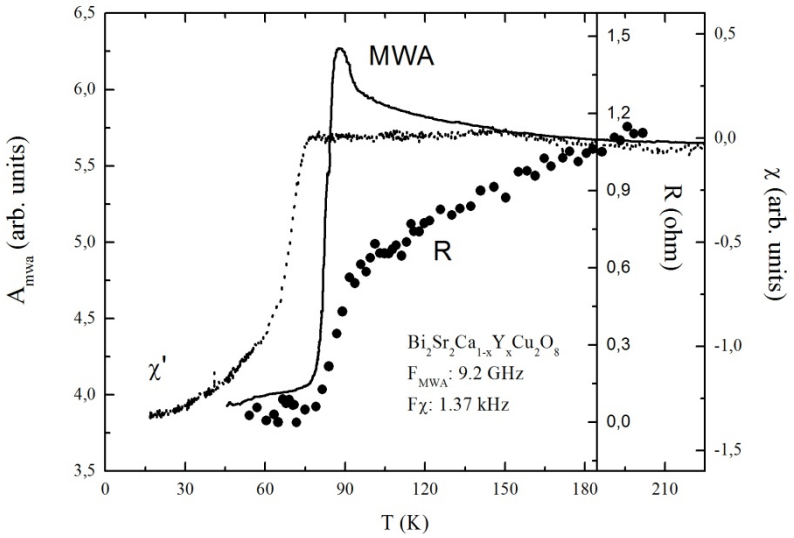

Fig.3. Temperature dependence of the susceptibility, resistivity and MWA (x = 0.2).

To summarize the results, we draw the superconducting transition temperature and the superconducting fluctuations appearance temperature on a phase diagram of $Bi_2Sr_2CaCu_2O_8$ (fig.4). This phase diagram shows the dependence of the transition temperatures on the concentration of carriers. As one can see, the superconducting transition temperature obtained from the susceptibility measurements is in good agreement with published data [1]. For a low concentration of charge carriers the boundary of the fluctuation region (black circles in fig.4) is consistent with data from measurements of the Nernst effect [1]. For concentrations more than optimally doped we can see a significant difference. However, our measurements reflect better the trend of the fluctuation region with the change of the hole concentration, discovered in studies using tunneling spectroscopy [2]. Namely, as the concentration of charge carriers increases, the effect of the superconducting order parameter fluctuations is reduced.

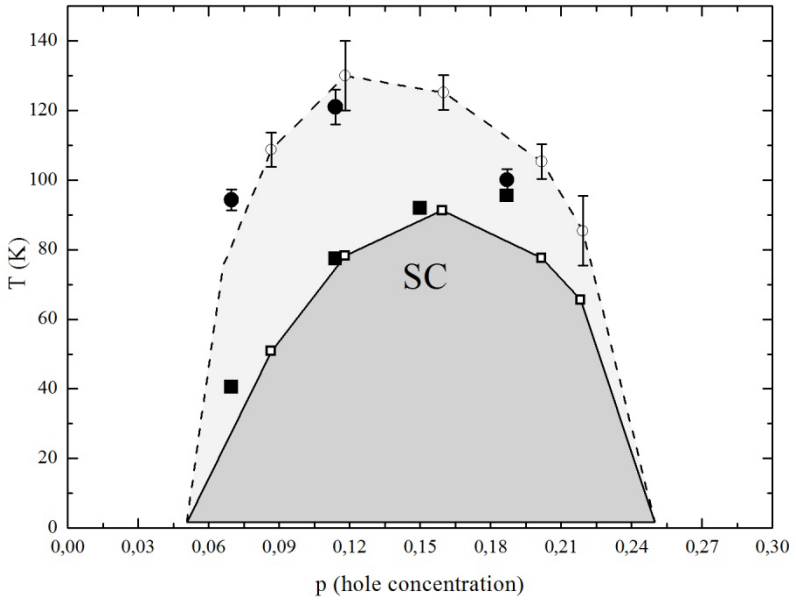

Fig.4. The phase diagram of the $Bi_2Sr_2CaCu_2O_8$ superconductor.
○ – T_f (Y.Wang et al.), ■ – $T_c(\chi_{ac})$, ● – T_f (MWA), □ – T_c (Y.Wang et al.)

References

[1] Yayu Wang *et al*. Phys. Rev. B 73, 024510 2006

[2] K. K. Gomes *et al*. Nature 447, 569 (2007)

Spin kinetics research of ^{3}He in contact with Al_2O_3 ordered aerogel

E.M. Alakshin[1], A.V. Klochkov[1], V.V. Kuzmin[1], K.R. Safiullin[1], A.A. Stanislavovas[1], M.S. Tagirov[1,2]

[1]Kazan (Volga region) Federal University, Kazan, 420008 Russia
[2]Institute for Perspective Studies, Academy of Sciences, Republic of Tatarstan, Kazan, 420011 Russia

e-mail: hectkctk@yandex.ru

Aerogels are materials with mechanical properties of solids but have a very low density. As usually pores occupy a 90 – 99% of the aerogel volume, they are used as detectors of Cherenkov radiation. Also, due to very low thermal conductivity, the aerogels are used as thermal insulation systems, applicable including space technologies. The specific porosity of these materials allows to create the electric double layer capacitors (EDLC) [1]. In addition, aerogel is a model system for studying the mechanisms of nuclear magnetic relaxation of the ^{3}He nuclei. It is known that the aerogel has affects on certain properties of ^{3}He nuclei at very low temperatures. In present work was carried out study the mechanisms of nuclear magnetic relaxation of the ^{3}He nuclei in contact with the ordered aerogel sample (published in [2]).

Ordered Al_2O_3 aerogel (Nafen-90, ANF Technology Ltd, Tallinn, Estonia) was used as a sample in the present work. The SEM image of used sample is shown in fig.1. The main parameters of this sample are: 0.5 cm diameter, 2.5 cm length, 8 nm fibers diameter, 90 mg/cm^3 density, and the distance between fibers of 50 – 80 nm.

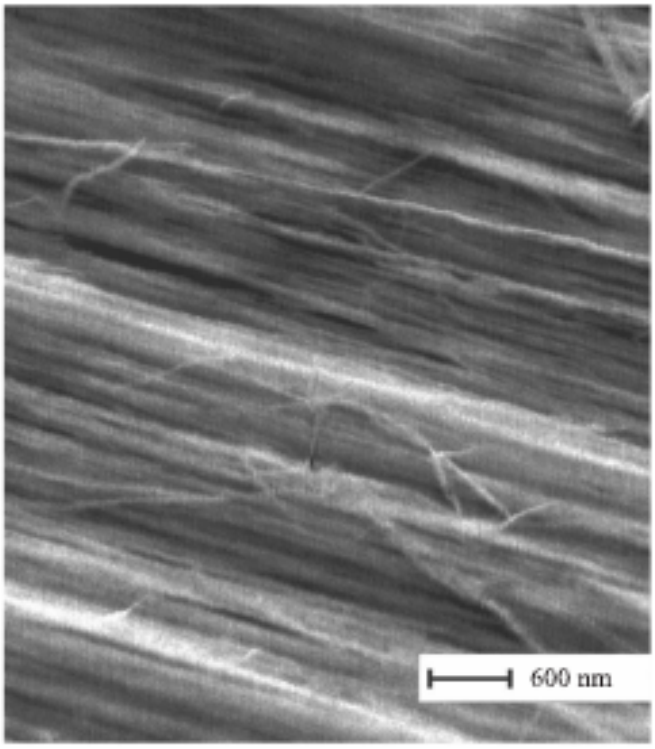

Fig.1. The image of Al_2O_3 “Nafen-90” ordered aerogel (ANF Technology Ltd, Tallinn, Estonia), obtained by scanning electron microscopy.

NMR experiments were carried out on a homebuilt pulsed spectrometer described by Alakshin E. M. et al in [3]. The resonance circuit tuning and matching scheme with a “hot”

capacitor was used to measure relaxation times at various frequencies. According to this scheme only the detection coil is located inside the ^{4}He cryostat. In our experiments magnetic field was varied in the range of 100 – 600 mT. The temperature of 1.6 – 4.2 K was obatained by helium vapor pumping. The spectrometer scheme is presented in fig.2.

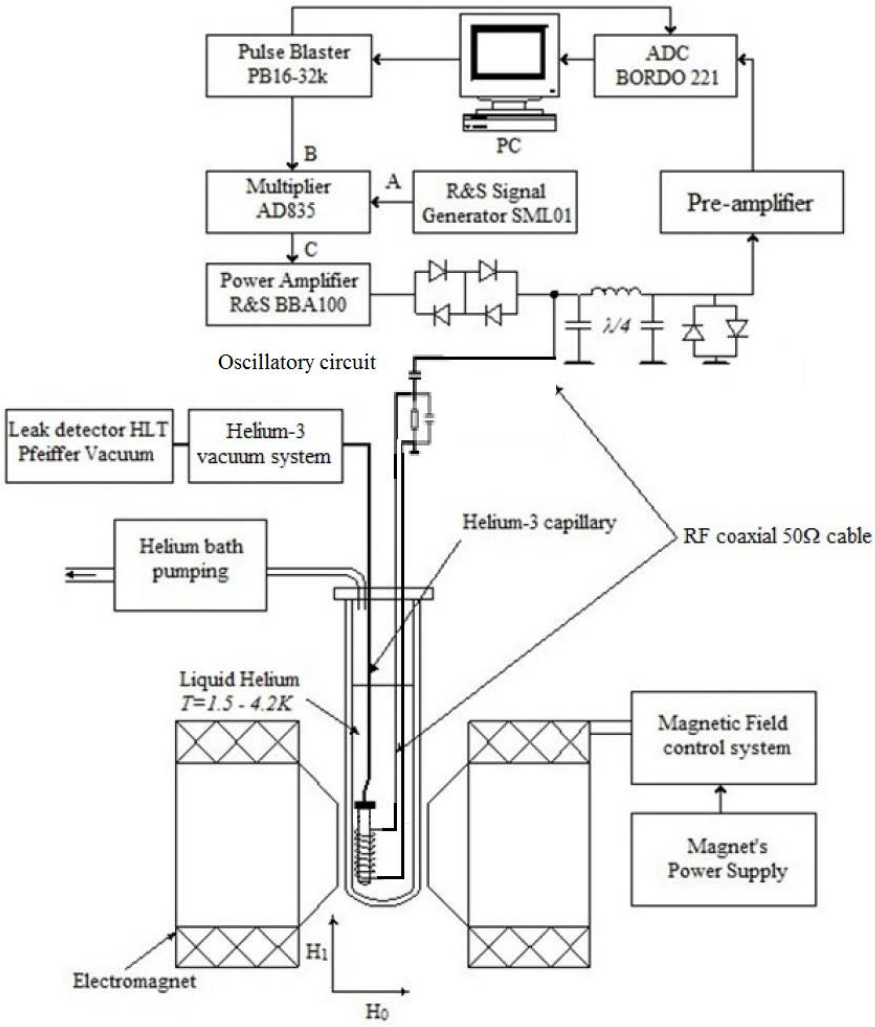

Fig.2. The scheme of used pulsed NMR spectrometer [3].

Preliminary experiments were carried out in order to determine the ^{3}He adsorbed volume on the sample surface. The pressure dependence of the 3He gas on its amount in the experimental cell was measured by a Pfeiffer Vacuum RPT 200 AR pressure detector at 4.2 K and 1.6 K temperatures. The obtained ^{3}He volume of adsorbed layers are following: 6.1 cc at 4.2 K and 12.2 cc at 1.6 K.

In this work the spin-lattice relaxation time T_1 of ^{3}He nuclei was studied by pulsed NMR methods in contact with the ordered Al_2O_3 aerogel.

The measured ^{3}He spin-lattice time T_1 dependence on amount of ^{3}He in the experimental cell is shown in fig.3 (f_0 = 16.32 MHz, B_0 = 0.5 T).

Earlier similar experiments have been performed using the chaotic SiO_2 aerogel in S.A. Altshuler laboratory [4-6]. These experiments confirm the decisive role of the adsorbed layer in the process of relaxation of gaseous and liquid ^{3}He. Our results show that during the completion of the adsorbed ^{3}He layers on the Al_2O_3 aerogel surface, the dependence of the ^{3}He spin-lattice relaxation time T_1 on ^{3}He amount behaves in the same way as for case of the

silicate aerogel (point A of fig.3). But in the gas phase that dependence disappears for a wide range of ^{3}He amount. This indicates on the presence of an additional relaxation channel.

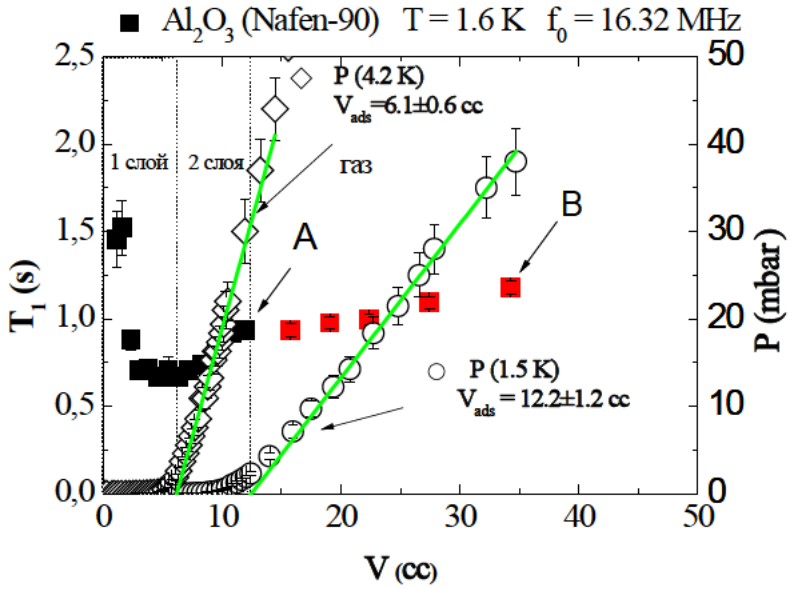

Fig.3. The dependence of spin-lattice time T_1 on the amount of the ^{3}He (n.c.) in Al_2O_3 aerogel (▪).The dashed line separates the filling region of the first and the second adsorbed layers. The pressure dependence on amount of ^{3}He in Al_2O_3 ordered aerogel at the 4.2 K (◊) and 1.6 K (○) (green lines – approximations of the linear region of the dependence performed in order to determine volumes of adsorbed layers).

To test this hypothesis the following experiment was performed: the sample surface was covered by two layers of ^{4}He (16 cc) at the 4.2 K temperature. Then the temperature was lowered to 1.6 K, the experimental cell was filled by ^{3}He gas (38 mbar) and the frequency dependence of ^{3}He gas T_1 relaxation time was measured. The obtained frequency dependence is shown on fig.4. The one obtained earlier for the ^{3}He adsorbed layer is also presented on fig.4 for comparison.

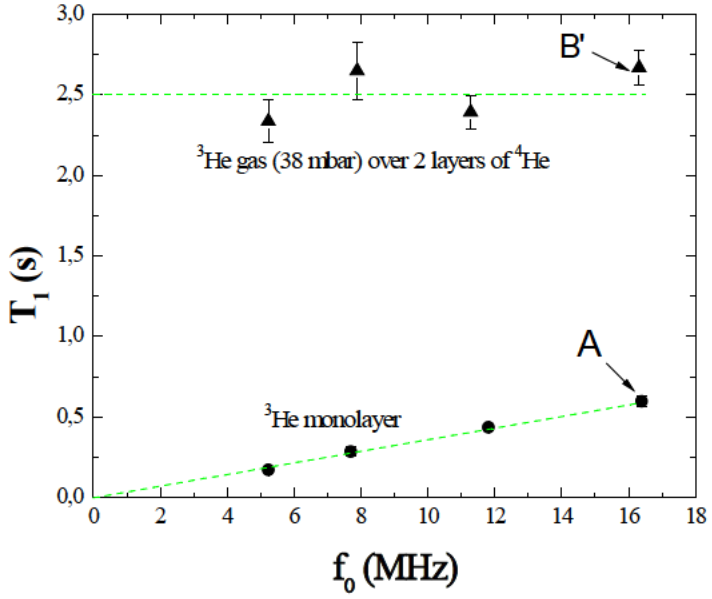

Fig.4. Frequency dependence of the ^{3}He spin-lattice relaxation time in the Al_2O_3 aerogel: ● – adsorbed layer of ^{3}He (16 cc), ▲ – gaseous ^{3}He (38 mbar) at coating the sample surface with two layers ^{4}He.

The ^{3}He spin-lattice relaxation time T_1 in the ^{3}He adsorbed layer linearly changes with the frequency. This is typical for surface relaxation mechanism of ^{3}He described in [7]. In contrast to the adsorbed layer, the spin-lattice relaxation time of gaseous ^{3}He after sample coating with ^{4}He is independent of frequency. This means that sample coverage by ^{4}He completely excluded the surface channel of ^{3}He relaxation. Also after coating the surface of the aerogel by two layers of ^{4}He, relaxation time of ^{3}He gas does not increase much (about 2 times – point B on fig.3 and point B' on the fig.4). In similar experiments on SiO_2 the value of the T_1 relaxation time values of ^{3}He nuclei increased by more than an order of magnitude [5,6]. Thus, the one can conclude that our experimental results confirm that the additional relaxation mechanism is not associated with the fast exchange between the adsorbed and gas phases of ^{3}He.

The EPR study of the sample revealed the presence of two types of paramagnetic centers near g-factor 2 with the concentration of about $2*10^{16}$ spin/g in it [8]. Probably mechanism of the relaxation of gaseous ^{3}He in fluctuating inhomogeneous magnetic fields created by paramagnetic centers occurs in our experiments. We have to note that intrinsic paramagnetic centers were not observed in SiO_2 aerogels.

However the experimental data can not uniquely confirm or deny the influence of paramagnetic centers on the relaxation of ^{3}He. It is also possible that the unique ordered structure of the aerogel influence on the relaxation of ^{3}He. Further studies are necessary to build a complete model of the ^{3}He nuclear magnetic relaxation in this type of aerogel.

The current state of recent studies will be presented.

References

[1] J. M. Miller, B. Dunn, T. D. Tran, R. W. Pekala, J. Electrochem. Soc. **144**, 309 (1997).

[2] A.V. Klochkov, A.A. Stanislavovas, V.V. Kuzmin, K.R. Safiullin, M.U. Zakharov, M. S. Tagirov, JETP lett. **104**, 325 (2016).

[3] E.M. Alakshin, R.R. Gazizulin, A.V. Klochkov, V.V. Kuzmin, A.M. Sabitova, T.R. Safin, M.S. Tagirov, Magnetic Resonance in Solids **15**, 1 (2013).

[4] A.V. Klochkov, V.V. Kuzmin, K.R. Safiullin, M.S. Tagirov, D.A. Tayurskii, N. Mulders, JETP Lett. **88**, 823 (2008).

[5] A. Klochkov, V. Kuzmin, K. Safiullin, M. Tagirov, A. Yudin, N. Mulders, J. Phys.: Conf. Ser. **150**, 1 (2009).

[6] E.M. Alakshin, R.R. Gazizulin, A.V. Klochkov, V.V. Kuzmin, N. Mulders, M.S. Tagirov and D.A. Tayurskii, JETP Lett. **93**, 223 (2011).

[7] B.P. Cowan, Journal of Low Temperature Physic **50**, 135 (1983).

[8] G.V. Mamin, S.B. Orlinsky, A.A. Rodionov, M.S. Tagirov, JETP Lett. **102**, 714 (2015).

Synthesis and study of the magnetic properties of micro- and nanosize powders $LiTbF_4$ and TbF_3

D.S. Nuzhina, E.M. Alakshin, A.V. Klochkov, S.L. Korableva, I.V. Romanova, M.S. Tagirov

Kazan Federal University, 420008, Kremlevskaya, 18, Kazan, Russia

e-mail: nuzh.darya@gmail.com

Introduction

Due to their unique physical and chemical properties nanosized particles have attracted increasing interest [1]. The complex fluorides $LiReF_4$ (Re = rare earth ion) present a class of crystal materials as model objects in physics of dipolar magnets. Nanocrystals of rare-earth tetrafluorides compounds with a controlled size, shape, composition and surface have specific optical, electronic, magnetic and catalytic properties that fundamentally important for industrial use [2]. Trifluoride exhibit distinct magnetic properties at low temperatures and interested as model for the theoretical study of magnetic ordering in competition dipole-dipole and exchange interactions [3].

For the first time the transition to the ferromagnetic state in $LiTbF_4$ crystal along easy magnetic axis was found in [4] from the temperature dependence of the longitudinal magnetic susceptibility. The $LiTbF_4$ is dipole Ising dielectric ferromagnet below the T_C (2.89 K) temperature [5].

The compound TbF_3 is a dielectric ferromagnet. The phase transition TbF_3 single crystal from the paramagnetic to the ferromagnetic state occurs when the temperature is lowered to $T_C = 3.95$ K [5]. At low temperatures ($T < T_C$) magnetic moments of ions Tb^{3+} (~9 μ_B) in TbF_3 single crystal ordered in two magnetically nonequivalent sublattices due classical dipole-dipole interaction between the ions of terbium, which dominates in the system above the magnetic exchange interaction.

Syntesis of micro- and nanoparticles powders

The samples of $LiTbF_4$ and TbF_3 were synthesized using following technologies [2,6-10].

Sample 1: $LiNO_3 + Tb(NO_3)_3 + 4NH_4F \xrightarrow{400\ C,\ 4ч} LiTbF_4 + 4NH_4NO_3$.

Sample 2: $LiOH \cdot 3H_2O + Tb(NO_3)_3 \cdot 5H_2O + 4NH_4F \xrightarrow{300\ C,\ 3ч,\ CF_4} LiTbF_4 + 4NH_4NO_3 + 8H_2O$.

Sample 3: $Tb(NO_3)_3 \cdot 5H_2O + 3NaF \longrightarrow TbF_3 + 3NaNO_3$.

The X-ray analysis of synthesized samples is shown in fig.1.

Phase ratio of $LiTbF_4$ и TbF_3 in samples 1-2 was refined using X-ray diffraction.

The chemical compositions of the synthesized samples are:

Sample 1 — TbF_3 (81.2 ± 0.4%) + $LiTbF_4$ (6.9 ± 0.1%) + $LiNO_3 \cdot H_2O$(11.9 ± 1.1%),

Sample 2 — $LiTbF_4$ (79.9 ± 0.7%) + TbF_3 (20.0 ± 0.5%),

Sample 3 — TbF_3(99 ± 1%).

Dimensions of powders particles were determined using the dynamic and static light scattering spectrometer for registration nanoparticles size and composition Photocor Complex (table 1).

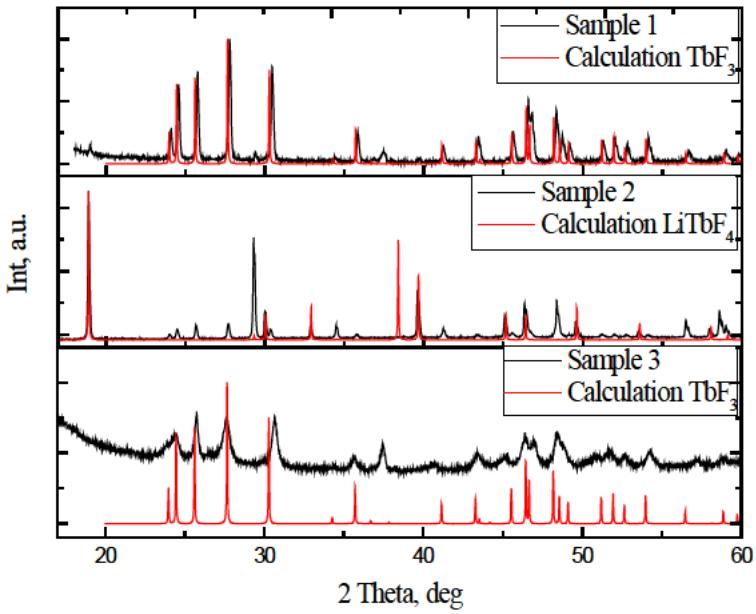

Fig.1. X-ray analysis of samples 1-3

Table 1. Characteristic size of samples 1-3

Sample	Characteristic size (diameter)
$LiTbF_4$(79.9%)+TbF_3(20%)	20 mkm
$LiTbF_4$(6.9%)+TbF_3(81.2%)	1,5 mkm
TbF_3	585 nm

Study of magnetic properties, discussion and results

The temperature dependencies of magnetic susceptibility of the all synthesized samples was measured on PPMS in magnetic fields with a strength of 100 Oe and 1 T, at temperatures of 2 – 300 K.

The temperature dependence of the derivative of magnetic susceptibility of the sample 1 is shown on fig.2. There are two phase transitions at temperatures $T = 2.8$ K and $T = 3.76$ K, which correspond to the Curie temperature of the transitions to a ferromagnetic state for $LiTbF_4$ and TbF_3 single crystals. The red curve on fig.2 presents the dependence of the derivative of magnetic susceptibility of single crystal $LiTbF_4$ in a magnetic field $B \| c$. In the measurement of the magnetization of the powder all possible directions of arrangement of the particles along the direction of the external magnetic field can be equivalent, which would reduce the total magnetization.

The temperature dependence susceptibility of the sample 2 is shown on fig.3 (black points). There is only one transition to a magnetically ordered state at $T = 3.78$ K, referring to the ferromagnet TbF_3. Content $LiTbF_4$ of the sample is too low to obtain the temperature transition to a magnetically ordered state of $LiTbF_4$.

Fig.4 shows the measured temperature dependence of the susceptibility of nanosized powder TbF_3 and data from [3] — the temperature dependence of the susceptibility of the powder TbF_3 and single crystal TbF_3 in different directions of crystal lattice — $\chi \| a$, $\chi \| b$, $\chi \| c$. Also for comparison with nanosized powder TbF_3, there is given data on the temperature dependence of the magnetic susceptibility in the micropowder in external magnetic field induction $B_0 = 0.01$ T (blue points).

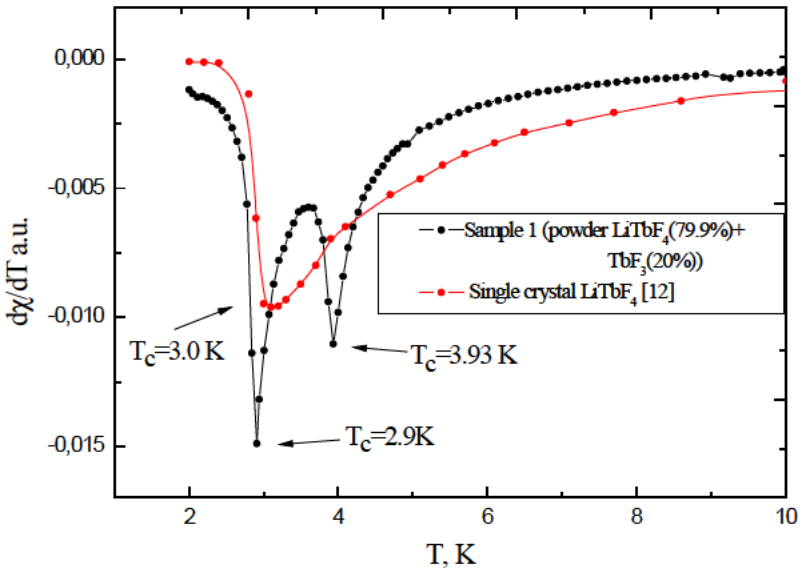

Fig.2. Dependence of the derivatives of magnetic susceptibility of temperature in $LiTbF_4$ (79.9 ± 0.7%) + TbF_3 (20.0 ± 0.5%) powder and $LiTbF_4$ single crystal, B = 100 Oe.

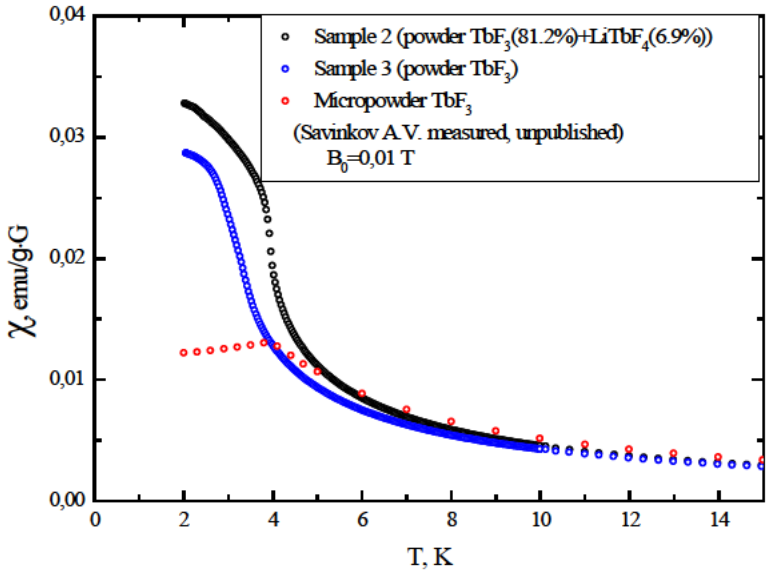

Fig.3 Temperature dependencies of magnetic susceptibility in TbF_3 and TbF_3 (81.2±0.4%)+$LiTbF_4$ (6.9±0.1%).

The magnetic susceptibility of the powder is described as , where — magnetic susceptibilities along the axes *a*, *b*, *c* [3]. This calculation is in approximately agreement with the experimental results, because it does not take into account the size and shape of the particles, as well as the parameters of the crystal field and the local magnetic fields on the Tb^{3+} ions.

Theoretical calculation of the susceptibility $\chi=M/B$, shown in fig.5 (red line). It was made taking into account all possible orientations of the external magnetic field along the crystallographic c-axis of the nanoparticle. Assuming that the angle between the *c*-axis of the lattice and the external magnetic field of α, the projection of the magnetic field on the direction of the *c*-axis lattice $B_z=B_0 cos\alpha$. The shape of the nanoparticles assumed spherical, the summation carried on sphere 360^0. The calculation was performed using the Matlab software:

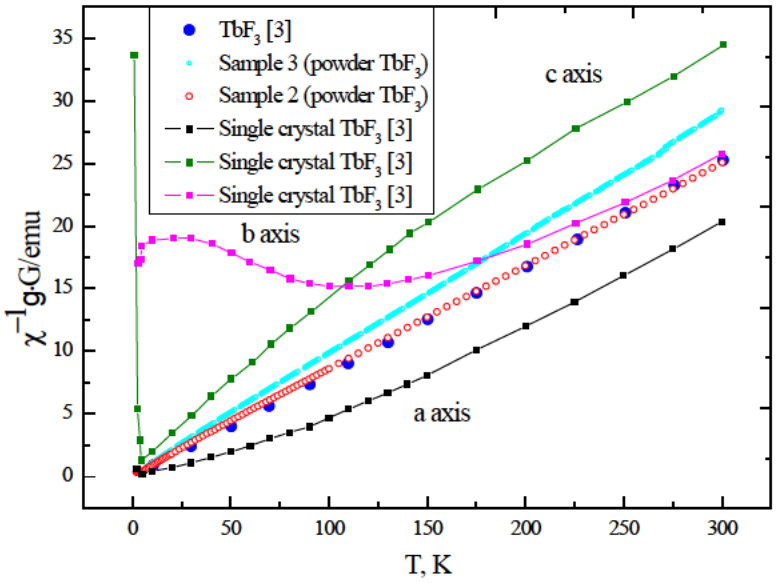

Fig.4. Temperature dependencies of magnetic susceptibility in TbF_3.

$$M_z = B_z\left[\lambda\left(\frac{th(\delta/2k_BT_C)}{th(\delta/2k_BT)}-1\right)+N\right]^{-1} \quad (1)$$

where M_z — magnetization along c-axis, λ — molecular field constant ($\lambda = 5.23 \pm 0.56$), δ — initial splitting quasidoublet ($\delta = 1$ cm^{-1}), N — demagnetization factor (N=4 /3), B_z — external magnetic field, k_B — Boltzmann's constant, T — temperature magnetic ordering [2].

The measured temperature dependences of the magnetization in sample 1 and single crystal $LiTbF_4$ at $B_0 \| a$ and $B_0 \| c$ in external magnetic field ($B_0 = 1$ T) are presented on the fig.5.

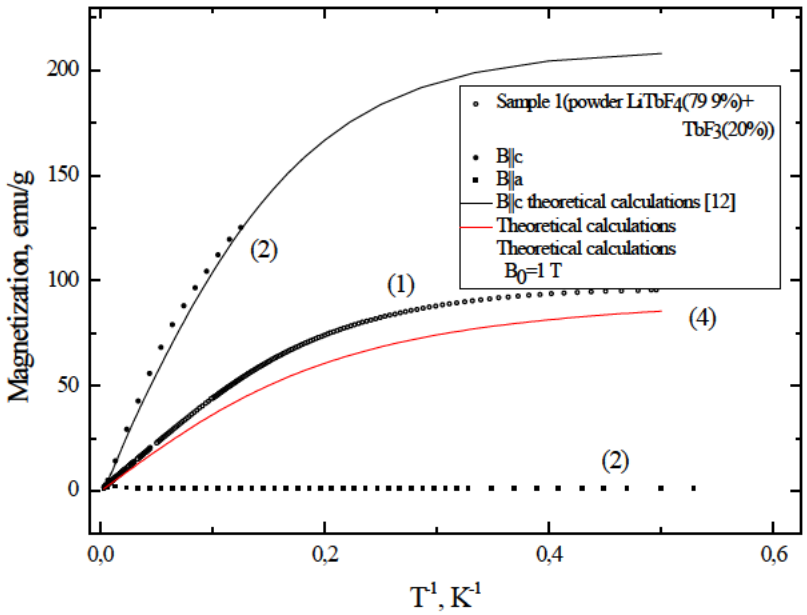

Fig.5. Temperature dependence of the magnetization in $LiTbF_4$ ($79.9 \pm 0.7\%$)+TbF_3 ($20.0 \pm 0.5\%$) and $LiTbF_4$ single crystal, $B = 1$ T.

Curve 4 in fig.5 shows the calculations taking into account all possible orientations of the external magnetic field along the crystallographic c-axis of the nanoparticle. The discrepancy between the theoretical calculations in this case can also be explained by the fact

that the calculation has not been considered TbF_3 particle content of a sample, and particle shape.

The fact that the values of magnetization were calculated without taking into account the content of TbF_3 in the compounds and particles shapes, can explain the difference between experimental results and theoretical description. This approximation describes the temperature dependence of the susceptibility for samples in the paramagnetic phase, above the transition temperature to magnetic ordered state.

The unusual behavior of the magnetization and magnetic susceptibilities in micro- and nanosized powders $LiTbF_4$ and TbF_3 should be considered in detail.

Acknowledgments

This work was partially supported by RFBR grant № №15-02-06990a

References

[1] Kuznetsov S. V. et al. Russian chemical reviews.V.75. №.12. P.1065-1082 (2006).

[2] Du, Y. P., Zhang, Y. W., Sun, L. D., & Yan, C. H. Dalton Transactions, (40), 8574-8581 (2009) .

[3] L.M. Holmes, H.J. Guggenheim. Journal de Physique. V.32. P. 501-502 (1971).

[4] L.M. Holmes, T. Johansson. Solid State Commun. V.12. I.10. P.993-997 (1973).

[5] J. Als-Nielsen, L.M. Holmes, F.K. Larsen, H.J. Guggenheim. Phys. Rev. B, 12,191 (1975).

[6] Fedorov, P.P., Kuznetsov, S.V., Voronov, V.V. et al. Russ. J. Inorg. Chem. 53(11), 1681 (2008).

[7] Chunhua Lu, et al. Materials Research Bulletin. 46(2), 216-222 (2011).

[8] Shi Chen, Shiwei Wang, Jian Zhang, Liqiong An. Journal of Nanoscience and Nanotechnology.V.9.P.1942–1946 (2009).

[9] Chunxia Li, Jun Lin. J. Mater. Chem. V.20. P. 6831-6847 (2010).

[10] M.F. Joubert, B. Jacquier, R. Moncorge. Phys. Rev. B. V.28. P.3725 (1983).

[11] I.V. Romanova, B.Z. Malkin, I.R. Mukhamedshin, H. Suzuki & M.S. Tagirov. Physics of the Solid State, 44(8), 1544-1549 (2002).

Investigation magnetic properties HgCdTe:Ag and HgSe:Cr

A.V. Shestakov[1], I.I. Fazlizhanov[1,2], I.V. Yatsyk[1,2], M.I. Ibragimova[2], V.A. Shustov[2], R.M. Eremina[1,2]

[1]Kazan (Volga Region) Federal University, 420008, 18 Kremlyovskaya St., Kazan, Russia
[2]Kazan E.K. Zavoisky Physical-Technical Institute, 420029,10/7 Sibirsky tract, Kazan, Russia
e-mail: aleksey665@gmail.com

The mercury chalcogenides HgSe and HgTe in the zinc-blende (ZB) structure belong to a group of unique materials exhibiting the so-called inverted band structure [1] and it are semimagnetic semiconductors n-type (AII BVI). Compound HgCdTe is the most widely used semiconductor with a variable band gap [2]. Ion implantation modifies the carrier concentrations at the introduction of impurities in the surface layer that greatly affects the skin effect. In conductive media, microwave absorption is determined by the skin effect. In this case, considerable importance is the condition of the surface of the sample. The aim of our work is the study of the magnetic and transport properties of implanted silver ions $Hg_{0.76}Cd_{0.24}Te$ by magnetic resonance method. In these samples an oscillation of the conductivity can be observed, at low temperatures in the presence of very intense magnetic fields, known as Shubnikov – de Haas effect (SdH). The SdH effect is a macroscopic manifestation of the inherent quantum mechanical nature of matter.

The samples were grown by continuous feeding of the melt. Grown crystal $Hg_{0.76}Cd_{0.24}Te$ had n-type conductivity with concentration of $10^{16} – 10^{17}$ cm^{-3}, the sample was subjected to ion implantation by ions of Ag^+ ion on ILU-3 accelerator. After implantation the sample was annealed in a sealed quartz tube in a saturated mercury atmosphere at a temperature of 300°C for 20 days. Subsequent annealing of the crystal in the atmosphere of mercury ions the conductivity is inverted to p-type with carrier concentration of $\approx 10^{14}$ cm^{-3}.

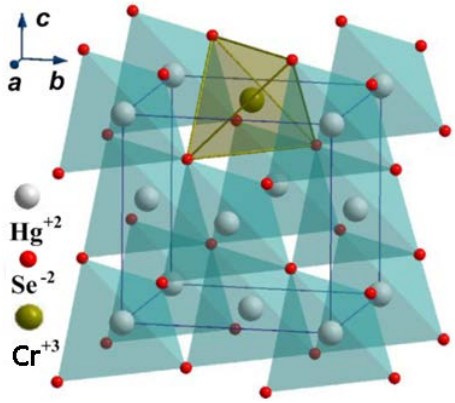

Fig.1. The crystal structure of HgSe:Cr. Tetrahedral mercury complex with chromium ion is highlighted [3]

Spectra investigations were performed on a spectrometer Varian E12 at X-band frequency (9.36 GHz) at the temperature 4.2 K and at the magnetic field from 0 to 10^4 Oe. The experiments with different orientations of the sample relative direction field and with difference microwave power magnetic field were performed in three planes, perpendicular to the selected axis (0) in the plane of the axis (90), and at an angle of 45 degrees to the selected direction.

The angular dependencies of spectra of $Hg_{0.76}Cd_{0.24}Te:Ag^+$ and HgSe:Cr single crystals at 4.2 K are shown in fig.2.

Strong Shubnikov – de Haas (SdH) oscillations were observed in the derivative of microwave absorption (f = 9.4 GHz) in the of $Hg_{0.76}Cd_{0.24}Te:Ag^+$ and $Hg_{0.76}Cd_{0.24}Te:Ag^+$ using electron paramagnetic resonance spectroscopy at low temperatures (4.2 – 20 K) and in the magnetic field up to 10 kOe. The samples of 2×2×2 mm^3 were placed in the cavity and the

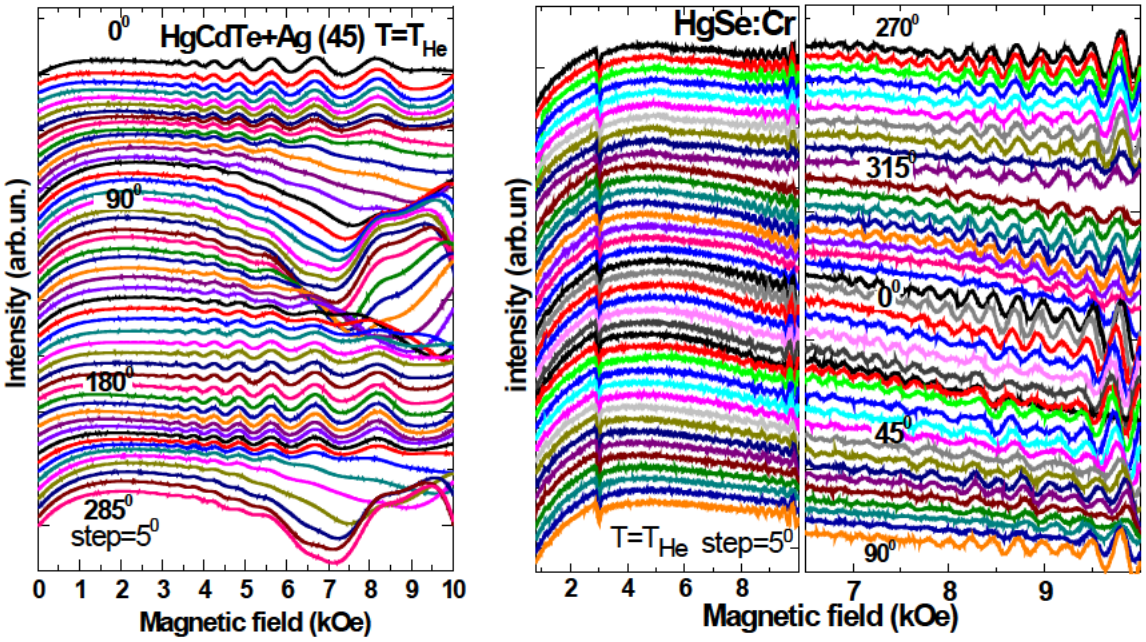

Fig.2. Angular dependencies of microwave power derivative in HgCdTe:Ag^+ (on the left) and in HgSe:Cr (on the right).

outside magnetic field was applied. The microwave absorption power derivative (dP/dH) was registered in the experiments. Microwave current induces in the microwave field. Oscillations of the microwave power derivative correspond to the transverse magnetoresistance $\Delta\rho/\rho$. The fitting dependence of the period of high-frequency oscillations is described by formula

$$\Delta H = A \cdot H^2 + C, \qquad (1)$$

where H — external magnetic field, $A = 26{,}6\ 10^{-6}$, $C = 55$ (for HgCdTe:Ag^+) — fitting parameters. Up to experimental error obtained parameters A and C are the same for all directions of the external magnetic field relative to the crystallographic axes of the crystal (see fig.3).

Fig.4 shows the microwave absorption power derivative as a function of the inverse applied magnetic field. The oscillation periods $\Delta(H^{-1})$ in the reverse magnetic field are equal

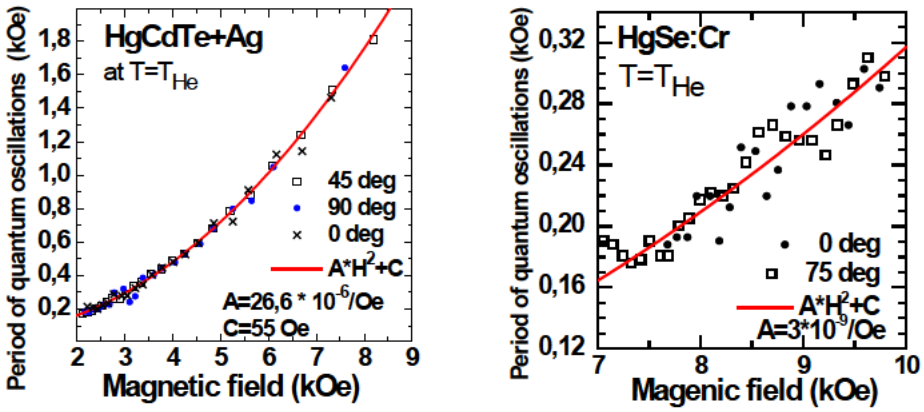

Fig.3. The dependence of the period of quantum oscillations from the applied magnetic field in HgCdTe:Ag^+ (on the left) and in HgSe:Cr (on the right).

2,8 – 3,23·10^{-5} Oe^{-1}, the carrier concentration n_s has been determined according to formula (2) [4] in skin layer:

$$n_s = \frac{e}{\pi\hbar\Delta(H^{-1})} = (4.48 \div 5.17)\cdot 10^{21}\,\text{cm}^{-2}. \quad (2)$$

The oscillation periods $\Delta(H^{-1})$ in spectrum of HgSe:Cr are equal 0,305 – 0,340 10^{-5} Oe^{-1} in the reverse magnetic field, the carrier concentration $n_s = (42 \div 47)\cdot 10^{21}\,\text{cm}^{-2}$.

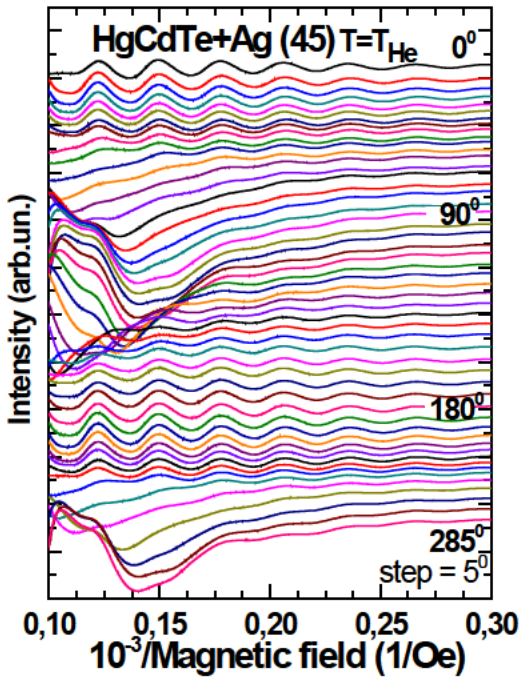

Fig.4. Angular dependence of SdH oscillations of the microwave power derivative in the reverse magnetic field. T = 4.2 K.

Conclusions

The implantation of silver and chromium ions leads to a increase of carrier concentration on surface and observation the quantum oscillations in the spectrum of magnetic resonance.

References

[1] A.Veynger, A.Zabrodskii, T. Tisnek, G. Biskupská, *Phys. and Tech. Semiconductor (FTP)*, **32**, 557-563 (1998).

[2] L. Winterfeld, L.A. Agapito, J. Li, N. Kioussis, P. Blaha, Y.P. Chen, *Phys. Rev. B*, **87**, 075A. 143 (2013).

[3] K. Lamonova, B. Bakirov, I. Ivanchenko, N. Popenko, E. Zhitluhina, V. Burhovetsky, S. Eagle, Yu. Pashkevich, *LowTempPhys*, **40**, 842-850 (2014).

[4] N. Popenko, A. Bakirov, I. Ivanchenko, A. Bludov and V. Pascenco, *JETF Letters*, **100**, 247-322 (2014).

Ab initio investigations of double rare earth fluorides under pressure

A.V. Petrova[1], O.V. Nedopekin[1], D.A. Tayurskii[1,2]

[1]Institute of Physics, Kazan Federal University, 420008, Kremlevskaya str. 16a, Kazan, Russia.

[2]Centre for Quantum Technologies, Kazan Federal University, 420008, Kremlevskaya str. 16a, Kazan, Russia.

e-mail: Anastasia.Petrova@kpfu.ru

There is a considerable progress in the study of structural and mechanical properties pressure effect in $M\mathrm{LiF_4}$ (M — is an element belonging to the group of lanthanides) compounds. The study of $M\mathrm{LiF_4}$ systematics behavior under compression may lead to deeper understanding of phase transitions mechanisms of named materials. For example, Grzechnik et al. studied $\mathrm{GdLiF_4}$ [1], $\mathrm{YLiF_4}$ [2] and $\mathrm{LuLiF_4}$ [3] compounds by X-ray diffraction in a diamond anvil cell at room temperature under pressure. These three compounds modifications took place near the pressure of 11 GPa with different consequences.

For investigation of applied pressure influence on $\mathrm{GdLiF_4}$ and $\mathrm{LuLiF_4}$ properties (structural, mechanical, electronic and vibrational) density functional theory (DFT) was used [4,5]. Ab initio calculations were performed using *Vienna Ab Initio Simulation Package* VASP 5.2 module [6] of MedeA® software package (Materials Design, S.A.R.L.). As a result of pressure influence investigation $\mathrm{GdLiF_4}$ structural decay reasons were determined. Also $\mathrm{LuLiF_4}$ second-order phase transition was proved and its direction in the $(\mathrm{LuLiF_4})_4$ unit cell was found. Coefficient at quadratic order parameter was calculated and its dependence on the pressure has been plotted indicating a phase transition at 10.5 GPa. Absence of phase transitions in the structures with symmetries $\mathrm{P2_1/c}$ and P12/c1 of $\mathrm{LuLiF_4}$ compound were proved by comparison of the enthalpy of these phases with the enthalpy of scheelite phase $\mathrm{I4_1/a}$.

References

[1] Decomposition of $\mathrm{LiGdF_4}$ scheelite at high pressures/A. Grzechnik, W.A. Crichton, P. Bouvier [et al.]//Journal of Physics: Condensed Matter. – 2004. – V. 16, no. 43. – P.7779.

[2] Scheelite to fergusonite phase transition in $\mathrm{YLiF_4}$ at high pressures/A. Grzechnik, K. Syassen, I. Loa [et al.]//Phys. Rev. B. – 2002. – V.65, no. 10. – 104102.

[3] Pressure-induced tricritical phase transition from the scheelite structure to the fergusonite structure in $\mathrm{LiLuF_4}$/A. Grzechnik, K. Friese, V. Dmitriev [et al.]//Journal of Physics: Condensed Matter. – 2005. – V.17, no. 4. – P.763.

[4] Hohenberg, P. Density functional theory/P. Hohenberg, W. Kohn//Phys. Rev. B. – 1964.– V.136. –Pp. 864-876.

[5] Kohn, W. Self-consistent equations including exchange and correlation effects/W. Kohn, L.J. Sham//Phys. Rev. A. – 1965. – V. 140, no. 4A. – P.A1133.

[6] Kresse, G. Efficient iterative schemes for ab initio total-energy calculations using a plane-wave basis set/G. Kresse, J. Furthmuller//Phys. Rev. B. – 1996. –V.54, no.16. – P.11169.

Spin kinetics of ^{3}He in contact with detonation nanodiamonds

G.A. Dolgorukov, V.V. Kuzmin, K.R. Safiullin, A.A. Stanislavovas, A.A. Petrov, A.V. Klochkov, M.S. Tagirov

Institute of Physics, Kazan Federal University, 420008 Kazan, Russian Federation.

e-mail: Sasha_chayan@mail.ru

It is known that restricted geometrical conditions can significantly affect nuclear magnetic relaxation of ^{3}He nuclei [1,2] and this effect is a subject of many studies. The difference of the NMR relaxation processes in free and in restricted geometry liquids are connected with the fact that in bulk liquids the mechanism of relaxation is determined by the diffusion modulation of dipole-dipole interaction, but in restricted geometry only few diffusion modes are possible. Especially significant effects appear at pore size scales less than 10 nm [1].

In order to achieve restricted geometry conditions for ^{3}He nanodiamonds were chosen as a sample. The used sample consisted of 3 – 10 nm detonation diamond nanoparticles of spherical shape. We expect a typical pore sizes of order of few and of tens nanometers in our sample at high bulk density.

NMR experiments were performed using a homebuild pulsed NMR spectrometer. The main characteristics of this NMR setup are: the magnetic field varies up to 0.8 T, 3 – 50 MHz operating frequency range, and 1.6 – 300 K temperature range.

Spin-lattice relaxation time T_1 and spin-spin relaxation time T_2 were measured for ^{3}He nuclei in adsorbed, gas and liquid phases in the Larmor frequency range of 5 – 18 MHz at 1.6 K temperature. The observed T_1 values (few milliseconds) are surprisingly shorter than ones usually obtained for ^{3}He in similar experiments with various samples (few seconds) [3,4]. Measured spin-spin relaxation times T_2 of ^{3}He in nanodiamonds (~0.5 ms) is also shorter than T_2 of ^{3}He in aerogels (~5 ms). However the observed linear frequency dependence of T_1 values of ^{3}He nuclei of all helium phases qualitatively coincides with one obtained for ^{3}He in aerogels [3]. It is also found that measured T_1 values are linearly dependent on the amount of ^{3}He in the gas phase.

In the case of ^{3}He in aerogels the linear frequency dependences are explained [3] by the surface channel of relaxation that is consistent with Cowan theory [5]. In order to remove the surface relaxation we performed similar experiments on ^{3}He nuclei with a sample surface covered by two layers of nonmagnetic ^{4}He. In this conditions ^{3}He relaxation times T_1 and T_2 increased only by one order of magnitude. Thus we suggest that the relaxation process through paramagnetic centers occurs in our experiments as well. It is known from EPR studies [6] that detonation nanodiamonds contain a high number of paramagnetic centers located on nanodiamond surface.

Further experiments are required to fully understand the relaxation mechanisms that take place in this experimental system. Current results of the studies will be presented.

The work was supported by the Russian Science Foundation (project no. 16-12-10359).

References

[1] V.V. Naletov et al, JETP. **108**, 577-592 (1995)
[2] Hammel P. C. Richardson R.C., Phys. Rev. Lett. **52**, 1441-1444 (1984)
[3] A.V. Klochkov et al, JETP Letters. **88**(12), 823-827 (2008)
[4] E.M. Alakshin et al, JETP Letters. **104**(5), 315-318 (2016)
[5] B.P. Cowan, J.Low Temp. Phys. **50**, 132-145 (1983)
[6] S.B. Orlinskii et al, Nanosci. Nanotechnol. Lett. **3**, 1–5 (2011)

List of authors

Table of contents

TABLE OF CONTENTS

ACTUAL PROBLEMS OF MAGNETIC RESONANCE AND ITS APPLICATION

XIX International Youth Scientific School

Program
Lecture Notes
Proceedings

Kazan
24 – 28 October 2016

Signed for printing 18.10.2016.
Offset paper. Digital printing.
Format 60x84 1/8. Гарнитура «Times New Roman».
Conventional printing plates: 7,21
Print run: 80 copies. Order: 162/10

Printing from camera-ready copy
at Kazan University Press printing house

420008, Kazan, Professor Nuzhin str., 1/37
Tel.: (843) 233-73-59, 233-73-28

ISBN 978-5-00019-709-7